Title
The Effects of Non-Uniform Electronic Properties on Thin Film Photovoltaics

Permalink
https://escholarship.org/uc/item/30t6135k

Author
Brown, Gregory Ferguson

Publication Date
2011

Peer reviewed|Thesis/dissertation

The Effects of Non-Uniform Electronic Properties on Thin Film Photovoltaics

by

Gregory Ferguson Brown

A dissertation submitted in partial satisfaction of the

requirements for the degree of

Doctor of Philosophy

in

Engineering - Materials Science and Engineering

in the

Graduate Division

of the

University of California, Berkeley

Committee in charge:

Prof. Junqiao Wu, Chair
Prof. Oscar Dubon
Prof. Peter Hosemann

Spring 2011

Abstract

The Effects of Non-Uniform Electronic Properties on Thin Film Photovoltaics

by

Gregory Ferguson Brown

Doctor of Philosophy in Engineering – Materials Science and Engineering

University of California, Berkeley

Professor Junqiao Wu, Chair

Thin film polycrystalline photovoltaics, typically made with CIGS and CdTe absorber layers, are promising sources of renewable energy due to their high efficiencies (>10%) and low cost. However, a fundamental understanding of their device physics is lacking. One of the primary reasons for this is the difficulty in modeling and quantifying the influence of electronic non-uniformities on device operation. Contrary to conventional silicon cells, which are typically cut from a monocrystalline ingot with relatively homogenous electronic properties, CIGS and CdTe solar cells exhibit both intentional and unintentional spatial variations in electronic properties. Therefore, in order to develop the physics of these photovoltaics, it is necessary to develop new characterization techniques and methods to probe the spatial variation in electronic properties in these material systems.

CIGS solar cells grown at the National Renewable Energy Laboratory were studied using a variety of techniques to quantitatively determine the impact of both intentional and unintentional electronic non-uniformities on device performance. The method of electron beam induced current (EBIC) was extended to characterize the depth dependent electronic properties in compositionally graded absorbers. It was experimentally shown using this EBIC technique that gallium gradients along the depth of the CIGS solar cells improve carrier collection through the introduction of quasi-electric fields. Furthermore, the improvements in the EBIC technique allowed for a quantitative determination of the bulk diffusion length in compositionally graded samples. It was experimentally determined that the bulk diffusion length in CIGS solar cells has no correlation with the device open circuit voltage, in sharp contrast to silicon solar cells. This result could be due to either lateral non-uniformities in the CIGS electronic properties or different defects dominating recombination in the space charge region. Therefore, a theory of electroluminescence intensity was developed for thin film photovoltaics to quantitatively determine the influence of lateral electronic non-uniformities on device performance. Using a combination of electroluminescence and electron beam induced current, it was determined that lateral non-uniformities in the quasi-

neutral bulk electronic properties do not dictate device performance. These results show the defect properties in the space charge region strongly influence device performance thereby providing a theoretical justification for the gallium depth profile observed in the highest efficiency CIGS solar cells. Furthermore, non-uniform secondary blocking barriers were experimentally detected on CIGS solar cells using electroluminescence and attributed to an unpinned Fermi-level at the CIGS/CdS interface combined with a conduction band offset. A discussion on how these results influence other characterization techniques and modeling efforts is provided.

List of Symbols and Abbreviations

ϕ Electric Potential (V)

ς Electric field (V cm^{-1})

ζ Normalized field

ρ Charge density (coulomb cm^{-3})

J_n Electron current density (A cm^{-2})

J_p Hole current density (A cm^{-2})

G_0 Carrier generation rate (cm^{-2}sec^{-1})

G_n Electron generation rate (cm^{-3}sec^{-1})

G_p Hole generation rate (cm^{-3}sec^{-1})

U_n Electron recombination rate (cm^{-3}sec^{-1})

U_p Hole recombination rate (cm^{-3}sec^{-1})

U_{rad} Radiative recombination rate (cm^{-3}sec^{-1})

U_{SRH} Shockley-Read-Hall recombination rate (cm^{-3}sec^{-1})

E_C Conduction band minimum (eV)

E_V Valence band maximum (eV)

E_F Fermi Level (eV)

E_g Bandgap (eV)

σ_{Eg} Standard deviation of bandgaps (eV)

QFL   Quasi-Fermi level splitting (eV)

E_{Fn} Electron quasi-Fermi level (eV)

E_{Fp} Hole quasi-Fermi level (eV)

E_i Intrinsic Fermi level (eV)

E_t Trap level (eV)

$E_{ionization}$ Average energy to create and electron-hole pair (eV)

n Free electron concentration (cm^{-3})

p Free hole concentration (cm^{-3})

n_i Intrinsic carrier concentration (cm^{-3})

$N(E)$ Density of states as a function of energy (cm^{-3}eV^{-1})

$F(E)$ Probability of state being occupied

B Probability for radiative recombination (cm^{3}sec^{-1})

Mc Number of equivalent conduction band minima

N_C Effective density of states in the conduction band (cm^{-3})

N_V Effective density of states in the valence band (cm^{-3})

m_{de} Density-of-state effective mass for electrons (kg)

ε_s Dielectric constant (F cm^{-1})

N_A Acceptor concentration (cm^{-3})

N_D Donor concentration (cm^{-3})

p_0	Free hole concentration on p-side (cm^{-3})
n_0	Free electron concentration on n-side (cm^{-3})
V_{bi}	Built-in voltage (V)
V_{BL}	Voltage drop across secondary diodes (V)
W	Space charge width (cm)
W'	Modified space charge width (cm)
σ_n	Electron capture cross section (cm^2)
σ_p	Hole capture cross section (cm^2)
v_{th}	Thermal velocity of carriers (cm sec^{-1})
N_t	Trap density (cm^{-3})
τ_n	Electron lifetime (sec)
τ_p	Hole lifetime (sec)
μ_n	Electron mobility (cm^2 V^{-1}sec^{-1})
μ_p	Hole mobility (cm^2 V^{-1}sec^{-1})
D_n	Electron diffusivity (cm^2 sec^{-1})
L	Minority carrier diffusion length (cm)
L'	Field modified carrier diffusion length (cm)
L_{eff}	Effective diffusion length (cm)
ξ	Correction factor for diffusion length accounting for back surface
$W + L\xi$	Collection length (µm)
S	Surface recombination velocity (cm sec^{-1})
S'	Field modified surface recombination velocity (cm sec^{-1})
S_g	Grain boundary recombination velocity (cm sec^{-1})
g	Grain size (cm)
h	Planck's constant (eV sec)
$\hbar$	Reduced Planck's constant (eV sec)
q	Electric charge (coulomb)
k	Boltzmann constant (eV K^{-1})
T	Temperature (K)
ϕ_n	Potential barrier at CdS/CIGS interface (eV)
D	Thickness of the AZO, IZO, CdS and CIGS layers (µm)
d	Thickness of absorber layer (µm)
C	Capacitance (F)
A	Sample area (cm^2)
J_0	Diode saturation current (A/cm^2)
j_b	Electron beam current (A/cm^2)
$F(z)$	Carrer collection efficiency as a function of depth
$g(z)$	Carrier generation rate as a function of depth (cm^{-2}sec^{-1})
$C(z)$	Probability of collecting an emitted photon as a function of depth
b	Fraction of backscattered electrons
SRH	Shockley-Read-Hall Recombination
I-V	Current-voltage curve

η	Device Efficiency
J_{sc}	Short circuit current (mA/cm^2)
V_{oc}	Open circuit voltage (V)
FF	Fill factor
CIGS	Cu(In,Ga)Se$_2$
CIS	CuInSe$_2$
CGS	CuGaSe$_2$
TCO	Transparent Conducting Oxide
CBD	Chemical Bath Deposition
IZO	Intrinsic Zinc Oxide
AZO	Aluminum doped Zinc Oxide
DLTS	Deep Level Transient Spectroscopy
AS	Admittance Spectroscopy
N2	Defect observed in CIGS using capacitance techniques
TRPL	Time Resolved Photoluminescence
PL	Photoluminescence
EL	Electroluminescence
CL	Cathodoluminescence
EQE	External Quantum Efficiency
EBIC	Electron Beam Induced Current
eQE	EBIC quantum efficiency
LBIC	Light Beam Induced Current
CV	Capaciance-Voltage measurements
LCR	Inductance (L), Capacitance (C) and Resistance (R) electronic test equipment

Acknowledgments

First, I would like to thank my research advisor Professor Junqiao Wu for his support and guidance. I am very fortunate to have had the opportunity to work for a very talented advisor who was always available and willing to explain any given topic. I look forward to reading about new scientific advances from his group for years to come.

I am extremely grateful to everyone who I have worked with at Nanosolar, Inc without whom this work would not be possible. I especially would like to thank Vladimir Faifer for both his research and personal support. Vladimir not only helped guide this research but also was a constant source of enthusiasm for my work. I'd like to thank Brian Sager, Martin Roscheisen, Ravi Nandan, Geoff Tate and Eugenia Corrales for providing me the opportunity to work at Nanosolar. I am very grateful to both Eugene Bykov and Dave Jackrel for giving me the opportunity to work in their groups and for their constant support. I also would like to thank Ben Cardozo, Alex Pudov, Serge Anikeev and Jeroen van Duren for their scientific insights that both directly contributed to and inspired the work in this thesis. I am also grateful to Ian Kelly Morgan, Will Higgins and Richmond Hollen for their technical support on many experiments.

I would like to thank Dr. Miguel Contreras at the National Renewable Energy Laboratory for providing the samples used in this work. I am also extremely thankful for the opportunity to work with both Dr. Wladek Walukiewicz and Dr. Joel Ager at Lawrence Berkeley National Laboratory. Wladek taught me a great deal about semiconductor physics and Joel was incredibly supportive during my time at Berkeley both technically and personally. I am also grateful for the experimental help provided by Dr. Kin Man Yu and Dr. Lothar Reichertz at the Lawrence Berkeley National Laboratory.

I would like to thank my dissertation committee of Prof. Junqiao Wu, Prof. Oscar Dubon and Prof. Peter Hosemann for their helpful comments in preparing this thesis. I am also very grateful for the opportunity to work closely with Oscar during my final semester at Berkeley as a GSI for his class. In addition to the professors and staff scientists I worked with during my time at Berkeley, I am also grateful to many of my fellow graduate students for their help and support. In particular, I would like to thank Devesh Khanal, Joanne Yim, Marie Mayer, Doug Detert, Nate Miller, Rob Broesler, Tyler Matthews and Alejandro Levander for all of their help during my time at Berkeley.

Finally, this work would not have been possible without the support of my family. I could not have finished this work without the constant love and support from my wife, Kate, who encouraged me while I was going through graduate school. I could not have made it alone. I am also grateful to Buster for providing me an outlet away from school. Finally, I would like to thank my parents, brother and sister for all of the support they have given me through the years. I would especially like to acknowledge my mom who has always showed an interest in my work and encouraged me in all of my pursuits.

Table of Contents

1. Introduction to Thin Film Photovoltaics

1.1 Thin Film Photovoltaics Overview

        The world currently generates most of its electricity from fossil fuels[1.1.1]. For centuries, this was not a problem because fossil fuel consumption was small relative to world fuel reserves and the environment could absorb the resulting CO_2 emissions. This last century of human history provided a number of amazing accomplishments, which have greatly improved the standard of living in large part due to the use of electricity. However, the era of fossil fuels will at some point come to an end due to the finite quantity of recoverable reserves on Earth as well as the finite amount of carbon emissions the Earth can handle while maintaining an environment hospitable to the human economy. Furthermore, the overall population of the Earth continues to rise, as does the energy used per each human being. As a result, it is expected that renewable energy sources will become a larger part of the global economy.

        Fortunately, the sun radiates more than enough energy to the Earth each day to cover all of our electrical needs. The direct conversion of sunlight into electricity can be achieved through photovoltaics (solar cells). Almost all commercially available solar cells are made of inorganic materials, which convert the suns photons into electron-hole pairs, which move to opposite electrical contacts thereby generating a photocurrent. The current-voltage (I-V) curve of a typical solar cell is shown in Fig. 1.1. The most important output parameter for a solar cell is the delivered power, which is the maximum product of current and voltage. The efficiency of a solar cell is defined as the delivered power divided by the incident power. The efficiency (η) of a solar cell is typical measured using the AM 1.5 solar spectrum[1.1.2], which is meant to simulate solar radiation under a certain set of atmospheric conditions thereby offering a means of comparing different solar cells.
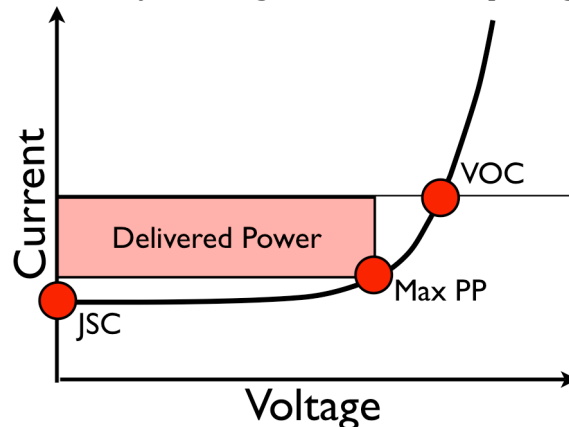

Fig. 1.1: Current-voltage curve for a solar cell. The current at zero voltage is equal to the short circuit current (J_{SC}). The voltage at zero current is equal to the open circuit voltage (V_{oc}). The actual power delivered to the external load is determined by the maximum power point (Max PP).

The efficiency of a solar cell is generally governed by four loss mechanisms[1.1.3] as shown in Fig. 1.2. The first two deal with incoming photons with energies either greater than or less than the optical bandgap of the absorber. Photons with energies below the bandgap are not absorbed and therefore do not contribute to the cell current. Photons with energies above the bandgap will generate hot electrons (holes), which produce waste heat when thermalizing to the bottom (top) of the conduction (valence) band. Furthermore, due to the reciprocity between optical absorption and emission, radiative recombination between electrons and holes limit device efficiencies to between 31% and 41% depending on the concentration of incoming sunlight[1.1.5]. However, in most practical cases, radiative recombination is insignificant compared to Shockley-Read-Hall recombination (SRH recombination), which describes the recombination of electrons and holes through deep defects in the bandgap[1.1.6].
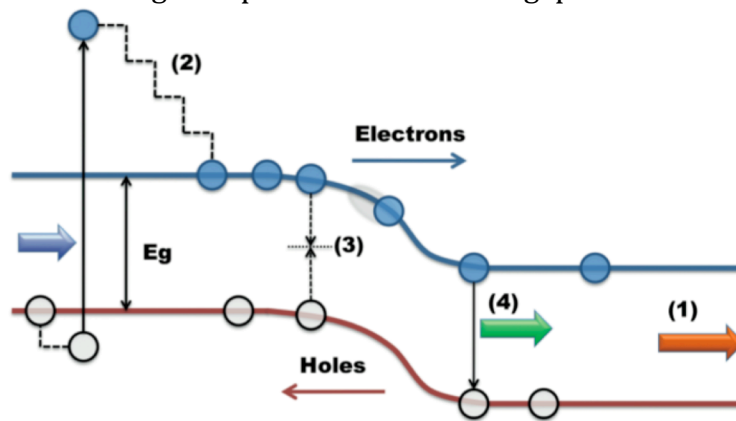

Fig. 1.2: A diagram showing the primary losses in solar cells adopted from Ref. 1.1.4. (1) Incoming photons with energies below the bandgap are not absorbed. (2) Incoming photons with energy in excess of the bandgap are absorbed but the electrons and holes will relax to the conduction band minimum / valence band maximum by producing phonons (represented by dashed lines). (3) Electrons and holes can recombine with the help of electronic states within the bandgap. These states are typically defects or impurity atoms and the recombination event produces phonons. (4) Electrons and holes can also recombine radiatively and produce a photon with an energy equal to the bandgap. Unlike 1, 2 and 3, this radiated energy is not necessarily lost as these photons can be reabsorbed. However, photons emitted from the front of the cell back towards the incoming sunlight are lost forever and ultimately restrict the maximum efficiency of the cells.

The highest efficiency single-junction solar cells are made from silicon, which has received immense amounts of research due to its importance in computing[1.1.7]. However, silicon is an indirect semiconductor and therefore has a very low absorption coefficient requiring thick cells to absorb all the incoming light (>300µm). Direct bandgap semiconductors typically only require a few microns of material to absorb the incoming sunlight and therefore can potentially be made much cheaper. However, the cost savings of depositing thin absorbers can typically only be obtained through the use of a cheap substrate such as glass, aluminum or stainless steel resulting in a polycrystalline absorber. Therefore, an ideal solar cell

material must have both a direct bandgap and have a natural resistance to electronic defects enabling high efficiencies with polycrystalline films.

Fortunately, several semiconductor materials have been identified that fulfill both of these requirements. The two most mature technologies are based on CdTe[1.1.8] and Cu(In,Ga)Se$_2$ (CIGS)[1.1.9], which have achieved efficiencies of over 16% and 20%, respectively. However, these materials have not been under investigation as solar cell materials for as long as silicon, nor have they received anywhere near the same levels of research funding. This is demonstrated in Fig. 1.3 showing the efficiency versus year for both silicon and CIGS. Despite the very high efficiencies of CIGS solar cells, most of the progress made has been empirical in nature. There currently exists no model based on the electronic and physical properties of the cells that allows one to calculate how efficient a CIGS solar cell will be. Therefore, the purpose of this work is to aid the development of such a model by developing new techniques to measure the electronic properties of thin film solar cell absorbers, with a particular emphasis on CIGS given it's the highest efficiency thin film material. One of the primary complications of modeling thin film photovoltaics is the inherent lateral and depth dependence of the electronic properties. Whereas crystalline silicon solar cells are made from large silicon ingots with relatively homogenous properties, CIGS solar cells are deposited with both intentional and unintentional electronic non-uniformities. For this reason, one of the major goals of this work is to provide information on both the in-depth and lateral non-uniformities in the electronic properties of thin film photovoltaics, so that their effects on device performance can be quantified.
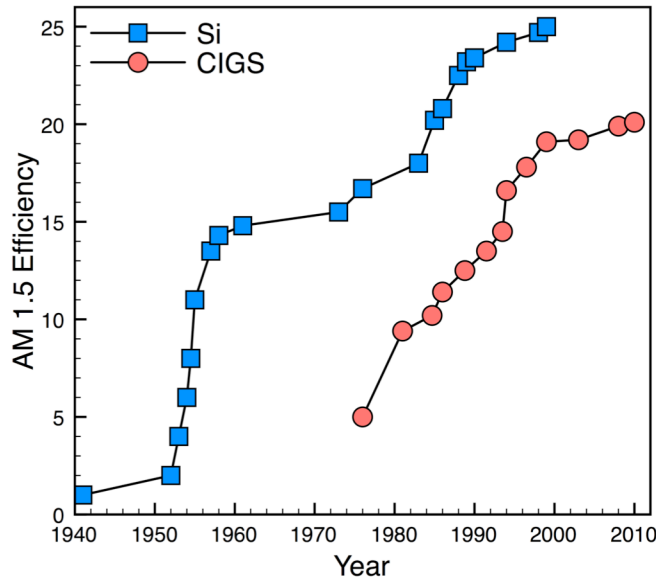

Fig. 1.3: Maximum solar cell efficiency as a function of year for both monocrystalline Si and polycrystalline CIGS solar cells. The data in this figure is taken from Ref. 1.1.10.

1.2 Cu(In,Ga)Se$_2$ (CIGS) Device Structure

The first reported efficiency of a CdS/CuInSe$_2$ heterojunction solar cell was in 1975 from a group at Bell labs[1.2.1]. The power conversion efficiency was cited as 12%, although the device was not tested in a solar simulator but "on a clear day in

New Jersey". This solar cell was made from a single crystal of $CuInSe_2$ with a thick (5-10μm) n-type CdS layer serving as the heterojunction partner. In 1976, a group at the University of Maine developed the first thin film polycrystalline $CdS/CuInSe_2$ solar cells grown on a Au-metallized glass substrate with device efficiencies in the range of 4-5%[1.2.2]. Boeing was the first group to obtain thin film devices with efficiencies exceeding 10% by elemental co-evaporation on Mo-coated glass substrates[1.2.3]. Further improvements in device efficiencies were obtained in 1986 by replacing the thick CdS heterojunction partner with a thin CdS layer followed by a transparent conducting oxide (TCO) layer made of ZnO to serve as the top contact[1.2.4].

From this point on, substantial progress has been made in CIGS solar cell efficiencies with the highest efficiency devices reaching almost 20%[1.2.5]. However, the device structure itself has not changed much since the 1980's. A schematic showing the different layers in a CIGS solar cell is shown in Fig. 1.4. The highest efficiency solar cells are currently grown on soda lime glass substrates that allow processing temperatures above 600°C and provide a good match to the thermal expansion coefficient of CIGS[1.2.6]. It has been shown that the soda lime glass has an additional benefit as it allows Na to diffuse into the CIGS film during growth, improving device performance.

The back contact utilized in almost all CIGS solar cells is Mo. This layer serves as a low resistivity contact responsible for transporting photogenerated holes to the electrical leads outside of the cell. However, experiments have suggested that depositing Mo on CIGS under vacuum results in a rectifying contact, which should preclude the development of high efficiency devices[1.2.7]. Direct electrical measurements of the voltage drop across the CIGS/Mo back contact indicate good ohmic contact[1.2.8]. This apparent contradiction has been resolved by experiments showing a thin layer of $MoSe_2$ forms during CIGS deposition resulting in a high quality ohmic contact[1.2.9]. $MoSe_2$ is typically a p-type semiconductor with a bandgap of roughly 1.3eV and is also expected to help reduce the impact of back surface recombination[1.2.7].
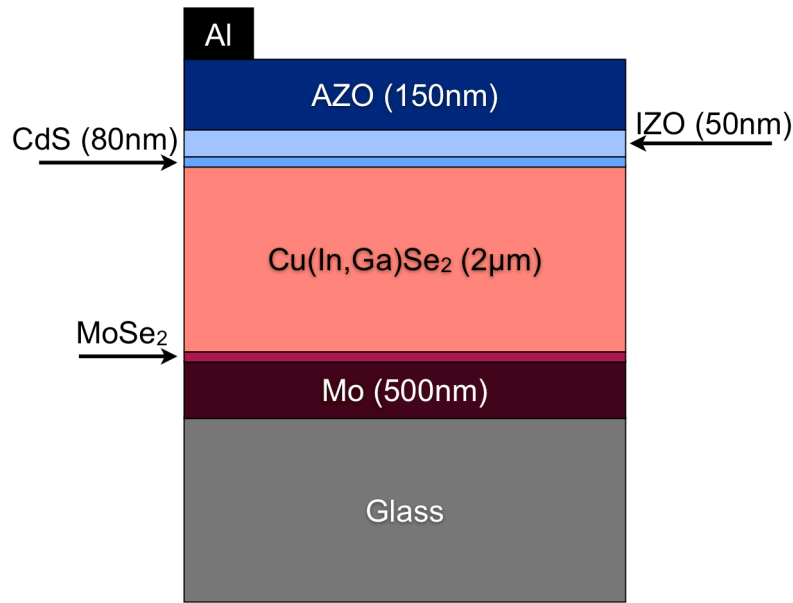
Fig. 1.4: Device structure for a typical CIGS solar cell. All device thicknesses are approximate and are independently optimized for device performance.

The CdS layer serves as the heterojunction parnter for the p-type CIGS. This layer is typically grown using chemical bath deposition (CBD), which results in a thin (~50nm) conformal coating on top of the CIGS[1.2.10]. As previously mentioned, this layer was historically used as the n-type heterojunction partner for CIGS solar cells. However, we note that in current devices, the CdS is too thin and too lightly doped[1.2.7] to complete the junction and thus it's somewhat unclear why this layer is necessary. Several explanations for the beneficial role of CdS in CIGS solar cells have been put forth such as the CdS protects the CIGS surface from damage in the subsequent ZnO processing and the CBD process removes the natural oxide on the CIGS surface[1.2.7]. The CdS layer absorbs photons with energies above 2.4eV and has a lower collection efficiency than the CIGS layer. Therefore, it would be beneficial to replace or remove this layer to improve the short circuit current of the device. However, most attempts at either removing or replacing the CdS layer have resulted in a reduced open circuit voltage relative to the best CdS containing CIGS solar cells and thus a reduced efficiency[1.2.11].
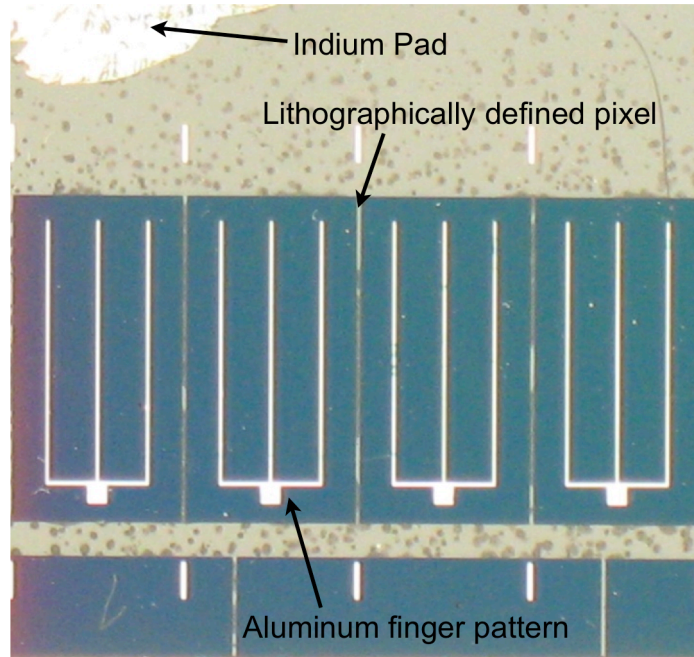
Fig. 1.5: Optical image of electrically isolated pixels on one growth plate. The indium pad connects to the p-type side of the device while the aluminum fingers are used to contact the n-type side.

The final two layers shown in Fig. 1.4 are comprised of ZnO. The first ~50nm of ZnO is intentionally grown with a high resistivity and therefore known as intrinsic ZnO (IZO). This layer is not actually intrinsic but is slightly n-type[1.2.7]. It has been proposed that this layer improves device performance by minimizing the impact of lateral non-uniformities (such as shunts or weak diodes) by providing a finite stack resistance[1.2.12]. The second layer of ZnO is doped with aluminum (AZO) to form a low resistivity TCO layer, which transports photo-generated electrons to the metallic fingers on the surface of the cell. Typically, a large substrate is used during the growth process and individual pixels are lithographically defined after all the individual layers have been deposited. This prevents any one bad region on the substrate from affecting the device performance of every pixel. A typical substrate with individually defined pixels measuring 0.42cm^2 is shown in Fig. 1.5.
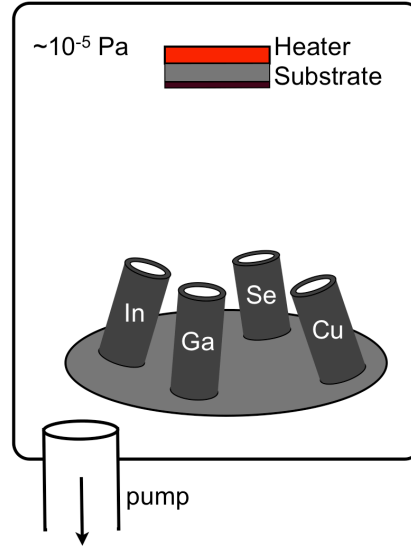
Fig. 1.6: Schematic of a vacuum co-evaporation system used for growing polycrystalline CIGS films.

All of the devices measured in this work were grown by vacuum co-evaporation at the National Renewable Energy Laboratory. A simple schematic of the growth chamber is shown in Fig. 1.6. The substrate is placed at the top of the chamber on a heater, which controls the temperature of the substrate. The chamber is pumped down to roughly 10^{-5} Pa before deposition begins. Each element in the CIGS layer (Cu, In, Ga and Se) is evaporated from a separate Knudsen cell to control the elemental flux on the substrate. The highest efficiency CIGS solar cells are grown in a "three-stage" process, which is shown schematically in Fig. 1.7[1.2.13].
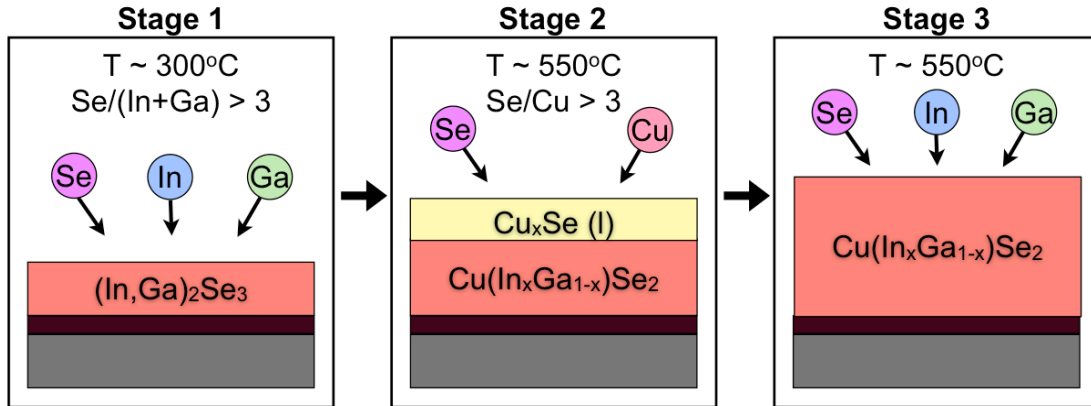

Fig. 1.7: Schematic showing the three-stage process used to grow high efficiency CIGS solar cells by vacuum co-evaporation. In the first stage, a precursor of $(In,Ga)_2Se_3$ is grown in the absence of Cu. During the second stage, Cu is added to the system until the film reaches a Cu-rich composition ($0.95 < Cu/(In+Ga) < 1.1$) at which point a liquid film of Cu_xSe segregates to the surface. The third stage reintroduces In and Ga to bring the final composition of the film to the desired Cu-poor composition. The film is then cooled in a Se environment.

In the first stage of growth, the substrate is heated up to over 300°C after which the In, Ga and Se are released into the chamber. In this stage, a thick layer of

(In,Ga)$_2$Se$_3$ is grown as a precursor. During the second stage, the In and Ga flux is removed and replaced with Cu while the substrate temperature is heated up to over 550°C. The Cu/Group III ratio is slowly raised to above 0.95 at which point it is believed a liquid film of Cu$_x$Se appears on the surface. This liquid is believed to facilitate mass transfer during the growth resulting in larger, more homogenous grains[1.2.13]. However, excess Cu$_x$Se on the film can form highly conductive shunts upon cooling and therefore, a third stage is introduced where the Cu flux is shut off and replaced with In and Ga to consume excess Cu$_x$Se and bring the final composition of the film to Cu poor (Cu/Group III < 0.95). During the entire growth process, the Se flux ratio is always kept above the stoichiometry of the film to improve overall film quality. One of the most important consequences of this film growth is the development of a natural Ga gradient throughout the depth of the sample, which will be discussed further in later sections.

One of the most fascinating characteristics of CIGS solar cells is the wide range of chemical compositions over which one can achieve high performances. It has been shown that the Cu/Group III ratio can vary from 0.7 to 0.98 while still obtaining efficiencies close to 19%[1.2.14]. Furthermore, Ga/Group III ratios can vary from 0.27 to 0.37 without significantly affecting device performance[1.2.14]. This wide degree of flexibility is both remarkably useful, from the standpoint of trying to make high efficiency cells, and frustrating, from the standpoint of trying to correlate any chemical or physical changes in the CIGS cell to device performance. An example of the current lack of understanding can be found in a quote from Ref. 1.2.14, "Our results not only reveal a lack of knowledge with regards to important process parameters, they also point out that supposedly dominant variables as the CIGS composition and crystal structure are sometimes over-estimated in their relevancy for high efficiency CIGS solar cells."

Given the number of layers and polycrystalline nature of CIGS solar cells, the actual band diagram in a device is complicated and varies in all three dimensions. A simplified one dimensional band diagram is frequently used[1.2.7] and one version is shown in Fig. 1.8. The Fermi-level in the AZO is located either very close to or above the conduction band due to the high free carrier concentration in this layer. The space charge region begins in the IZO layer and typically extends a few hundred nanometers into the CIGS layer, which exhibits carrier concentrations on the order of $10^{15} - 10^{16}$ cm^{-3} [1.2.15].
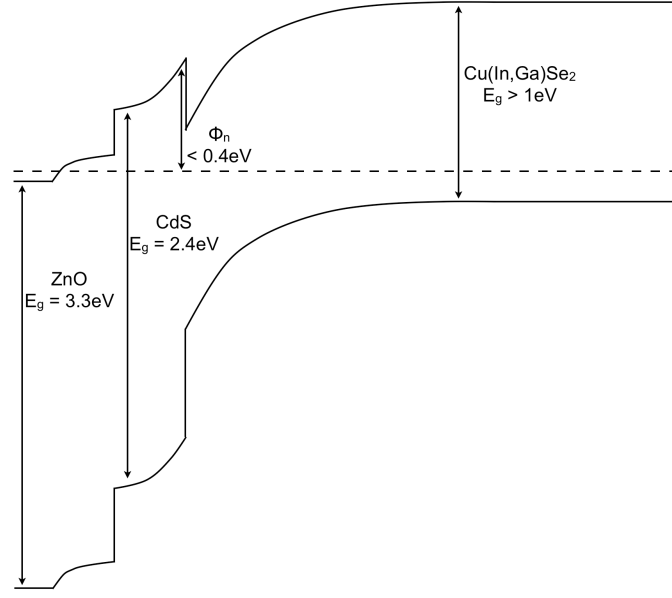
Fig. 1.8: A simplified band diagram of a typical CIGS solar cell.

One of the most complicated aspects of the CIGS band diagram is the CdS/CIGS interface as will be discussed in more depth in Sec. 3.6. A key aspect at this interface is the existence of a conduction band offset between the CdS and CIGS layers[1.2.16, 1.2.17] resulting in a potential barrier for photo-generated electrons equal to Φ_n. It has been shown that potential barriers below ~0.4eV do not significantly impede current collection[1.2.18]. A similar conduction band offset has been observed at the CdS/ZnO interface[1.2.19]. The band diagram in Fig. 1.8 does not include the effects of any interface states between the various layers, which have been shown in several cases to significantly modify device performance[1.2.20].

1.3   Physics of Photovoltaics
There are two requirements for designing a high efficiency solar cell. First, the solar cell must absorb as much of the incoming sunlight as possible and have the photo-generated electrons/holes reach the contacts of the sample. Second, the forward current in the device should be minimized to allow for the highest possible open circuit voltage. As previously discussed, the minimum amount of forward current is achieved when all recombination is radiative in nature. However, very few solar cells actually achieve this and instead are limited by other recombination processes. To quantitatively determine the efficiency of a solar cell, it's necessary to review the equations governing these two requirements to better understand what electronic parameters are needed to describe the operation of a solar cell.
An important starting point is the behavior of a semiconductor in the dark. The following equations are taken directly from Ref. 1.3.1 unless otherwise specified. All of the variables used in the following equations are described on pg. i-iii of this work. The equilibrium free electron concentration (n) of a semiconductor in the dark is given by

$$n = \int_{E_C}^{\infty} N(E)F(E)dE ,$$ (1.1)

where $N(E)$ is the density of states, $F(E)$ is the probability of the state being occupied and E_C is the energy of the conduction band minimum. The density of states in the conduction band can be approximated by

$$N(E) = M_C \frac{\sqrt{2}}{\pi^2} \frac{m_{de}^{3/2}(E - E_C)^{1/2}}{\hbar^3} ,$$ (1.2)

where M_C is the number of equivalent conduction band minima and m_{de} is the density-of-state effective mass for electrons. The occupancy of each level is given by the Fermi-Dirac distribution function

$$F(E) = \frac{1}{1 + \exp[(E - E_F)/kT]} ,$$ (1.3)

where E_F is the Fermi level. If the Fermi level is several kT below the conduction band, Boltzmann statistics can be used and the integral in Eqn. 1.1 becomes

$$n = N_C \exp\left(\frac{E_F - E_C}{kT}\right)$$ (1.4)

where the effective density of states in the conduction band (N_C) is approximately

$$N_C \equiv 2\left(\frac{2\pi m_{de}kT}{h^2}\right)^{3/2} M_C .$$ (1.5)

By similar arguments, the equilibrium hole concentration (p) is given by

$$p = N_V \exp\left(\frac{E_V - E_F}{kT}\right),$$ (1.6)

where E_V is the valence band maximum and N_V is the effective density of states for the valence band. In the absence of any dopants, the only carriers in the conduction and valence band are provided by thermal agitation. Therefore, due to charge conservation, the number of free electrons and holes are equivalent. By equation Eqn. 1.4 and 1.6, the intrinsic carrier concentration (n_i) of a non-degenerate semiconductor is equal to

$$n_i = \sqrt{N_C N_V} \exp\left(\frac{-E_g}{2kT}\right),$$ (1.7)

where E_g is the bandgap of the semiconductor. Therefore, in the dark, the free carrier statistics in a semiconductor are given by the locations of the conduction band, valence band and Fermi-level as shown in Fig. 1.9.
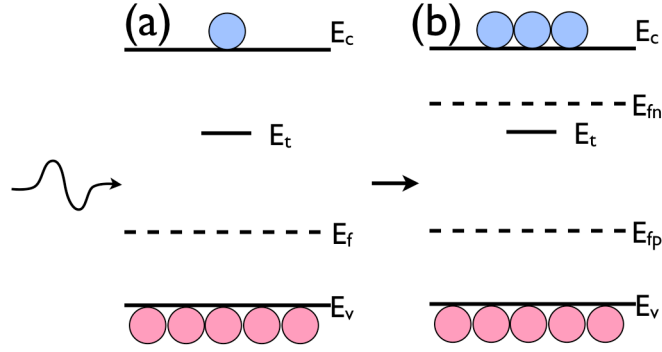
Fig. 1.9: (a) A generic p-type semiconductor in the dark can be described by the conduction band (E_C), valence band (E_V), Fermi-level (E_f). (b) Upon illumination, the semiconductor is no longer in equilibrium as is instead described by separate Fermi-levels for the conduction and valence band (E_{fn} and E_{fp}). The number of excess holes under solar illumination is typically much lower than the hole concentration in the dark. The number of excess electrons greatly exceeds the electron concentration in the dark and is governed primarily by the amount of illumination and the properties of the trap levels (E_t).

However, upon illumination or charge injection, a semiconductor is no longer in equilibrium and these three parameters are no longer sufficient to describe the free carrier statistics. In this case, it is necessary to define separate quasi-Fermi levels for both the conduction $\left(E_{Fn}\right)$ and valence $\left(E_{Fp}\right)$ band as

$$E_{Fn} \equiv E_i + kT \ln(\frac{n}{n_i}), \tag{1.8}$$

$$E_{Fp} \equiv E_i - kT \ln(\frac{p}{n_i}), \tag{1.9}$$

where E_i is the intrinsic Fermi level. The location of quasi-Fermi levels under illumination or applied bias is primarily determined by the properties of defects states located within the bandgap.

Most thin film photovoltaics consist of several separate semiconductors with different properties in contact with one another. A full description of the entire device under illumination can be given by the carrier concentration at every point within the device. For this reason, it is necessary to know the location of the band edges and quasi-Fermi levels throughout the device. This can be accomplished by self consistently solving the following sets of equations, shown here in their one-dimensional form:

$$\frac{\partial^2 \phi}{\partial x^2} = -\frac{\partial \varsigma}{\partial x} = \frac{-\rho}{\varepsilon_s} = \frac{q(n - p + N_A - N_D)}{\varepsilon_s}, \tag{1.10}$$

$$J_n = q\mu_n\left(n\varsigma + \frac{kT}{q}\frac{\partial n}{\partial x}\right) = \mu_n n \frac{\partial E_{Fn}}{\partial x}, \tag{1.11}$$

$$J_p = q\mu_p\left(p\varsigma - \frac{kT}{q}\frac{\partial p}{\partial x}\right) = \mu_p p \frac{\partial E_{Fp}}{\partial x}, \tag{1.12}$$

$$\frac{\partial n}{\partial t} = G_n - U_n + \frac{1}{q}\frac{\partial J_n}{\partial x}, \tag{1.13}$$

$$\frac{\partial p}{\partial t} = G_p - U_p - \frac{1}{q}\frac{\partial J_p}{\partial x} \tag{1.14}$$

where ϕ is the electric potential, ς is the electric field, ρ is the charge density, ε_s is the dielectric constant, N_A is the acceptor concentration, N_D is the donor concentration, J_n is the electron current density, J_p is the hole current density, μ_n is the electron mobility, μ_p is the hole mobility, G_n is the electron generation rate, G_p is the hole generation rate, U_n is the electron recombination rate and U_p is the hole recombination rate.

Eqn. 1.10 is Poisson's equation and describes the change in potential or electric field across a device. Eqn. 1.11 and 1.12 define the electron and hole current densities throughout the device. The first term $(n\varsigma)$ represents the drift component of current and the second term $\left(\dfrac{kT}{q}\dfrac{\partial n}{\partial x}\right)$ the diffusion component. Finally, Eqn. 1.13 and 1.14 are the continuity equations stating the net change in carrier concentration at a given point in the cell is given by the generation of carriers, recombination of carriers and net change in current flowing in and out of the region of interest. Under quasi-equilibrium conditions, such as constant illumination, the net change of carriers is equal to zero and therefore a self-consistent solution of 1.10 through 1.14 can be obtained.

In real systems, it can be very difficult or impossible to obtain a set of analytic solutions describing the system and the method of finite element analysis must be used to solve these equations. This approach involves splitting the device structure into discrete layers where all properties within that layer are held constant. The solution to the problem is guessed and then equations 1.10 through 1.14 are calculated between each layer. The algorithm then modifies the initial guess and solves the set of equations again, proceeding until the error between each layer falls below some threshold. Several commercial and freeware software packages have been designed to solve these equations with varying degrees of complexity. In this work, the software package AMPS[1.3.2] is used when necessary. However, it is frequently helpful to use analytic approximations to describe solar cell behavior and they will be used in this work wherever possible.

Equations 1.13 and 1.14 contain terms for the recombination rate at a given location in the cell. There are several types of recombination events that can occur and they are summarized in Fig. 1.10. The radiative recombination rate (U_{rad}) is given by[1.3.3]

$$U_{rad} = Bnp, \tag{1.15}$$

where B is the probability for radiative recombination. It is frequently helpful to define a minority carrier lifetime (τ_n / τ_p) in a semiconductor, which gives the average amount of time a free electron/hole will remain in the semiconductor until it recombines with an electron/hole. In the case of radiative recombination, the lifetime of a minority carrier is a function of the number of majority carriers

$$\tau_{p,rad} = \frac{1}{Bn}, \qquad (1.16)$$

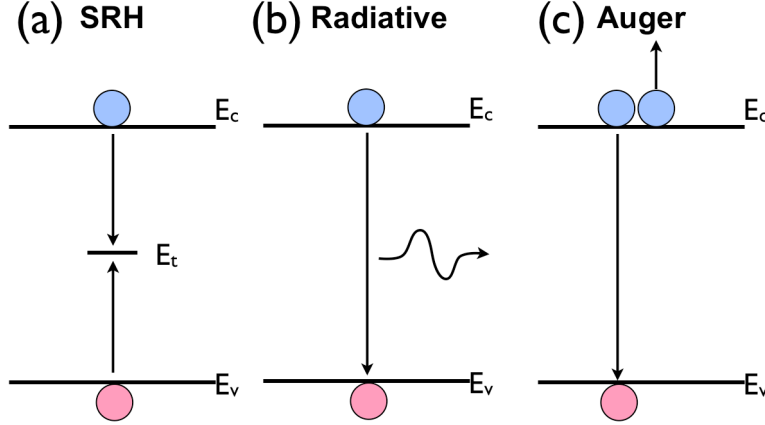$$\tau_{n,rad} = \frac{1}{Bp}. \qquad (1.17)$$

Fig. 1.10: The primary recombination mechanisms in a semiconductor. (a) Shockley-Read-Hall recombination describes the recombination of electrons and holes through trap levels located in the bandgap where the excess energy is typically released through phonons. (b) Radiative recombination accounts for the direct recombination of electrons and holes through the emission of photons. (c) Auger recombination allows for recombination between two electrons and one hole where the excess energy from electron-hole recombination is transferred to the third electron.

However, semiconductors usually have a non-negligible density of states within the bandgap through which recombination is more probable. The equation governing trap-assisted recombination was originally described by Shockley, Read and Hall who found the recombination rate equal to[1,3,4]

$$U_{SRH} = \frac{\sigma_p \sigma_n v_{th} N_t (pn - n_i^2)}{\sigma_n \left[n + n_i \exp\left(\frac{E_t - E_i}{kT} \right) \right] + \sigma_p \left[p + n_i \exp\left(\frac{E_i - E_t}{kT} \right) \right]}, \qquad (1.18)$$

where σ_n is the electron capture cross section, σ_p is the hole capture cross section, v_{th} is the carrier thermal velocity, N_t is the trap density and E_t is the trap energy. The carrier lifetime for SRH recombination is a strong function of the Fermi-level position in the semiconductor. However, in the situation where the semiconductor is primarily n- or p-type (ie. the quasi-neutral region of the absorber), the carrier lifetime can be simplified as

$$\tau_p = \frac{1}{\sigma_p v_{th} N_t}, \qquad (1.19)$$

$$\tau_n = \frac{1}{\sigma_n v_{th} N_t}. \qquad (1.20)$$

To determine the amount of forward current as a function of applied bias in a solar cell, it is useful to isolate the region of the cell where recombination is taking place. The four primary areas in a CIGS solar cell where recombination is expected

to take place are shown in Fig. 1.11. The first area to be considered is within the space charge region (SCR). The quasi-Fermi level splitting (QFL) inside the SCR is approximately equal to[1.3.1]

$$qV = E_{Fn} - E_{Fp}.$$ (1.21)

From combining Eqn. 1.8 and 1.9, one arrives at

$$pn = n_i^2 \exp\left(\frac{E_{Fn} - E_{Fp}}{kT}\right),$$ (1.22)

which can be inserted into Eqn. 1.16 to give

$$U_{SCR}(V) = \frac{\sigma_p \sigma_n v_{th} N_t n_i^2 [\exp(qV/kT) - 1]}{\sigma_n [n + n_i \exp\left(\frac{E_t - E_i}{kT}\right) + \sigma_p [p + n_i \exp\left(\frac{E_i - E_t}{kT}\right)}.$$ (1.23)

In the case that the trap primarily responsible for recombination is located in the mid-gap and has an equal capture cross section for electrons and holes, the maximum recombination rate is equal to

$$U_{SCR,\max} \approx \frac{1}{2}\sigma v_{th} N_t n_i \exp\left(\frac{qV}{2kT}\right).$$ (1.24)

By integrating Eqn. 1.23 through the space charge region, the forward current density as a function of voltage can be expressed as[1.3.5]:

$$J(V) \approx \frac{qW'n_i}{2\tau}\exp(qV/2kT),$$ (1.25)

where the modified space charge width $\left(W'\right)$ is given by

$$W' = WkT/q(V_{bi} - V),$$ (1.26)

where W is the space charge width and the built-in voltage V_{bi} is given by

$$V_{bi} \approx \frac{kT}{q}\ln\left(\frac{n_0 p_0}{n_i^2}\right),$$ (1.27)

where n_0 is the free electron concentration on the n-side of the junction and p_0 is the free hole concentration on the p-side of the junction.
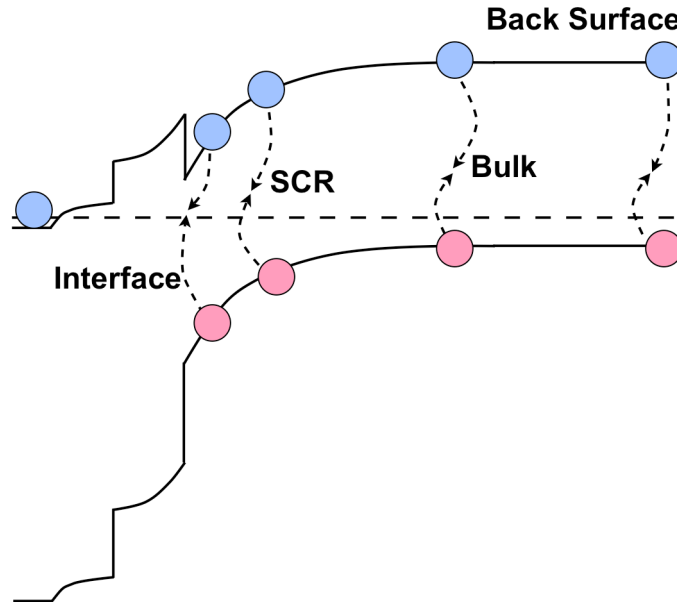
Fig. 1.11: The physical location of the primary recombination paths in a CIGS solar cell. Recombination can take place through interface states, within the space charge region (SCR), within the quasi-neutral bulk or at the back surface.

To illustrate the physical model of recombination given by Eqn. 1.23, the normalized recombination rate as a function of distance of a n$^+$p heterojunction was numerically calculated and the result is shown in Fig. 1.12. The band diagram under forward bias was obtained using the depletion approximation and the analytic equations derived in Ref. 1.3.1. Fig. 1.12 shows three different cases where the recombination is controlled by a generic mid-gap state, a trap state closer to the valence band and a trap state with a higher capture cross section for holes than electrons. It is apparent that changing the type of trap leads to a shift in the recombination profile. However, in general, SCR recombination is highest close to the middle of the depletion region. This can be understood by considering recombination requires the presence of both an electron and a hole. In the middle of the SCR there is a high concentration of both electrons and holes. The concentration of holes falls off sharply when approaching the n-side of the junction while the concentration of electrons falls off sharply when approaching the p-side of the junction leading to a maximum recombination rate in the middle of the SCR.
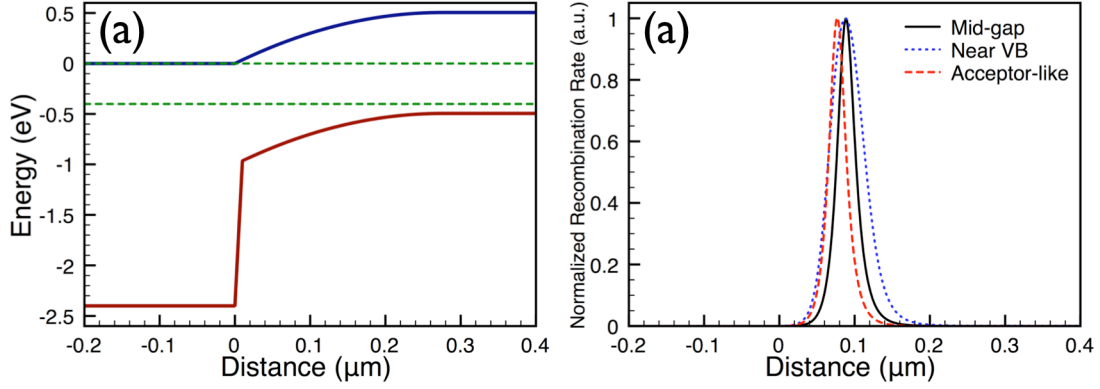
Fig. 1.12: (a) Simplified band diagram of a n+p heterojunction solar cell under a forward bias of 0.4V. (b) Calculated recombination profile as a function of distance through the cell assuming different defect properties. The first case (mid-gap) assumes the dominant trap level is located in the middle of the bandgap with $N_t = 2 \cdot 10^{13} cm^{-3}$ and $\sigma_n = \sigma_p = 5 \cdot 10^{-13} cm^2$. The second case (near VB) assumes the dominant trap level is instead 300meV above the valence band. The third case (acceptor-like) assumes a mid-gap trap but with $\sigma_n = 5 \cdot 10^{-13} cm^2$ and $\sigma_p = 5 \cdot 10^{-12} cm^2$.

The next area of recombination considered is in the quasi-neutral bulk of the CIGS and the back interface. In this region, Eqn. 1.18 is approximately equal to

$$U(x,V) = n(x,V)/\tau_n. \tag{1.28}$$

Therefore, to analytically express the recombination in the quasi-neutral bulk it is necessary to know the excess electron concentration in the bulk. The high free hole concentration in the bulk leads to a negligible gradient in the hole quasi-Fermi level. Therefore, Eqn. 1.11 and 1.13 can be combined to give

$$\frac{1}{qD_n}\frac{\partial J_n}{\partial x} = \frac{\zeta\partial n}{\partial x} + \frac{\partial^2 n}{\partial x^2} = \frac{n}{L^2} \tag{1.29}$$

where the normalized electric field (ζ) and diffusion length (L) are given by

$$\zeta = \frac{q\varsigma}{kT}, \tag{1.30}$$

$$L = \sqrt{D_n \tau_n}, \tag{1.31}$$

and the electron diffusivity D_n is given by

$$D_n = \frac{kT}{q}\mu_n. \tag{1.32}$$

A general solution of Eqn. 1.29 can be obtained by assuming there is no electric field in the quasi-neutral bulk[1.3.6],

$$n = A\exp(-x/L) + B\exp(x/L). \tag{1.33}$$

The constants in Eqn. 1.33 can be obtained by assuming the electron quasi-Fermi level varies at edge of the SCR by the applied voltage

$$n(W) = n_0(W)\exp(qV/kT) \tag{1.34}$$

and the current at the back of the cell is equal to

$$J_n(d-W) = qn(d-W)S, \tag{1.35}$$

16

where (d) is the absorber thickness and S is the back surface recombination velocity. Combining Eqn. 1.28, 1.33, 1.34 and 1.35 results in[1.3.6]

$$J(V) \approx q \sqrt{\frac{D_n}{\tau_n}} \frac{n_i^2}{p_0} \exp(qV/kT) \frac{\sinh((d-W)/L) + (SL/D_n)\cosh((d-W)/L)}{\cosh((d-W)/L) + (SL/D_n)\sinh((d-W)/L)}. \qquad (1.36)$$

However, high efficiency CIGS solar cells feature a varying bandgap along the depth of the absorber. From Ref. 1.3.6, the change in bandgap results in a quasi-electric field throughout the bulk leading to[1.3.6]

$$\zeta = \frac{1}{kT} \frac{\partial E_g}{\partial x}. \qquad (1.37)$$

The solution to Eqn. 1.29 changes as a result of the quasi-electric field in the bulk to

$$n = A\exp(-x/L_+) + B\exp(x/L_-), \qquad (1.38)$$

where

$$L_\pm = L \Big/ \left[\sqrt{1 + (\zeta L/2)^2} \pm \zeta L/2 \right]. \qquad (1.39)$$

Using the same boundary conditions shown in Eqn. 1.34 and 1.35, one obtains

$$J(V) \approx \left(\frac{qD_n}{L'} \frac{n_i(W)^2}{p_0} \frac{\sinh((d-W)/L') + (S'L'/D_n)\cosh((d-W)/L')}{\cosh((d-W)/L') + (S'L'/D_n)\sinh((d-W)/L')} - qD_n \frac{n_i(W)^2}{p_0} \frac{\zeta}{2} \right) \exp(qV/kT), \qquad (1.40)$$

where the modified diffusion length (L') and (S') surface recombination velocity are given by

$$L' = L \Big/ \sqrt{1 + (\zeta L/2)^2}, \qquad (1.41)$$

$$S' = S + \zeta D_n/2. \qquad (1.42)$$

However, the quasi-electric field in the CIGS absorber is not constant all the way through the depth of the sample. This is shown in Fig. 1.13 for a high efficiency CIGS solar cell with a "saddle" shaped profile. This can be accounted for by dividing the absorber into regions of approximately constant quasi-electric field. In this case, the back surface recombination velocity in the first layer is modified by using[1.3.6]

$$S = J_0 \Big/ \left(q \frac{n_i^2(I)}{p_0} \right) \qquad (1.43)$$

where I is the location of the next adjoining region and J_0 is the diode saturation current. In this way, the recombination current in each layer is defined recursively, where the first layer has a back surface recombination velocity set by the subsequent layers. In a similar way, the splitting of the quasi-Fermi level at the front of the last region is fixed by the properties of the proceedings layers.
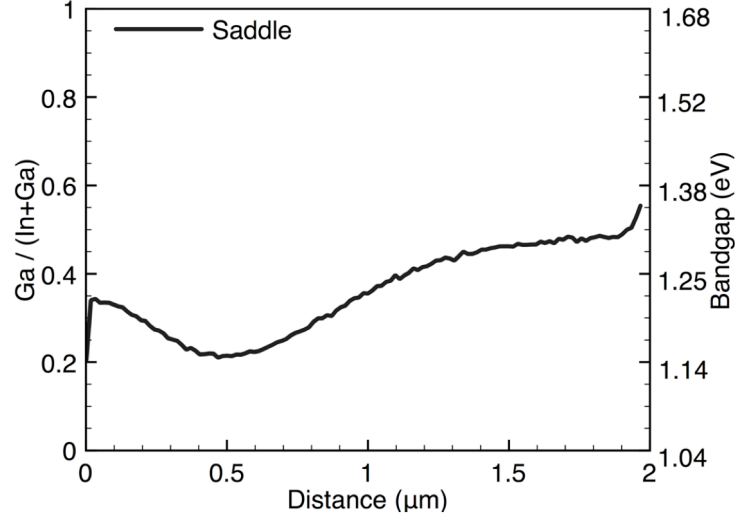
Fig. 1.13: Ga/(In+Ga) ratio as a function of depth through a high efficiency CIGS solar cell grown at NREL with a "saddle" shaped profile. The gallium gradient results in a change in bandgap through the depth of the film shown on the second y-axis. Due to the p-type nature of the absorber layer, the bandgap profile is approximately equal to the conduction band profile in the quasi-neutral bulk.

As the absorber is polycrystalline in nature, the recombination properties at the grain boundaries are important. It has been shown that this can be incorporated into the preceding equations for quasi-neutral bulk recombination by replacing the diffusion length with [1.3.7]

$$L_{eff} = \left(L^{-2} + 2S_g / D_n g \right)^{-1/2} \tag{1.44}$$

where S_g is the grain boundary recombination velocity and g is the grain size.

Finally, recombination at the CdS/CIGS interface is also expected to be important, primarily due to the high concentration of defects expected at almost any hetero-interface. The recombination rate at this interface is a strong function of the Fermi-level position with respect to the band edges. If the Fermi-level is close to the conduction band (as expected in high efficiency CIGS solar cells), recombination is primarily determined by the minority hole concentration. However, in general, the recombination rate at a heterointerface is complicated and depends strongly on the conduction band offsets at this interface as well as the absence or presence of Fermi-level pinning. A complete discussion of the recombination rates at a heterojunction interface can be found in Ref. 1.3.8.

One of the most common methods to try and separate the recombination processes in solar cells is to analyze the diode ideality factor of the device. The ideality factor is equal to the denominator of the exponential term in the current voltage equation (Eqn. 1.25, 1.36 or 1.40). Therefore a logarithmic plot of the current versus the voltage can be used to experimentally determine diode ideality factor and help determine which region of the device controls forward current. In practice, this is frequently difficult and the simplified equivalent circuit used in analyzing solar cells leads to some error. For this reason, more complex techniques have been proposed to extract the diode ideality factor[1.3.9].

Using the ideal diode theory, the diode ideality factor should vary between 1 and 2 depending on the dominant recombination process, although the dominant recombination process itself can change as a function of voltage. For quasi-neutral bulk recombination, the free electron concentration at the edge of the space charge region is the only voltage dependent term determining the recombination rate (Eqn. 1.34). As the quasi-Fermi level splitting at the edge of the space charge region is equal to the applied voltage, the increase in free electron concentration is exponentially proportional to (qV/kT) leading to an ideality factor of 1.

Alternatively, in the case of space charge region recombination, the recombination rate is governed by the excess concentration of both electrons and holes in the middle of the space charge region. Again, the quasi-Fermi level splitting is equal to the applied voltage and since both the electron and hole quasi-Fermi levels are moving, each level only changes by $V/2$. For this reason, the exponential term in Eqn. 1.25 reads $\exp(qV/2kT)$ and the diode ideality factor is equal to 2. Again, both of these recombination theories are only approximations of the device behavior and any changes in their underlying assumptions can lead to a variation in the diode ideality factor. Furthermore, several authors have noted that the highly defective nature of the CIGS and CdS layers can lead to an increased contribution of tunneling recombination, which is not explicitly discussed in this work[1.3.10]. In this case, the diode ideality factor can even exceed 2. Previous attempts to use the diode ideality factor to determine the location of recombination in CIGS solar cells will be discussed in more detail in Sec. 1.4.

Ultimately, by reviewing the previous equations, it is apparent that the most important electronic properties governing forward current are the bandgap, defect density, capture cross section and free carrier density of the absorber. However, the equations describing recombination vary depending on whether the recombination occurs in the neutral bulk, space charge region or the front or back interface. Furthermore, the influence of each electronic defect on device performance will vary depending on its spatial location in the CIGS absorber. It is highly likely that all of the electronic parameters vary both in depth and laterally across the sample making it imperative to develop spatially sensitive techniques to determine the parameters responsible for controlling device operation.

The second requirement of solar cells, to collect all the photo-generated carriers, is closely related to the first requirement of minimizing the forward current. It has been shown that the carrier collection probability (f_c) in the quasi-neutral bulk is related to the carrier concentration in the dark through a reciprocity theorem: [1.3.11]

$$f_c(x) = \frac{n(x)}{n_0(x)} \tag{1.45}$$

In the case of bandgap grading, the equilibrium dark carrier concentration can be expressed as[1.3.6]

$$n_0(x) = n_0(W)\exp(-\zeta x). \tag{1.46}$$

As a result, the collection efficiency in the quasi-neutral bulk can be expressed as [1.3.6]

$$f_c(x) = \exp(\zeta x/2)\left(\frac{\cosh((d-W-x)/L') + (S'L'/D_n)\sinh((d-W-x)/L')}{\cosh((d-W)/L') + (S'L'/D_n)\sinh((d-W)/L')}\right).\qquad(1.47)$$

Eqn. 1.47 expresses the carrier collection probability in the quasi-neutral bulk of the CIGS absorber. Within the SCR, the collection probability is effectively unity due to the large built-in electric field resulting in a high concentration of both carrier types. As a result, the photogenerated carriers can quickly move across the SCR resulting in a negligible recombination loss. However, some photo-generated carriers are also absorbed in the CdS and ZnO layers of the cell. It is difficult to derive the collection probability in these layers without knowing the exact band diagram and properties of these layers. Experimentally, it has been shown that roughly 50% of the carriers generated in the CdS are lost to recombination while almost no carriers generated in the ZnO are collected[1.3.7].

Ultimately, Eqn. 1.47 shows that the primary factors controlling short circuit current in a cell are the space charge width, quasi-electric field, back surface recombination properties and the diffusion length in the quasi-neutral bulk. Furthermore, many of these parameters also show up in the equations for forward current indicating that in many cases, the two should be related.

1.4   Electronic properties of CIGS

The equations governing recombination in a solar cell can be generally applied to any material system. As mentioned previously, the two primary requirements for a high efficiency solar cell are to collect as many of the photogenerated carriers as possible and to minimize the amount of forward current to achieve a high open circuit voltage. Collecting photogenerated carriers requires maximizing the collection efficiency throughout the quasi-neutral bulk. According to Eqn. 1.47, this requires maximizing the bulk diffusion length, which according to Eqn. 1.31 requires maximizing the minority electron lifetime. The most important variables governing the minority electron lifetime in the quasi-neutral bulk are the density of electron traps and their respective capture cross sections. Additionally, as the device thickness can be smaller than the bulk diffusion length, it is also critical to obtain a low back surface recombination velocity.

The situation is similar for the forward current contribution from the neutral bulk. In this case, eqn. 1.36 shows it is also important to maximize the bulk diffusion length and therefore reduce the density of electron traps in the material. However, two other variables also play a key role in eqn. 1.36. First, the recombination current is proportional to the square of the intrinsic carrier concentration and thus exponential proportional to the bandgap of the absorber (Eqn. 1.7). Second, the recombination current is inversely proportional to the hole concentration in the quasi-neutral bulk.

The situation is somewhat more complex for recombination in the space charge region. Eqn. 1.23 shows that the recombination is again proportional to the intrinsic carrier concentration while eqns. 1.25-1.27 show recombination is also proportional to the hole concentration in the absorber. However, Eqn. 1.23 shows recombination is now tied to both the electron and hole trap properties. In the general case of assuming a midgap defect with equal probability for electron and

hole capture, one can arrive at Eqns. 1.24,1.25. However, there is no a priori reason to assume such generic defects exist in the material. To gain a full understanding of how CIGS solar cells behave, it is necessary to have information on how the chemistry and structure of the material affect the bandgap, hole concentration and defect levels within the material. The purpose of this section is to provide a brief literature review on these three topics followed by previous attempts to describe recombination in CIGS solar cells.
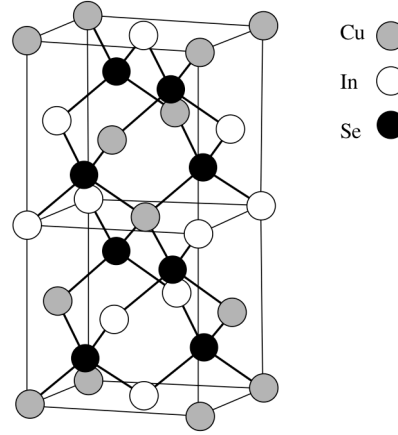
Fig. 1.14: Chalcopyrite crystal structure of CuInSe$_2$. Image taken directly from Ref. 1.4.1.

CIGS has the chalcopyrite crystal structure (Fig. 1.14)[1.4.1] and first principles calculations have shown the bandgap can be described by the empirical relationship[1.4.2]

$$E_g(CuIn_{1-x}Ga_xSe_2) = 1.04(1-x) + 1.68x - 0.21x(1-x), \tag{1.48}$$

where the incorporation of gallium primarily modifies the conduction band. However, deviations from stoichiometry in CIGS thin films lead to significant Urbach tails below the conduction band minimum[1.4.3]. While there has been no correlation between the Urbach tail energy and recombination current in solar cells, a correlation has been observed with the short circuit current of devices suggesting the degree of sub-bandgap tails may influence the electron mobility and hence carrier collection[1.4.4].

The free carrier concentration in CIGS is primarily controlled by native defects, which in turn can be controlled by changing the stoichiometry. It has been observed that the carrier concentration and carrier type of a film can be altered through the Se/(Cu+In) ratio and Cu/In ratio[1.4.5]. In general, it has been observed that Cu-rich films are always p-type while In-rich films can be made either n- or p-type. When the Se/(Cu+In) ratio is greater than 1, In-rich films are typically p-type while in the opposite case, the films are n-type[1.4.1]. Solar cell quality CIGS films are almost always Se-rich and Cu-poor. These qualitative trends combined with first principles calculations suggest that V_{Cu} and Cu_{In} point defects are acceptor like while In_{Cu} are donors[1.4.6]. Fig. 1.15 provides a rough estimation of the type and energy level of some point defects in CIS[1.4.6]. In addition to those shown, it has been determined that V_{Se} acts as a compensating donor in p-type material[1.4.1,1.4.7,1.4.8]. It has also been observed that the incorporation of sodium can increase the hole

concentration in CIGS films, although it is generally thought that the sodium itself is not an acceptor but is simply changing the relative populations of the intrinsic defects [1.4.1].

One of the more interesting properties of CIGS is that efficient solar cells can be made with extremely off-stoichiometric material. Efficiencies close to 19.5% have been achieved with Cu/(In+Ga) ratios from 0.7 to 0.98[1.4.9]. Even in this large composition range, carrier concentrations on the order of $10^{16} cm^{-3}$ are typically observed[1.4.1]. This has been explained by the low formation energy of the defect pair $2V_{Cu}^{-} + In_{Cu}^{2+}$. First principles calculations show this pairing effectively pushes the In_{Cu} defect levels closer to the conduction band thereby minimizing their influence on recombination[1.4.2].
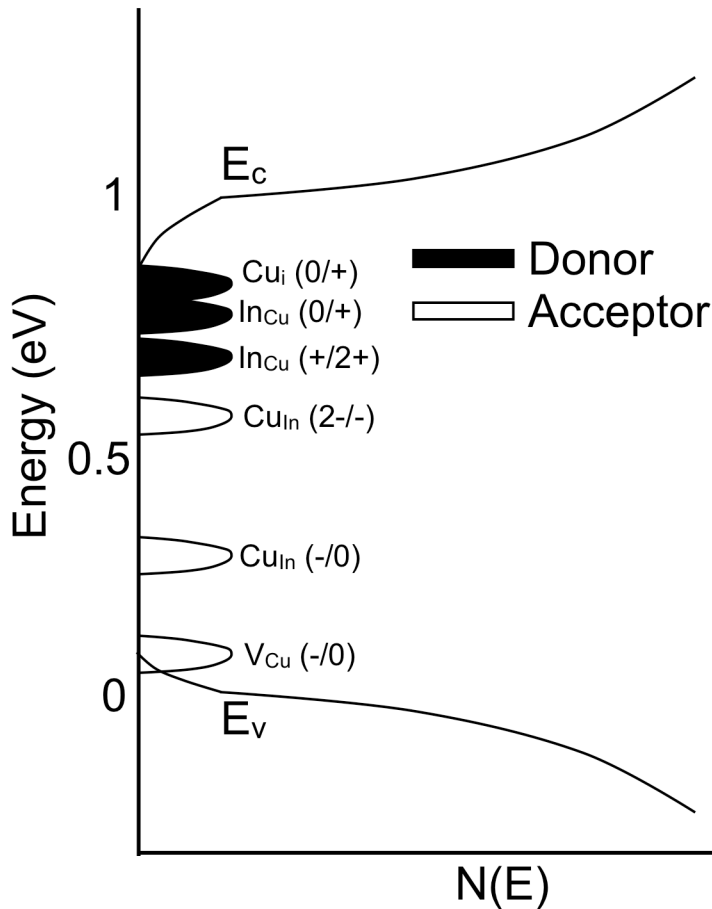

Fig. 1.15. Location of several point defects within the bandgap of $CuInSe_2$. The relative position and identification of these defects are taken from Ref. 1.4.6.

While the bandgap and hole concentration in CIGS films are fairly well established experimentally, the same cannot be said for deep defects. Numerous publications have reported various defect levels in CIGS films, typically through capacitance or luminescence techniques, but very few of these levels have been unambiguously assigned to a chemical origin or been found to directly dictate device performance.

Defect studies have been carried out on both single crystalline and polycrystalline samples. Several hole traps have been observed by deep level transient spectroscopy (DLTS) in single crystal homo and heterojunctions of CIS with the most commonly reported defect being ~250meV above the valence band edge[1.4.10]. Admittance spectroscopy (AS) and DLTS measurements on polycrystalline CIS and CIGS solar cells have also observed hole traps around 250 to 320meV from the valence band edge [1.4.11,1.4.12]. Several publications refer to this defect as N2. Given this trap is observed in both polycrystalline and monocrystalline samples, it is believed to originate from the CIGS bulk. Generally, the defect concentration is found to be around 10^{15} to $10^{16}cm^{-3}$. The defect is not a single level but a Gaussian distribution of levels with some tail extending into the midgap[1.4.13]. This defect band has been found to remain fixed relative to the valence band when increasing the gallium concentration and move farther away from the valence band when adding sulfur to the system[1.4.14]. Therefore, it has been proposed that the defect energy remains constant relative to the vacuum level.

Some groups have been able to correlate the concentration of this defect with device performance. In one case, devices with varying gallium-contents were fabricated while the concentration of the N2 defect was measured using AS. The concentration was found to correlate well with $E_g - V_{oc}$ indicating the defect may be responsible for controlling forward current in CIGS devices[1.4.15]. Another group used electron irradiation to damage CIGS solar cells and found the reduction in open circuit voltage correlated with the increase of the N2 defect in the device[1.4.16]. However, a quantitative comparison between the observed defect concentrations and capture cross-sections found that the N2 defect does not easily explain many device characteristics[1.4.17]. Specifically, it was found that a very large capture cross section for electrons $\left(\sigma_n = 2\times10^{-13}cm^2\right)$ was needed to explain the device open circuit voltage which would in turn required a bulk diffusion length below 0.3um. Given the good carrier collection typically observed in CIGS solar cells, this low value seems unlikely. Furthermore, the hole capture cross-section for this defect is only $\sigma_p = 2\times10^{-15}cm^2$. Acceptor-like defects typically have larger capture cross-sections for holes than electrons due to their columbic attraction. One proposed explanation is the density of the N2 defects increases towards the CIGS/CdS interface and therefore AS measurements underestimate the actual defect concentration[1.4.17].

One additional complication/problem with correlating device performance with the N2 defect is that the N2 defect is metastable. It has been found that both light and forward bias causes a reduction in shall electron traps and an increase in the N2 defect[1.4.18]. Furthermore, the increase in the N2 defect concentration is connected to an increase in the free hole concentration in the film[1.4.18]. This metastability has been used to explain the apparent increase in open circuit voltage of CIGS devices upon light-soaking[1.4.19,1.4.20]. We note that the observation of forward bias increasing the device open circuit voltage and N2 defect concentration suggests the N2 defect concentration is not responsible for device performance. A detailed investigation of the N2 defect and its metastabilities have attributed its origin to a V_{Se}-V_{Cu} complex[1.4.21].

The lack of correlation between defect densities and device performance has made it difficult to develop theories describing what fundamentally controls recombination current in CIGS solar cells. As shown in the previous section, there are four primary areas within a solar cell where recombination can take place: the interface, space charge region, quasi-neutral bulk and back surface. Furthermore, within those areas the recombination can be further subdivided into recombination through bulk defects, grain boundaries or interface states.

Interface recombination was initially suspected to be responsible for determining the open circuit voltage of devices[1.4.22]. This was thought to occur due to the comparable doping on the CdS and CIGS side of the device resulting in the Fermi-level being close to midgap at the CdS/CIGS interface. As discussed in the previous section, recombination is most likely to occur where the Fermi-level is at midgap due to the high concentration of both electrons and holes. As interfaces are typically highly defective, it was proposed that recombination occurred primarily at this interface. However, the current device structure only uses a thin CdS layer and is therefore closer to an n+p heterojunction where the Fermi-level at the CdS/CIGS interface is closer to the CIGS conduction band[1.4.23]. Furthermore, it has been observed that the bandgap at the surface of CIGS films is increased relative to the bulk due to a substantially lower Cu concentration, giving rise to an ordered defect compound at the surface[1.4.24]. This would further reduce the impact of interface recombination by lowering the minority-hole density at this interface. However, there is no definitive proof that recombination at the CdS/CIGS interface is not responsible for the forward current in the device.

Alternatively, it has been proposed that recombination in the space charge region is responsible for device performance. It has frequently been observed that the ideality factor in CIGS solar cells lies somewhere between 1.2 and 2[1.4.25], although there are frequent cases where the ideality factor exceeds 2[1.4.26]. The ideality factor greater than 1 would suggest from the ideal diode theory that recombination is occurring primarily in the space charge region. Furthermore, it was observed that the diode ideality factor frequently increases as the temperature of the cell is decreased. To explain these effects, it has been proposed that recombination in CIGS occurs in the space charge region via trap states exponentially decaying from the band edges into the bandgap which can be enhanced at low temperatures by tunneling[1.4.26].

However, beyond the observations of ideality factors greater than 1, there exists little direct evidence that recombination occurs primarily in the space charge region. Furthermore, recent time resolved photoluminescence (TRPL) measurements on CIGS samples from NREL indicate minority carrier lifetimes of up to 250ns[1.4.27]. Generally, recombination in the space charge region should dominate only for low quality absorbers. To illustrate this, the open circuit voltage versus minority carrier lifetime was numerically calculated based on the previously presented equations and assuming a bulk mobility of 10cm^{2}V^{-1}sec^{-1}, back surface recombination velocity of 10^{3}cm-sec^{-1} and a constant density of midgap states in the CIGS. The results of the calculation are shown in Fig. 1.16. It is apparent from this graph that one would expect the recombination to occur primarily in the quasi-neutral bulk once the minority carrier lifetime exceeds 10ns. Therefore, it is not

immediately apparent why the ideality factor of high quality devices is not closer to 1.

Recent publications have offered an alternative explanation for the high ideality factors. First, any form of non-uniformity in the device can lead to ideality factors greater than 1. In the simplest case, the geometry of the finger pattern across the cell combined with the finite conductance of the TCO leads to a distribution of voltages across the cell. As each point on the cell is effectively under a different bias, the assumption of an equipotential front contact in the ideal diode equation is no longer valid and as a result the measured diode ideality factor can increase. This mechanism essentially describes the high ideality factor as an artifact of the equivalent circuit being used to fit the current-voltage curve.
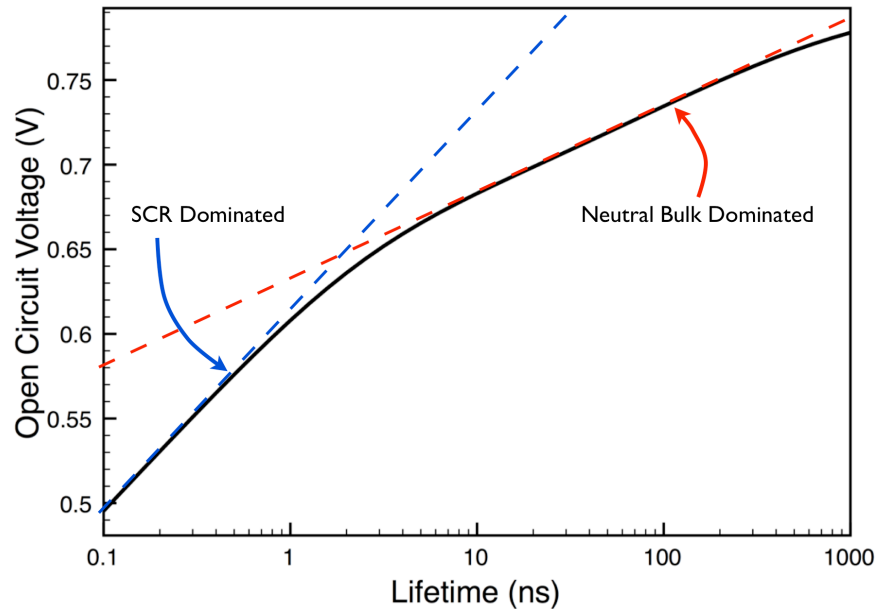
Fig. 1.16: Open circuit voltage versus minority carrier lifetime in a CIGS sample with 30% gallium and a uniform midgap defect concentration. At low lifetimes, the open circuit is dominated by recombination in the space charge region while at high lifetimes, it is dominated by recombination in the quasi-neutral bulk.

A second origin of non-uniformities are lateral variations in any of the key electrical properties affecting the diode current. These non-uniformities lead to different parts of the device having different current-voltage characteristics. As a result, the superposition of all the individual current-voltage curves leads to an increase in the diode ideality factor. Lateral non-uniformities in electrical properties have been observed on CIGS solar cells over several lengths scales using techniques such as photoluminescence (PL)[1.4.28], cathodoluminescence (CL)[1.4.29], scanning tunneling microscopy[1.4.30] and photocapacitance spectroscopy[1.4.4]. However, it has generally been difficult to quantitatively describe the effect of these non-uniformities on the diode ideality factor.

Finally, it has also been proposed that small scale electrostatic non-uniformities can lead to a large increase in the diode ideality factor[1.4.31]. In this model, the electrostatic non-uniformities are screened upon illumination/forward bias leading to a large ideality factor. This theory therefore implies that

recombination is occurring in the quasi-neutral bulk of the CIGS and the high ideality factor occurs as a consequence of electrostatic non-uniformities[1.4.31].

Ultimately, there is no consensus as to where recombination occurs in CIGS solar cells. This information is not only of scientific interest but is key to improving device efficiencies. Therefore, it is useful to consider the specific features of the highest performance devices for clues as to what ultimately controls recombination in high efficiency CIGS solar cells.

There are at least two unique features of high quality CIGS solar cells. First, these cells feature CdS/IZO buffer layers, which from a current collection standpoint should be detrimental to device performance due to parasitic absorption. Therefore, one would assume these layers are necessary to obtain very high open circuit voltages to offset their negative impact on device current. Second, these cells exhibit a pronounced bandgap grading through the depth of the absorber. In an ideal solar cell, the existence of a bandgap grading is detrimental to device performance, as the open circuit voltage will be fixed by the lowest bandgap section of the device leading to current losses stemming from incomplete absorption. Therefore, any theory of recombination in CIGS solar cells should offer an explanation for these two features.

The first point, the existence of a CdS/IZO buffer layer, has been justified in several ways[1.4.23]. First, the CdS deposition occurs in a low temperature chemical bath, which may exhibit better interface properties than a sputtered ZnO/CIGS interface. Second, the IZO buffer layer increases the stack resistance of the device, which can limit the amount of current traveling through the cell. In a 1D device, such an effect would be detrimental to performance by reducing the fill factor of the device. However, it has been proposed that in the presence of 2D lateral non-uniformities, stack resistance can be beneficial by limiting the amount of current that can flow through any weak diode[1.4.32, 1.4.33]. For this reason, it has been theorized by several groups that lateral non-uniformities in bandgap, defect density and free carrier density limit the performance of CIGS solar cells[1.4.28,1.4.30,1.4.31,1.4.34]. Furthermore, some groups have proposed that these non-uniformities have reached their theoretical minimum making it difficult to expect large improvements in device performance in coming years[1.4.31].

The second observation of a non-uniform bandgap gradient has been explained in two ways. First, the increase in gallium concentration towards the back of the cell should result in a quasi-electric field, which aids in the collection of photo-generated minority carriers. Therefore, it has been proposed that the increased carrier collection offsets the decreased photon absorption resulting in an improvement of the device current[1.4.35]. Additionally, an increase in gallium concentration towards the back of the sample has also been credited with reducing the impact of the back surface recombination velocity on the device open circuit voltage[1.4.36]. The increase of gallium concentration towards the front of the sample has also been credited with increasing the device open circuit voltage by minimizing the recombination in the space charge region[1.4.37]. However, it's unlikely that both of these explanations are true at the same time for the same device given they point to the dominant recombination occurring at both the front and very back of the device.

Therefore, the purpose of this work is to develop new techniques to quantitatively determine the spatial variation in electronic properties in thin film photovoltaics both in-depth and laterally across the sample and their influence on device properties. In doing so, it will be possible to isolate the areas of the solar cell responsible for efficiency losses which will in turn provide fundamental insights into the properties of CIGS. As shown in the preceding sections, there are several open questions regarding the physics of CIGS solar cells including what impact the gallium gradient has on the device operation and what role lateral non-uniformities play in limiting device performance.

This work focuses on samples obtained from the National Renewable Energy Laboratory grown using vacuum co-evaporation. However, it's important to note that there are frequent contradictions in experimental data obtained by different laboratories around the world. Therefore, it is imperative to develop techniques and analysis methods that are applicable to all types of thin film photovoltaics and restrict the conclusions to the devices being measured.

2   Depth Dependent Electronic Properties

2.1   Background

Thin film photovoltaics inherently have depth dependent electronic properties due to their multi-layer structure. As previously shown in Fig. 1.11, there are multiple recombination pathways along the depth of the film that can affect device performance. One of the most important features of a solar cell is the ability to collect photogenerated carriers. For this reason, it has been shown both theoretically[2.1.1] and experimentally[2.1.2] that the carrier collection efficiency of a cell can be improved by intentionally modifying the electronic properties as a function of depth through compositional grading. However, there are currently no established characterization techniques that can extract key electrical parameters such as the minority carrier diffusion length in thin film photovoltaics featuring compositional gradients.

The minority carrier diffusion length is one of the most critical parameters in a solar cell for device performance. As previously shown, maintaining a high diffusion length and low back surface recombination velocity is critical for collecting photo-generated carriers and minimizing forward current. Two established techniques for determining the minority carrier diffusion length in a compositionally uniform solar cell are measuring the sample external quantum efficiency (EQE) and electron beam induced current (EBIC). The basic experimental setup for these two techniques is shown in Fig. 2.1. The techniques are fundamentally very similar in that both generate a known number of excess carriers in the solar cell, which is then compared to the photocurrent to determine how many of the carriers were collected.

Mathematically, the purpose of both techniques is to determine the carrier collection probability as a function of depth $(F(z))$[2.1.3]. This can be determined by the following expression for the quantum efficiency (QE):

$$QE = \frac{\int_0^D F(z)g(z)dz}{\int_0^D g(z)dz}, \tag{2.1}$$

where D is the combined thickness of the ZnO, CdS and CIGS layers and $(g(z))$ is the carrier generation rate as a function of depth. In order to determine the depth dependent carrier collection probability, it is necessary to vary the carrier generation rate as a function of depth. In external quantum efficiency measurements, the generation function is varied by selecting different wavelengths of light to probe deeper into the sample[2.1.4]. In electron beam induced current, the generation function is modified by changing the electron beam accelerating voltage, as will be explained latter[2.1.5]. The exact shape of the generation function is different for the two techniques and is shown qualitatively in Fig. 2.1.
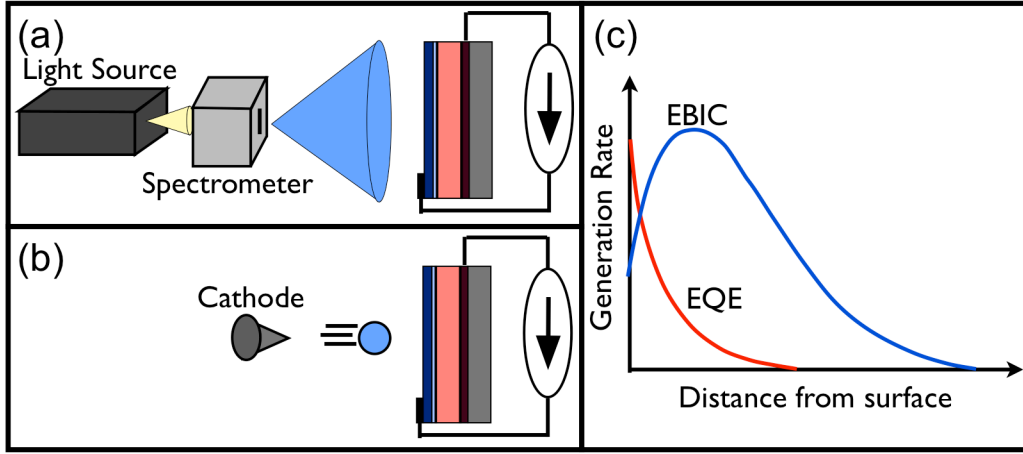
Fig. 2.1: (a) Setup of an external quantum efficiency (EQE) measurement. A narrow band of light is selected by a spectrometer from a broad band light source and directed at the sample. The measured current is compared to the incident photon flux to determine the quantum efficiency. (b) Setup of an electron beam induced current measurement (EBIC). Here, the excess carriers are generated by high energy electrons directed at the sample surface. The measured current is compared to the number of excess carriers generated in the semiconductor layers. (c) Comparison of the carrier generation rate as a function of distance from the surface for the two methods.

EQE and EBIC measurements have previously been performed on CIGS solar cells. EQE measurements have indicated bulk diffusion lengths on the order of 0.7μm[2.1.6]. However, the problem with EQE measurements is that they are very sensitive to the absorption coefficient of the absorbing layer, as this ultimately determines the shape of $(g(z))$. This is problematic in high efficiency solar cells since the bandgap is graded along the depth of the film and therefore the absorption coefficient is also rapidly changing along the depth of the film. Furthermore, as the bandgap increases towards the back of high efficiency cells, it can be impossible to generate significant excess carriers at the back of the film by illuminating the cell from the front surface. Some groups have attempted to rectify this by growing films on transparent back contacts, but these devices typically have much lower

efficiencies, suggesting the results are not comparable with high efficiency cells grown on a conventional opaque Mo layer[2.1.7].

EBIC measurements have been performed on CIGS solar cells in the past but only for samples featuring no compositional grading[2.1.8-2.1.10]. Some of these studies had to assume either a carrier collection probability in the CIGS that did not monotonically decrease[2.1.8] or the method of analysis left a wide range of possible fitting parameters[2.1.10]. As will be shown in the following sections, EBIC has several key features making it the ideal technique to study the bulk diffusion length in compositionally graded samples and the effect of quasi-electric fields on carrier collection.

2.2   Electron Beam Carrier Generation Function

The carrier generation function $\left(g(z)\right)$ in electron beam induced current measurements is primarily dictated by the energy of the incoming electron beam and the material properties of the sample. The electron beam energy and material properties directly affect the manner in which hot electrons lose their energy upon entering the material. This interaction can be expressed by the electron energy dissipation function, which describes over what volume hot electrons will lose their energy. For this study, the electron energy dissipation function was calculated for a typical ZnO/CdS/CIGS solar cell structure using the Monte-Carlo simulation program CASINO[2.2.1].

The program simulates an individual electron striking a material and how that electron dissipates energy before it reaches thermal equilibrium. There are two important interactions the hot electron will have with the material. First, the hot electron can elastically scatter off one of the atomic nuclei thereby altering its direction in the material. Second, the hot electron will inelastically interact with the core and valence electrons in the material thereby producing additional free electrons. CASINO models these effects by simulating the path of thousands of electrons entering the sample. The distance between nuclei collisions is calculated based on a random number and mean free electron path[2.2.2]. The scattering angle for each collision is then calculated based on the scattering cross section of the atom involved in the collision[2.2.2]. Between collisions, the electron is assumed to lose some energy per path length in the continuous slowing down approximation[2.2.3]. The program continues to monitor the path of the electron until it either leaves the sample or reaches an energy below 50eV[2.2.1].

The result of these calculations is a three dimensional description of the electron energy dissipation rate. The simulations for a ZnO/CdS/CIGS sample are shown in Fig. 2.2. It is apparent from the simulations that the energy dissipation volume increases as the beam energy increases. This is expected given the higher energy electrons must travel along a longer path before they reach thermal equilibrium. The width and depth of the electron interaction volume are roughly equivalent and around 300nm at 10kV.
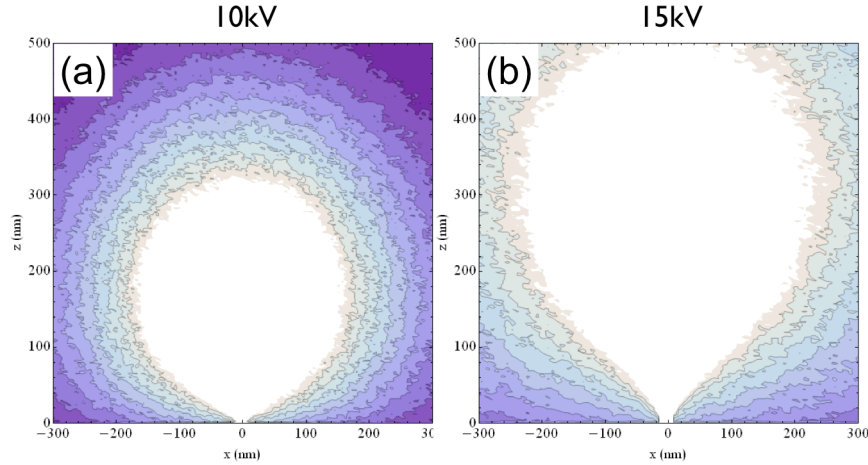
Fig. 2.2. (a) Shape of the energy dissipation function for an incident electron beam (originating from the bottom of the plot) at 10kV. The region in white is >= 5% of the maximum of the dissipation function. (b) The shape of the energy dissipation function for an incident electron beam at 15kV. The interaction volume between the incident electrons and sample increases when the accelerating voltage is increased.

The full three dimensional electron energy dissipation function will be used in Sec. 2.6 to interpret cross sectional EBIC results. However, for the sake of calculation time, it is preferable to have an analytic formula to approximate the energy dissipation function. To our knowledge, there are no accurate formulas for the radial and depth dependence of the energy dissipation function. However, Wu and Wittry[2.2.4] previously published an analytic approximation for the depth dependence of the energy dissipation function, provided the thickness of every layer is normalized by the material density. This approximation works relatively well as the material density is a strong component determining the energy loss per path length for an electron[2.2.2].
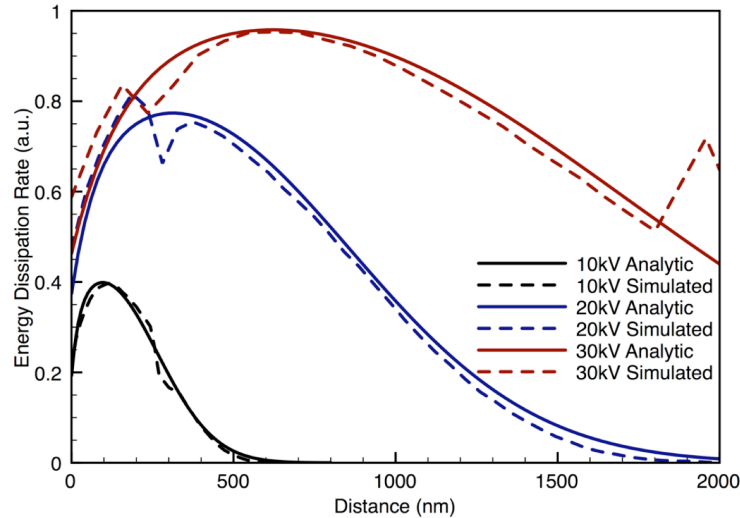

Fig. 2.3. Comparison of the energy dissipation function calculated using an analytical approximation versus Monte-Carlo simulations.

A comparison between the Wu and Wittry approximation and the Monte-Carlo simulation results are shown in Fig. 2.3. The calculations agree very well with one another and therefore the analytic formula given by Wu and Wittry will be used in the subsequent EBIC analysis.

In order to turn the electron energy dissipation function into the carrier generation function $(g(z))$, it is necessary to divide the energy dissipation rate by the mean energy required to generate an electron hole pair $(E_{ionization})$ at every point in the sample. Qualitatively, hot electrons lose their energy in a material either through impact ionization or optical phonon generation, as shown in Fig. 2.4. The carriers generated by each hot electron also have a chance of undergoing additional impact ionization events, until finally the carrier energy is insufficient to generate additional electron hole pairs $(E < E_g)$ and the remaining carrier energy is dissipated as heat.
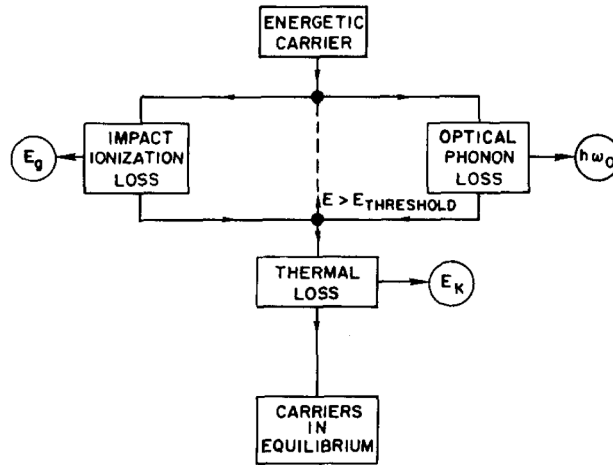
Fig. 2.4. Model of the energy-loss mechanisms for hot carriers in a semiconductor, taken from Ref. 2.2.5.

Theoretical calculations of the average energy to generate an electron hole pair are complicated and depend on many properties of the semiconductor such as the band structure of the material and the phonon properties. However, it has been experimentally shown that the average energy to generate an electron hole pair is linear with the bandgap of the material over a wide range of bandgaps and even with different ionizing radiation as shown in Fig. 2.5[2.2.6]. Therefore, in the following work, we use the empirical relationship[2.2.4]:

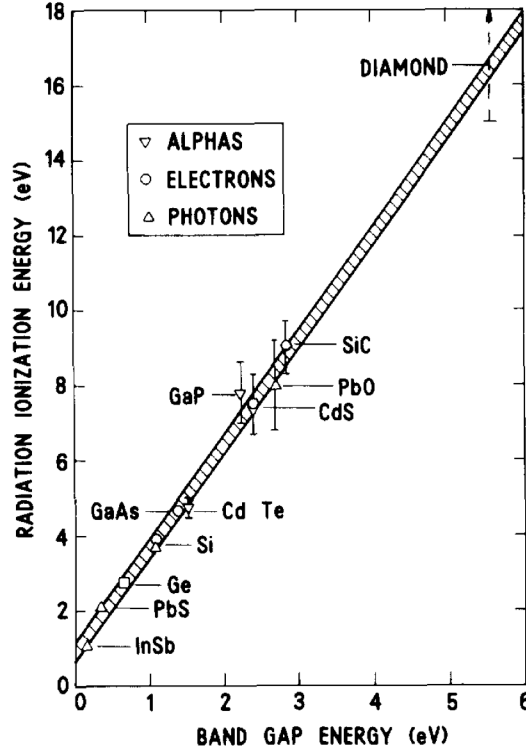$$E_{ionization} = 2.596E_g + 0.714. \tag{2.2}$$

Fig. 2.5. Energy required to generate an electron hole pair versus the bandgap energy for several materials. Previous measurements indicate there is a linear relationship between the material bandgap energy and energy required to generate an electron hole pair. Figure is taken from Ref. 2.2.6.

Finally, the quantitative number of electron hole pairs generated per distance is determined by scaling the carrier generation function by the total carrier generation rate (G_0)[2.2.4]:

$$G_0(cm^{-2}\sec^{-1}) = \frac{6.25 \times 10^{21} V j_b (1-b)}{E_{ionization}},$$ (2.3)

where V is the beam voltage in kV, j_b is the beam current in A/cm^{2} and b is the fraction of backscattered electrons (assumed to be a constant value equal to 0.32[2.2.7]).

Overall, the carrier generation function in a structure is primarily dependent on the incoming electron beam energy, material density and bandgap. The material density does not change significantly between CIS and CGS and furthermore, the change in the carrier generation rate is only linear with bandgap making it easy to calculate the shape of the carrier generation function in a graded bandgap structure. Furthermore, by using an electron beam, it is possible to generate carriers towards the back of a graded film thereby directly probing the influence of quasi-electric fields on carrier collection.

2.3   Carrier Collection Function

Now that the carrier generation function in Eqn. 2.1 is know, it's necessary to determine the carrier collection probability as a function of depth $\left(F(z)\right)$. The carrier collection probability for a p-n junction can be subdivided into two regions, the space charge region and the quasi-neutral bulk. Almost all carriers generated in the space charge region are collected due to the high electric field in the space charge region (evidence for this assumption will be discussed in the experimental results), while carriers generated in the quasi-neutral bulk will have a collection probability determined by how far from the space charge region they are generated and what the bulk diffusion length is in the quasi-neutral bulk. Therefore, in order to accurately extract the bulk diffusion length, it is necessary to know the space charge width of the sample.

The space charge width is most easily determined by measuring the capacitance $\left(C\right)$ of a sample[2.3.1]:

$$C/A = dQ/dV = \varepsilon/W ,$$
(2.4)

where A is the sample area (0.42cm² for the samples in this study). The permittivity of CIGS used in the following calculations is $13.6\varepsilon_0$[2.3.2]. A LCR meter was used to measure the capacitance of each sample and calculate the width of the space charge region. The bias on the sample was swept from -1.0V to 0.6V to obtain a capacitance-voltage (CV) curve. The CV curve could then be used to determine the free carrier concentration profile in the sample through the equation[2.3.3]:

$$p = -\frac{2}{q\varepsilon A^2}\left[\frac{d\left(1/C^2\right)}{dV}\right]^{-1} .$$
(2.5)

However, it is also apparent from Eqn. 2.4 that the sample capacitance is affected by any change in charge as a function of bias. For materials with a low density of deep defects, the change in charge comes almost entirely from the free carriers at the edge of the space charge region. However, in polycrystalline CIGS materials, there are often large numbers of interface and bulk defects which can charge and discharge upon a change in bias as shown schematically in Fig. 2.6. This leads to an increase in the measured capacitance and as a result, an underestimation of the space charge width.
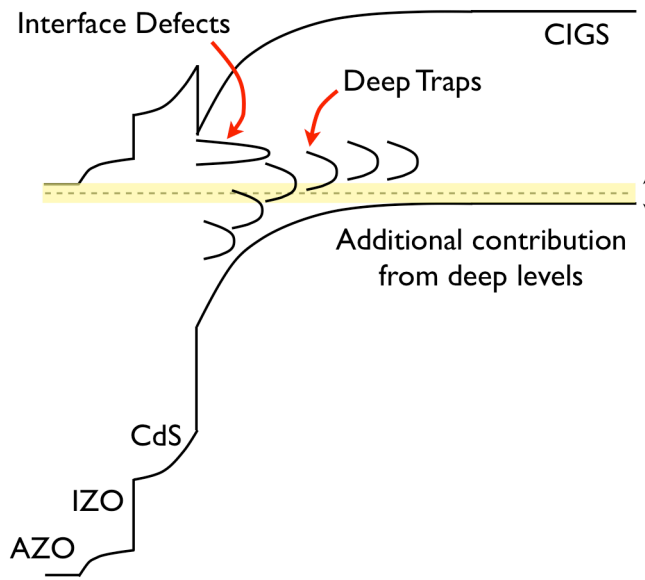
Fig. 2.6: Schematic indicating the influence of deep traps and interface defects on the measured capacitance of a sample. Capacitance measurements are sensitive to both the bulk free carrier concentration of the film and any deep traps near the Fermi-level.

To alleviate this problem, the sample capacitance was measured at high frequencies (100kHz) and low temperatures (-110°C) to reduce the impact of deep defects. In order for a deep defect to contribute to the sample capacitance, it must be able to charge and discharge at a rate faster than the change in applied voltage. By using a high frequency voltage, the deep defects have less time to respond to the change in bias. Furthermore, in order for a deep defect to discharge, the trapped carrier must be thermally emitted into the conduction or valence band. Therefore, by using low temperatures, the deep defects take longer to discharge and contribute less to the measured capacitance. An experimental example of the change in space charge width as a function of temperature is shown in Fig. 2.7 for a CIGS device. The figure shows that the space charge width is underestimated by a factor of two at room temperature due to the contribution of deep levels which are suppressed upon cooling to -110°C.
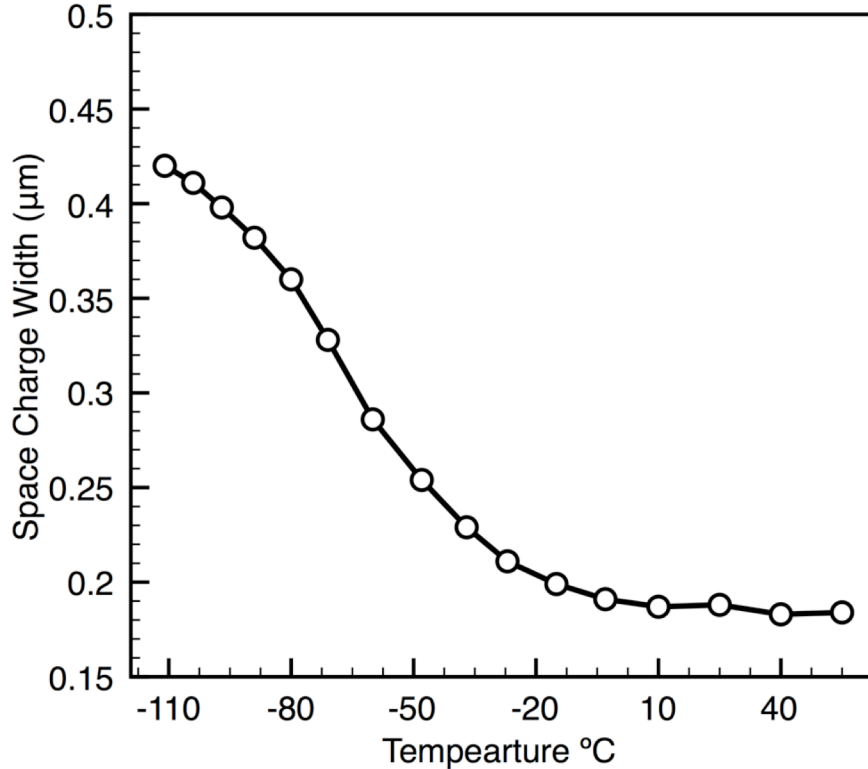
Fig. 2.7: Measured space charge width versus temperature for a CIGS solar cell. The space charge width is underestimated at high temperatures due to the influence of deep levels on the measurement. By lowering the temperature of the device, these levels can be frozen out yielding a more accurate space charge width.

2.4   Influence of Gallium Gradients on Collection

As previously discussed, one of the most intriguing applications of EBIC is to determine the carrier collection efficiency and minority carrier diffusion length in compositionally graded samples[2.4.1]. To study this effect, samples with four different gallium gradients were grown by the National Renewable Energy Lab using vacuum co-evaporation. All four of these samples were grown with similar growth conditions to a thickness of 2µm before being finished by an 80nm layer of CdS grown by CBD and a sputtered bi-layer of IZO/AZO. The gallium to group III ratio was intentionally varied during the growth process to modify the gallium gradient through the film and experimentally determined using secondary ion mass spectrometry. The appropriate calibration factors to convert the gallium and indium counts into atomic ratios were determined using compositionally uniform calibration samples.

The resulting gallium depth profile and associated variation in bandgap along the depth of the film is shown in Fig. 2.8. One sample has a uniform gallium concentration, two samples have a roughly linearly increasing gallium concentrations (Monotonic A and B) and the final sample has a saddle shaped profile, which is standard for high efficiency devices grown by NREL.

In order to properly model the variation in carrier collection efficiency as a function of depth in these samples, it is necessary to include the effects of the

35

gallium gradient induced quasi-electric field, which can aid in carrier collection. As previously shown, the carrier collection probability in the quasi-neutral bulk can be obtained through the reciprocity theorem in Eqn. 1.45. In the case of bandgap gradients, the carrier collection probability is modified by the quasi-electric field as shown in eqn. 1.47. However, this equation only accounts for a sample with a constant quasi-electric field whereas the samples in Fig. 2.8 have the quasi-electric field varying through the depth of the sample. Fortunately, it has been shown that a sample can be subdivided into regions with a constant quasi-electric field, provided the boundary conditions at the front and back of each region are modified[2.4.2].
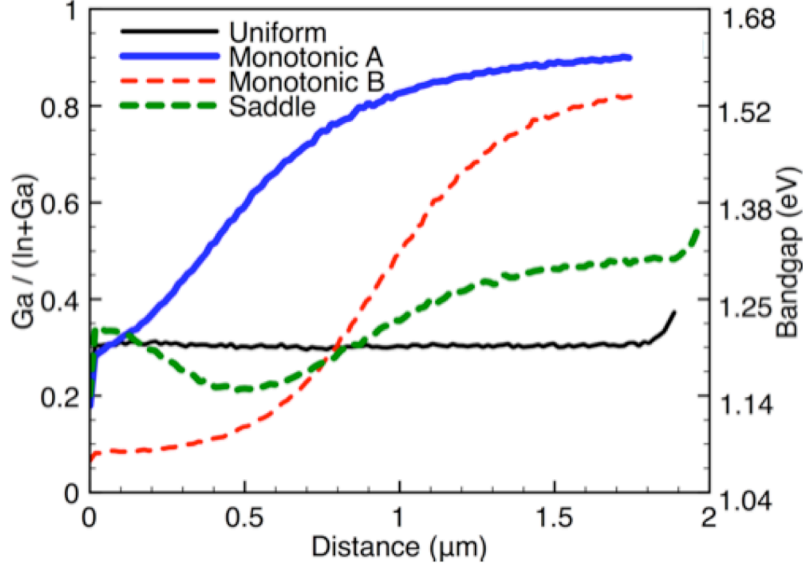

Fig. 2.8: Gallium to group III ratio depth profile as determined by secondary ion mass spectrometry. The right axis shows the expected change in bandgap as a function of depth.

In this case, the gallium gradient as a function of depth through the film was subdivided into three regions with approximately constant quasi-electric fields. The first region's front surface boundary condition is determined by the edge of the space charge region while the back surface is determined by Eqn. 1.43. The second region of the absorber then has the front surface boundary condition specified by the preceding layer and back surface boundary condition specified by Eqn. 1.43. Finally, the last region of the cell has the front surface boundary condition specified by the preceding two sections and the back surface boundary specified by the surface recombination velocity of the CIGS/Mo interface. The end result of this analysis is that each region of the absorber has its recombination properties determined by the properties of all the other regions plus the back surface recombination velocity.

To illustrate the influence of quasi-electric fields, calculations of the carrier collection probability as a function of depth for the four samples with different gallium gradients are shown in Fig. 2.9 assuming a bulk diffusion length of $0.7\mu m$, space charge width of $0.5\mu m$ and back surface recombination velocity to carrier diffusivity ratio of $4 \times 10^4 cm^{-1}$. It is apparent from the calculation that the quasi-

electric fields generated by the gallium depth profile aid in carrier collection compared to the uniform bandgap profile.

The current-voltage characteristics of the four samples with varying gallium gradients were measured with a solar simulator and the results are shown in Fig. 2.10. It is apparent that the varied gallium gradients have a significant impact on device performance by modifying both the short circuit current density and open circuit voltage significantly. Table 2.1 shows the relevant device characteristics as well as the space charge width and bulk diffusion length, which will be discussed in the following sections.
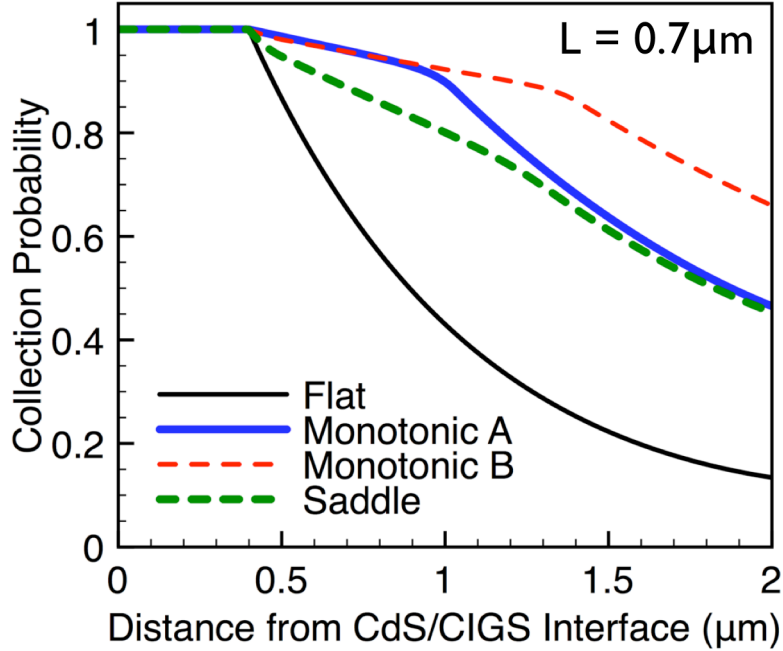
Fig. 2.9: The calculated collection probability as a function of distance from the CdS/CIGS interface for the various bandgap profiles shown in Fig. 2.8. The calculations assume a bulk minority carrier diffusion length of 0.7μm. The variation in collection efficiency as a function of depth is due to the different quasi-electric fields produced by the gallium gradient.

Sample	J_{sc} (mA/cm^2)	V_{oc} (mV)	Fill Factor	Efficiency η	SCR (μm)	L (μm)
Uniform	30.44	656.2	0.769	15.36	0.42	>0.91
Monotonic A	27.97	736.9	0.741	15.27	0.56	0.30
Monotonic B	34.28	666.3	0.752	17.17	0.70	0.35
Saddle	32.16	668.2	0.790	16.97	1.18	0.52

Table 2.1: Solar simulator results showing the operating characteristics of the four devices. The space charge width (SCR) is obtained by the low temperature capacitance of each sample. The minority carrier diffusion length (L) is obtained by the EBIC quantum efficiency versus electron beam voltage.

As previously discussed, the carrier collection efficiency of a solar cell is typically determined using external quantum efficiency. However, the external

quantum efficiency depends strongly on the variation in absorption coefficient through the depth of the film making quantitative analysis difficult. This is illustrated in Fig. 2.11 where the external quantum efficiency is measured on the four samples exhibiting different gallium gradients. In the absence of strong gallium gradients, the long wavelength external quantum efficiency is primarily affected by the bulk diffusion length, space charge width and free carrier absorption from the AZO. However, it is apparent from looking at the Monotonic A sample that there are significant losses in the long wavelength region of the curve, which is most likely due to incomplete absorption originating from the strong gallium gradient. As such, it's difficult to make quantitative statements on the carrier collection properties of these films without resorting to electron beam induced current.
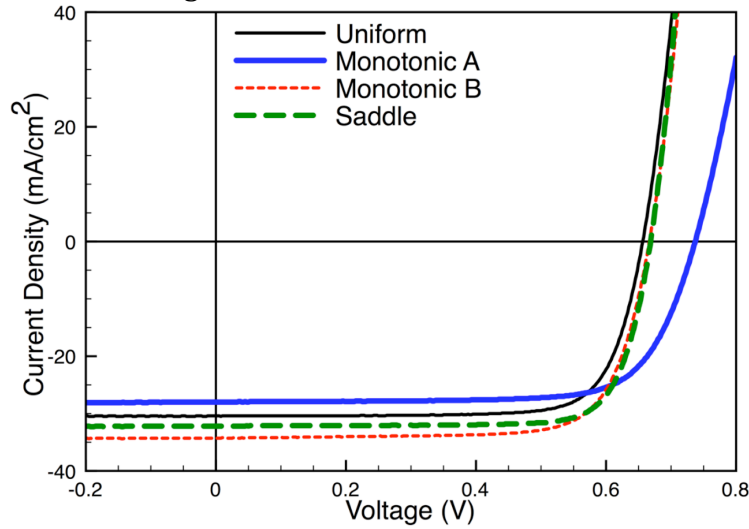

Fig. 2.10: The I-V characteristics of the four samples featuring different gallium gradients.
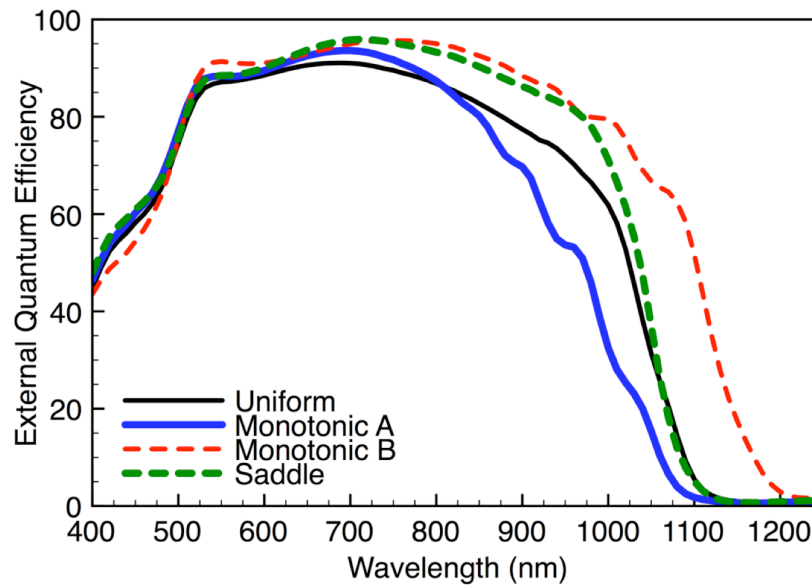

Fig. 2.11: External quantum efficiency plots for the four samples featuring different gallium gradients. It's difficult to determine from these plots which cells exhibit the best carrier collection due to the complicated interaction between the varying collection probability and absorption coefficient.

Energy dependent EBIC measurements were collected for the four samples exhibiting different gallium gradients. The measurements were obtained with a Hitachi SU-1500 scanning electron microscope using accelerating voltages between 4 and 30kV. The EBIC and beam current were measured using a current preamplifier (Stanford Research Systems SR570). The electron beam was intentionally defocused to eliminate the lateral spreading of the generation volume shown in Fig. 2.2. The electron beam current was kept constant at 100pA as measured by a faraday cup mounted on the specimen holder. The electron beam current was kept low to ensure low injection conditions $\left(\Delta n < p_0\right)$ as verified from the linear relationship between the electron beam current and measured EBIC.

As previously discussed, it is necessary to measure the space charge width to accurately calculate the bulk diffusion length in each sample. The space charge width and depth dependent free carrier concentration for all four samples is shown in Fig. 2.12. For the purposes of modeling the extracted EBIC data, it was assumed that the collection probability within the space charge region is equal to unity. This is typically a good assumption due to the high electric fields in the space charge region. Furthermore, the EQE plots shown in Fig. 2.11 do not show any evidence of weak carrier collection in the wavelength region between 600 and 800nm. In this wavelength region, under-absorption in the CIGS is typically not a problem and therefore, the only losses come from either reflection or imperfect collection in the space charge region. Given all four samples have close to 90% quantum efficiency in this region, it is reasonable to assume perfect collection within the space charge region.
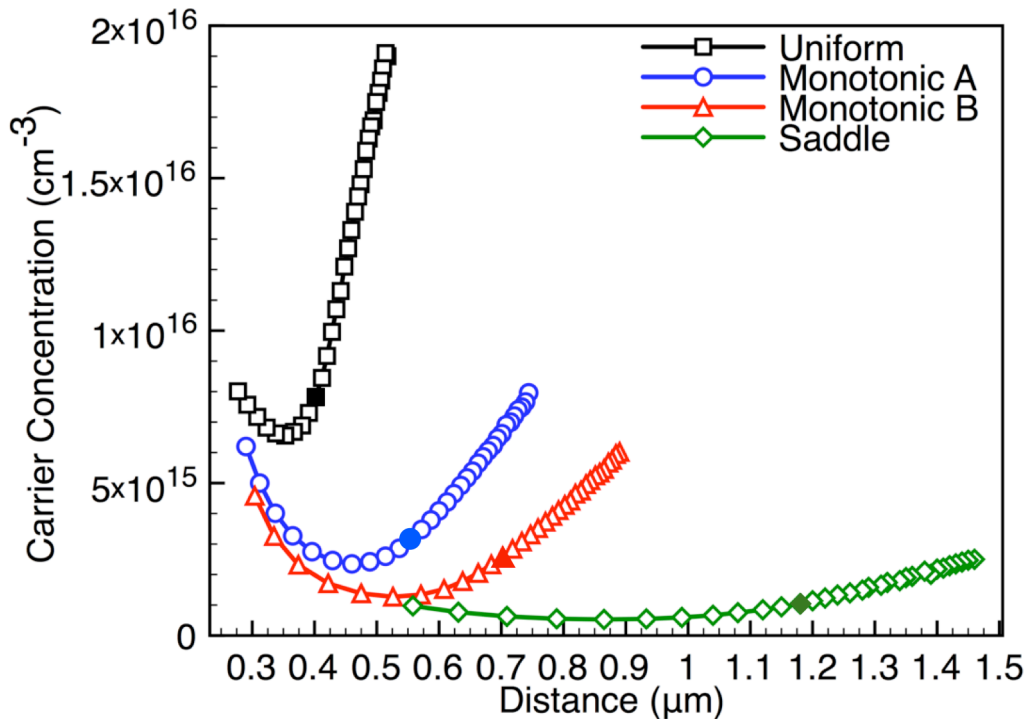

Fig. 2.12. Carrier concentration versus distance for the four samples featuring different gallium gradients as determined by capacitance-voltage measurements at 100kHz and -110°C. The zero-bias depletion width is indicated by a filled symbol.

A constant carrier collection probability of 0 (0.2) was assumed for the ZnO (CdS) layers. To fit the measured EBIC versus beam voltage, the carrier diffusion length for each sample was allowed to vary while the electron mobility was fixed at 100cm^2/Vsec and the back surface recombination velocity was set at 10^5 cm/sec. Finally, the simulated EBIC quantum efficiency (eQE) curve was scaled by a constant factor to account for the shunt resistance of the cell. The shunt correction factor is necessary given the input impedance on the current preamplifier can be on the order of the shunt resistance of the cell. However, for these four high quality CIGS solar cells, the shunt correction factor was typically negligible and modified the simulated eQE curve by less than 5%.

The measured eQE and fitted quantum efficiency are shown in Fig. 2.13. It is apparent from these figures that good fits can be obtained using this methodology even for samples with very strong compositional gradients. The EBIC quantum efficiency curves show measureable differences between the four cells, even though all four exhibit high efficiencies (over 15%). The two highest efficiency cells with monotonic B and saddle profiles exhibited the highest quantum efficiencies with the least falloff at high beam voltage. The falloff at high beam voltage is most strongly dependent on the composition gradient and minority carrier diffusion length. This effect is most easily seen in Fig. 2.14 where the collection probability remains high towards the back of the sample. The monotonic A sample also features a large composition gradient, but most of it is located towards the front of the sample thereby reducing its benefit for carrier collection. The uniform sample suffers from a reduced collection probability due to the lack of a composition gradient.
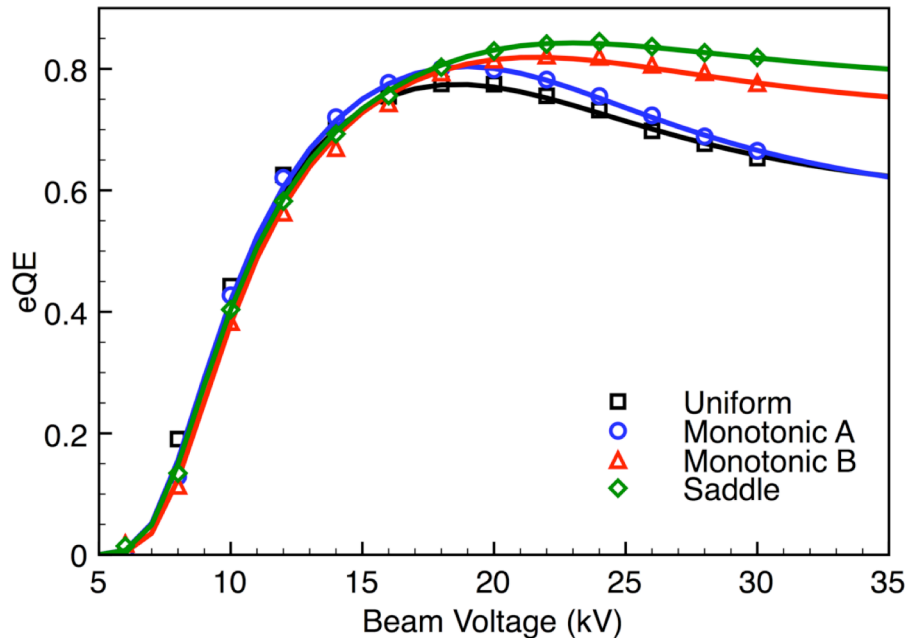

Fig. 2.13: The EBIC quantum efficiency (eQE) versus electron beam voltage for the four samples featuring different gallium gradients. The symbols show the experimental data while the solid lines are theoretical fits.
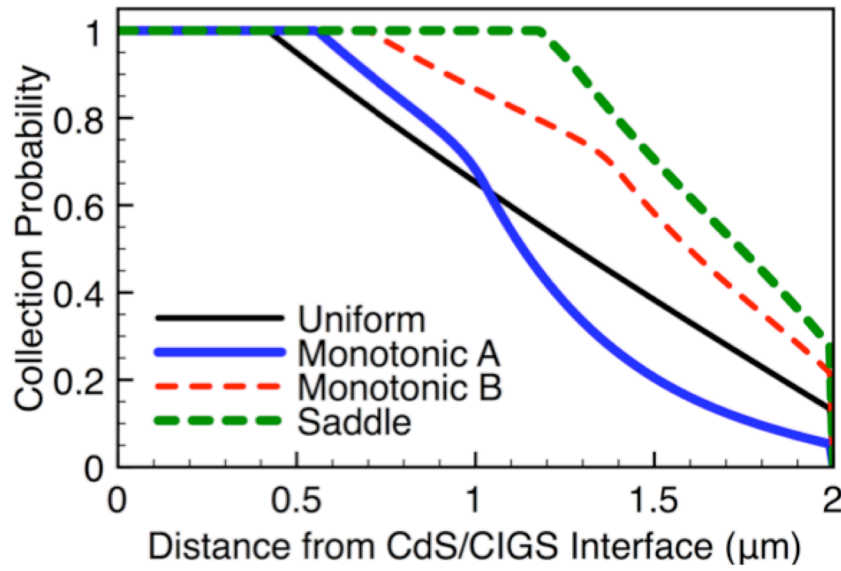
Fig. 2.14. The carrier collection probability as a function of distance from the CdS/CIGS interface for the four samples featuring different gallium gradients. These carrier collection probability functions were used to generate the theoretical fits in Fig. 2.13.

The minority carrier diffusion lengths used to simulate the quantum efficiency plots are shown in Table 2.1. The two samples with the largest gradients have diffusion lengths of 0.3 and 0.35 μm, while the saddle shaped sample has a diffusion length of 0.52 μm. The uniform sample has a diffusion length on the order of the film thickness, such that its collection probability is primarily determined by the back surface recombination velocity. Previous experiments have suggested an extremely high back surface recombination velocity to carrier diffusivity ratio $(S_{Mo}/D_e) \geq 10^7 cm^{-1}$[2.4.3]. However, this experimental result for the uniform sample sets an upper limit of $4 \times 10^4 cm^{-1}$ for the S_{Mo}/D_e ratio. Furthermore, some samples discussed in Sec. 2.7 indicate an even lower back surface recombination velocity.

Energy dependent EBIC is an accurate method to determine small diffusion lengths. However, it is less reliable when the diffusion length is on the order of the film thickness as it is necessary to assume some S_{Mo}/D_e ratio. This is most pronounced for the uniform sample where the diffusion length can range from 0.91 μm to the film thickness depending on which S_{Mo}/D_e ratio is used. On the other hand, the choice of S_{Mo}/D_e ratio has no effect on the monotonic samples due to their lower diffusion lengths and compositional grading. It should be noted that other techniques used to determine the carrier diffusion lengths via collection efficiency (such as external quantum efficiency) have the same limitations. It was found that errors in the measured ZnO thickness and space charge width have the most influence on the EBIC fitting. For the monotonic A sample, a 10% error in the measured ZnO thickness or space charge width would change the diffusion length by roughly 6%. All other assumptions (carrier mobility, CdS collection efficiency, etc.) used to fit the monotonic A data were found to affect the diffusion length by less than 1%. However, as the back surface gallium gradient is diminished, these

assumptions have a larger influence on the EBIC fitting due to the increasing effect of the back surface.

In summary, the energy dependent EBIC measurements shown here on samples with different gallium profiles provide direct evidence that quasi-electric fields due to the compositional grading are beneficial for improving carrier collection and reducing the impact of back surface recombination. It is also interesting to note that the increased amount of compositional grading also lowers the minority carrier diffusion length thereby making the grading less beneficial for charge collection than if the material quality remained the same. However, the next section will show that the diminished bulk diffusion length in compositionally graded samples may not be detrimental to the performance of CIGS solar cells.

2.5   Influence of Gallium Gradients on Forward Current

The extension of electron beam induced current to compositionally graded materials provides an additional opportunity to look beyond the effect of compositional grading on current collection and into how the grading affects the device open circuit voltage. As was previously discussed, the device open circuit voltage is obtained when the short circuit current is equal to the forward diode current. The forward diode current can occur due to recombination in several regions of the cell such as in the space charge region or within the quasi-neutral bulk of the CIGS layer.

The development of compositionally graded samples was historically driven by maximizing device efficiency and it is only after the fact that researchers have attempted to explain why this growth method results in higher efficiency cells. As has been discussed in Sec. 1.4, the influence of the bandgap gradient on device open circuit voltage has been simulated by several groups using different input parameters leading to different conclusions. It is fairly simple to understand at least qualitatively why a saddle shaped bandgap profile could be good for the open circuit voltage without resorting to finite element simulations.

First, the interface recombination velocity between CdS and CIGS is a strong function of the bandgap at the surface[2.5.1]. Therefore, one possible explanation for the improvement of device performance through bandgap gradients is that the increase in gallium content towards the front of the cell raises the interface bandgap thereby reducing the recombination current. Second, recombination through the space charge region is also sensitive to the bandgap at the point of maximum recombination (Eqn. 1.24) and therefore increasing the gallium content towards the front of the cell would again be expected to improve performance. Third, recombination in the quasi-neutral bulk is a function of the quasi-electric field in the bulk (Eqn. 1.40) and therefore the increase in gallium composition towards the back of the cell would serve to reduce quasi-neutral bulk recombination. Finally, the influence of the back surface recombination velocity can be strongly diminished by the quasi-electric field towards the back of the cell, which helps to repel minority electrons from this defective interface (Eqn. 1.40).

To help differentiate these various theories, samples with the saddle shaped gallium profile were grown by the National Renewable Energy Labortory. The cells were first measured with a solar simulator to determine the device

characteristics. A large variation in device open circuit voltage was observed between various cells, making it possible to directly compare the devices to determine what variation in electrical properties was driving the change in device performance. The device I-V characteristics are shown in Fig. 2.15 and summarized in Table 2.2. Table 2.2 shows that two of the devices exhibit a 60mV difference in open circuit voltage from one another.
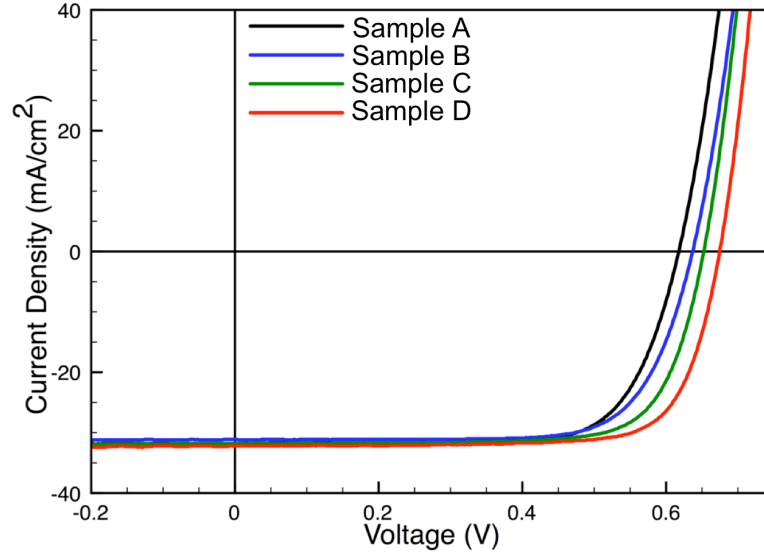

Fig. 2.15: Current-voltage characteristics for four high efficiency samples with a saddle shaped gallium depth profile. The four samples are from the same growth run and therefore had almost identical growth conditions.

Device	Voc (mV)	Jsc (mA/cm²)	Fill Factor	Efficiency η	SCR (µm)	Eg (eV)	L (µm)	L expected (µm)
Sample A	617.4	31.79	0.732	14.36	0.417	1.136	0.82	0.459
Sample B	636.7	31.14	0.733	14.54	0.417	1.135	0.79	0.540
Sample C	652.2	31.82	0.752	15.60	0.479	1.122	0.82	0.789
Sample D	674.3	32.18	0.765	16.60	0.439	1.127	0.98	0.946

Table 2.2: Solar simulator results showing the operating characteristics of the four high efficiency devices. The space charge width (SCR) is obtained by the low temperature capacitance of each sample. The bandgap was determined by extrapolating long wavelength region of the EQE curve to zero. The minority carrier diffusion length (L) is obtained by the EBIC quantum efficiency versus beam voltage. The expected minority carrier diffusion length indicates how much the bulk diffusion length would need to vary to account for the change in device open circuit voltage.

For further analysis, capacitance-voltage measurements were performed on the samples to determine if there was a large change in free carrier concentration between samples. Free carrier concentration would be expected to have a large influence on recombination in the space charge region (Eqn. 1.27), quasi-neutral bulk and back interface (Eqn. 1.40). The free carrier concentration profiles for these four devices are shown in Fig. 2.16. Very little difference in free carrier

concentration is observed between the samples pointing to a difference mechanism underlying the variation in device performance.
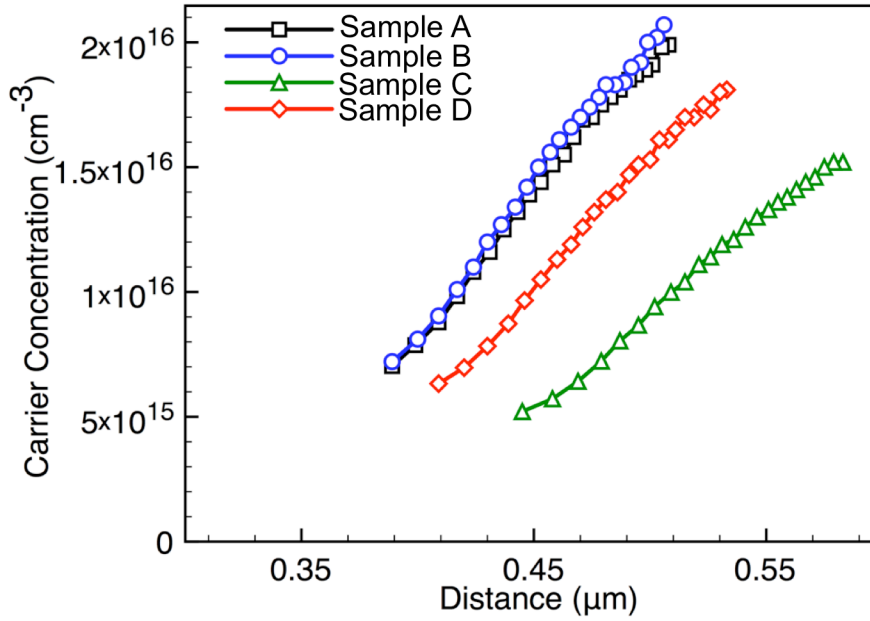

Fig. 2.16: Carrier concentration profiles obtained through capacitance-voltage measurements.

Alternatively, a variation in bandgap from sample to sample could also drive the variation in device open circuit voltage. The minimum bandgap of a sample can be estimated from external quantum efficiency measurements by extrapolating the low energy portion of the QE curve to zero. External quantum efficiency measurements for these samples are shown in Fig. 2.17. In this case, it was found that the samples only exhibited a 20meV variation in bandgap. Furthermore, the lowest bandgaps correspond to the two devices with the highest open circuit voltage, which is opposite to what one would expect if the device performance were driven by changes in bandgap.
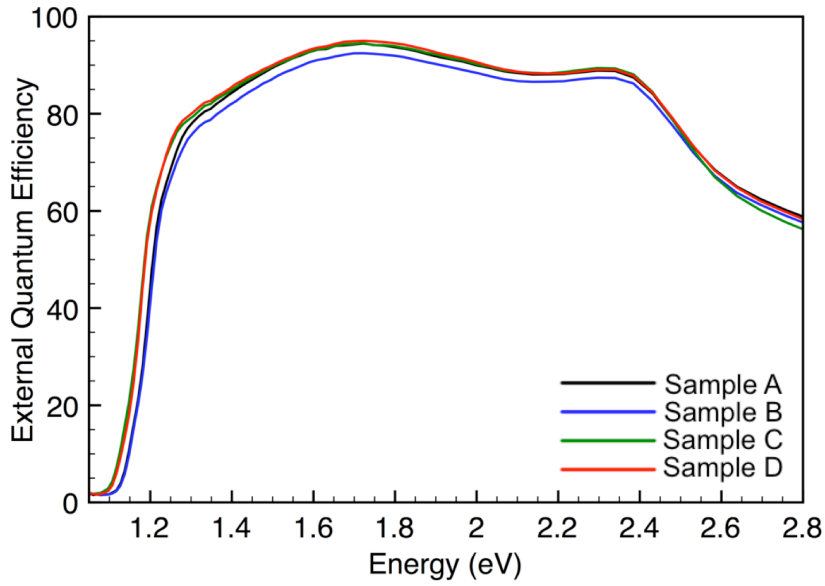
Fig. 2.17: External quantum efficiency measurements obtained for the four high efficiency cells.

Therefore, the simplest explanation for the variation in performance between samples would be variations in the defect concentration and a corresponding change in the bulk diffusion length (Eqn. 1.20 and 1.31). To test this, the minority carrier diffusion length in each sample was measured using electron beam induced current with the analysis being performed in the same manner as the previous section. The EBIC quantum efficiency data for the four devices is shown in Fig. 2.18 and the corresponding bulk diffusion length in Table 2.2. Surprisingly, no significant variation in the carrier collection probability or bulk diffusion length was detected between the samples[2.5.2].

This result has important implications for understanding both the device performance and electronic properties of CIGS. The similar bulk diffusion lengths between all four devices suggests that recombination in the quasi-neutral bulk and back surface is an insignificant factor in determining the device open circuit voltage. This in turn makes it unlikely that the strong gallium gradient towards the back surface of the device has a significant impact on the device open circuit voltage as was previously suggested by some groups[2.5.3]. However, it is important to note that other groups are measuring not only different samples but in many cases samples grown at different laboratories by different growth methods and therefore it's quite possible that different recombination mechanisms dominate the forward current in different cells.
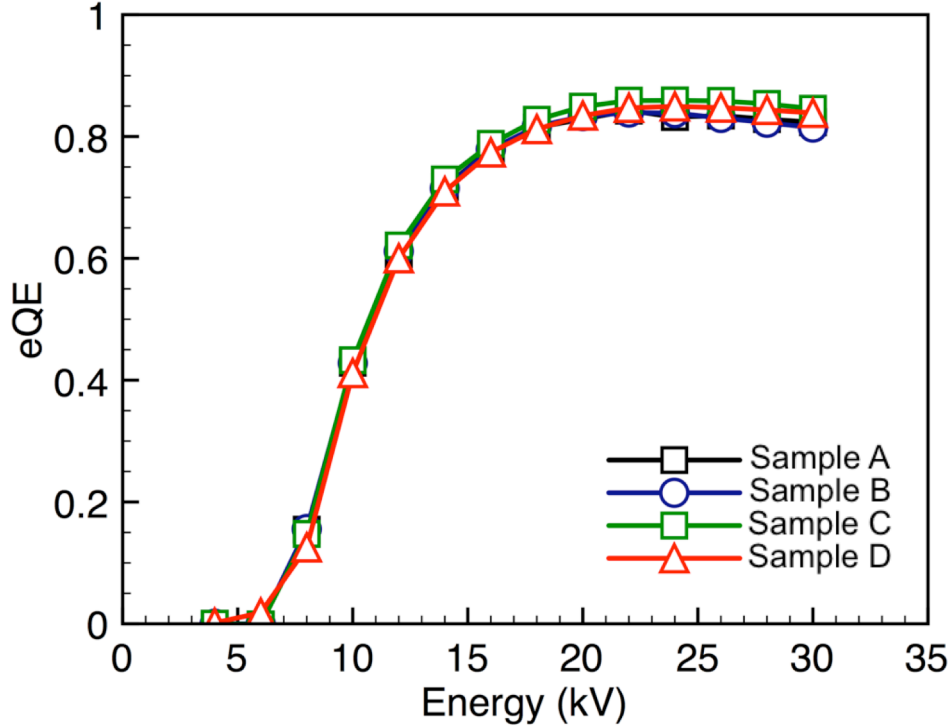
Fig. 2.18: EBIC quantum efficiency versus beam voltage for four high efficiency cells. Despite having open circuit voltages that vary by 60mV, the cells exhibit almost identical carrier collection properties.

Additionally, this result indicates that forward current in CIGS solar cells is not correlated with the bulk diffusion length. Therefore, current collection and open circuit voltage appear to be controlled by separate defects. To illustrate this point, the variation in defect density necessary to account for the wide variation in device open circuit voltage was calculated for each device assuming recombination is primarily in the space charge region (Eqn. 1.25). This defect density was then converted into the expected change in bulk diffusion length (Eqn. 1.31) if the same defects also controlled recombination in the quasi-neutral bulk. The results of this calculation are shown in Table 2.2. The results indicate that one would expect a factor of 2 difference in the bulk diffusion length, which is not observed in the EBIC data.

There are several possible explanations for this effect. First, the CIGS samples are grown in a multistage process, which may result in very different properties throughout the depth of the sample[2.5.4]. Second, it has been observed that CIGS has large lateral non-uniformities in its electronic properties on several lengths scales[2.5.5]. The techniques used here measure the average bulk diffusion length and are not sensitive to these variations, which may dictate device performance[2.5.6]. This second point will be explored in more detail in Sec. 3 where it is shown that lateral non-uniformities in the bulk diffusion length and bandgap are not responsible for the observed variation in device performance. Finally, given the large variety of defects founds in CIGS[2.5.7], it is possible that the traps responsible for recombination in the space charge region do not dominate minority electron

46

recombination in the neutral bulk[2.5.8]. One specific case that has been discussed in the CIGS literature is the V_{Se}-V_{Cu} complex[2.5.9]. This defect has been predicted to exist in two different atomic configurations corresponding to two different electronic behaviors. The transition between these two states is predicted to have a strong Fermi-level dependence and has been connected to persistent photoconductivity in CIGS[2.5.10]. For this reason, one could hypothesize that this vacancy complex controls recombination in CIGS solar cells, but is only a strong recombination center in the space charge region where the Fermi-level position stabilizes the acceptor charge state.

2.6   Cross Sectional EBIC

In addition to the EBIC approach described in the previous section, it is also possible to use EBIC to probe a sample cross section and more directly access the change in collection probability along the depth of the sample. This approach has been used previously on CIGS, as will be discussed below, but no attempts have been made to compare the results from cross sectional to top-down EBIC approaches. Furthermore, this analysis has not been performed on samples exhibiting compositional gradients. The purpose of this section is to provide a direct comparison of the two approaches to both confirm the validity of the top-down EBIC approach and gain additional understanding of the depth dependent carrier collection probability in CIGS samples.

Cross sectional EBIC is inherently a difficult experiment due to sample preparation difficulties and interpretation of the data. Sample preparation is difficult because EBIC inherently requires a working p-n junction with a high sample shunt resistance. Cross sectional EBIC samples are typically prepared by mechanical cleaving, which inherently creates a risk of shunting the device. Furthermore, as will be discussed shortly, the sample must typically be polished in order to prevent surface artifacts from dominating the measurement, which again increases the chance of shunting the sample. Interpretation of the EBIC data is complicated by the shape of the energy dissipation volume discussed in Sec. 2.2 and by the presence of an additional air/CIGS interface which can modify the sample recombination properties. Furthermore, it is unknown if the air/CIGS interface modifies the band bending in the CIGS layer in a manner that would affect the carrier collection probability.

To compare the top-down and cross sectional EBIC approaches, a sample from the same growth run presented in Sec. 2.5 was measured first using the top down EBIC method established in the previous two sections. The sample was then mechanically cleaved by scribing the glass substrate and applying mechanical force to the sample. The sample was then immediately loaded into the scanning electron microscope for EBIC imaging. A representative cross sectional image of the high efficiency saddle profile sample is shown in Fig. 2.19. It is apparent from looking at the image that the EBIC signal varies significantly across the sample and is strongly correlated with the sample topography. This is likely due to a non-negligible air/CIGS recombination velocity combined with the three dimensional surface topology. As a result, electron-hole pairs generated on a grain protruding from the

sample surface will have both a longer path length to reach the space charge region and an increased probability of recombining at the air/CIGS interface.
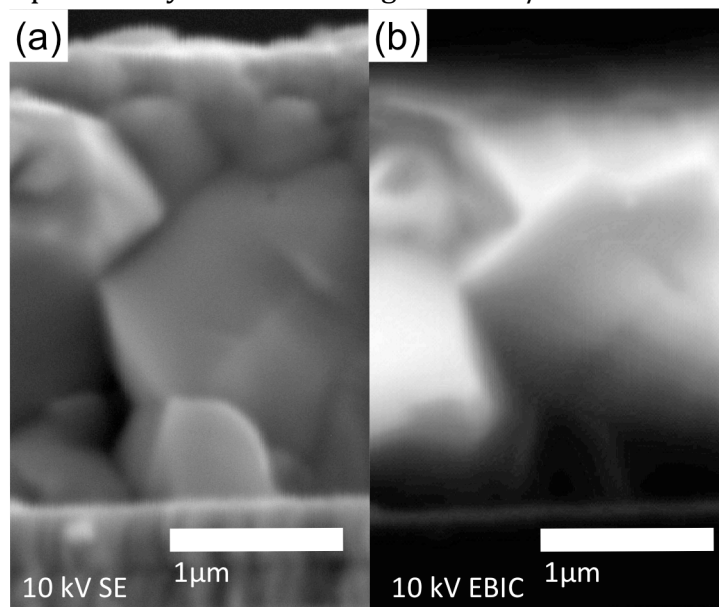

Fig. 2.19: (a) Secondary electron image of a high efficiency NREL sample with a saddle shaped profile. (b) EBIC image of the corresponding region. The EBIC image is strongly influence by the topography seen in the secondary electron image.

As seen in Fig. 2.19, a direct determination of the depth dependent carrier collection probability in cross sectional EBIC images is very difficult for polycrystalline samples due to the strong influence of surface topography. However, this point has not been taken into account in many previous publications. For instance, one previous publication used cross-sectional EBIC images to show that the maximum in carrier collection probability moves into the bulk of the CIGS film when the gallium content is below 30%[2.6.1]. This data point was then used as evidence for surface inversion at the CdS/CIGS interface for low gallium content CIGS solar cells. However, these measurements were carried out on unpolished cross sectional samples making it difficult to determine whether the maximum in carrier collection probability was different between the samples. Furthermore, many additional papers discuss EBIC depth profiles on CIGS samples but make no indication as to the degree of surface roughness on the cross sectional sample[2.6.2-2.6.4].

In order to minimize the influence of surface topography on the EBIC signal, the cross sectional sample was polished using an Argon ion beam for 30 minutes. The sample was loaded with the glass substrate facing the ion beam at a 5° angle to allow the Argon beam to impact the side of the sample. This geometry was found to provide a higher probability of maintaining a high shunt resistance after polishing.

The sample was loaded into the SEM for imaging after argon ion polishing. The polished EBIC image is shown in Fig. 2.20. The impact of surface topology was greatly diminished using this polishing procedure. The EBIC image in Fig. 2.20 shows a high collection probability all the way through the depth of the CIGS

absorber layer. An EBIC line scan through a thin section of the sample is shown in Fig. 2.21. To quantitatively compare this line scan to the top-down EBIC approach, the theoretically expected EBIC line scan was calculated and shown in Fig. 2.21. This theoretical EBIC curve was obtained by convoluting the carrier collection probability determined using the top-down EBIC approach and the electron energy dissipation function simulated using Monte-Carlo methods described in Sec. 2.2. The experimentally obtained EBIC line scan and theoretically simulated line scan show relatively good agreement validating the top-down EBIC approach.
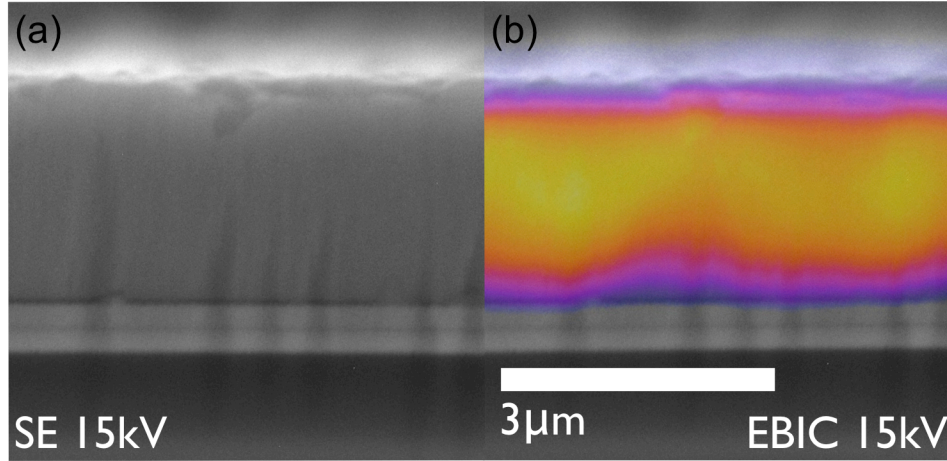

Fig. 2.20: (a) Secondary electron image of the same sample shown in Fig. 2.19 (b) EBIC image overlaid on top of secondary electron image. The EBIC image shows strong carrier collection through the depth of the CIGS absorber.
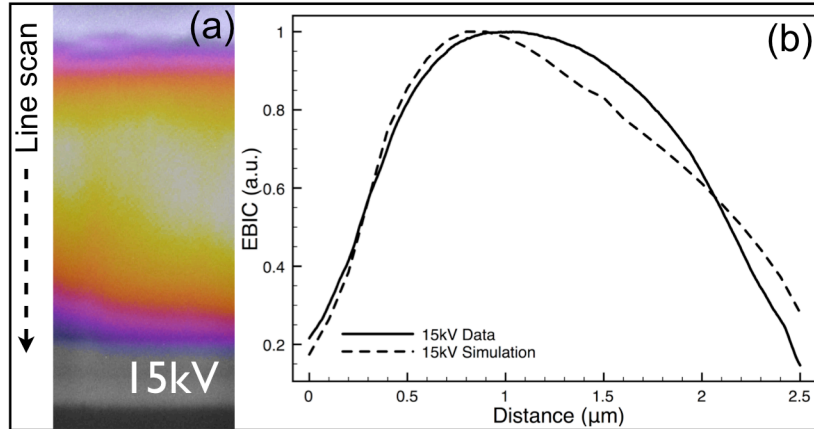

Fig. 2.21: (a) Subsection of the EBIC image show in Fig 2.20. (b) Normalized line scan of the electron beam induced current along the depth of the sample. The dashed line indicates the expected EBIC line scan based on the current collection probability determined in top-down EBIC measurements and the electron energy dissipation volume simulated using Monte-Carlo methods.

However, the close relationship between the top-down EBIC approach and cross-sectional EBIC data is somewhat surprising given that the cross-sectional carrier collection probability should be influenced by recombination at the air/CIGS

surface, which inherently doesn't exist in the top-down sample configuration. To understand the influence of the air/CIGS surface recombination velocity, EBIC images were taken at several beam voltages to generate the electron-hole pairs at a varying distance from the air/CIGS interface. The resulting images are shown in Fig. 2.22. Two things are apparent from these images. First, the region of the sample producing current becomes broader at higher energies, as expected from the increased lateral spreading of the electron beam. Second, at low beam voltages (<10kV), certain areas of the sample produce less current and begin to show features consistent with surface topography variations. This suggests that the air/CIGS interface has a non-negligible surface recombination velocity and therefore, the area imaged during the cross sectional EBIC experiment likely has an even better carrier collection probability than the cross sectional EBIC line scan indicates.
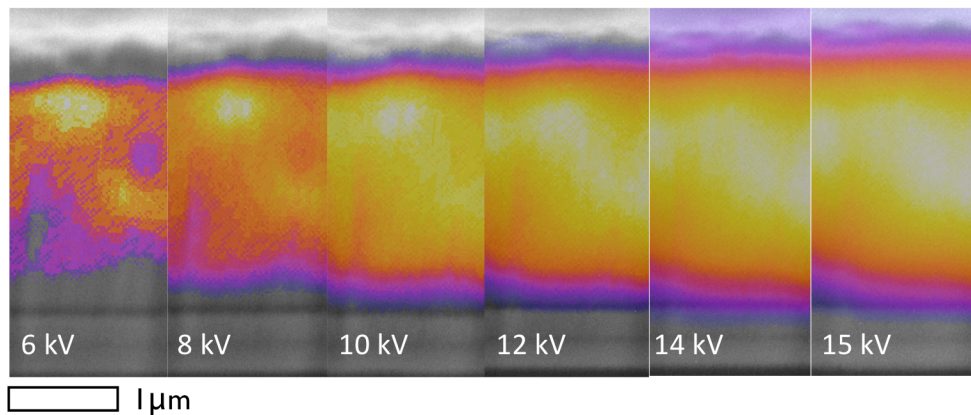

Fig. 2.22: Subsection of the EBIC image shown in Fig. 2.20 taken at different electron beam voltages. Increasing the electron beam voltage increases the width of the EBIC image due to the increased spreading of the electron energy dissipation function. Below 10kV, surface topography affects begin to dominate the EBIC image.

It is important to note that the area analyzed using the top-down EBIC approach is on the order of 100µm x 100µm while the area in one cross sectional EBIC image is only about 5µm wide. Therefore, if the current collection probability is laterally non-uniform across the CIGS layer, one would expect some regions would appear to have better current collection in cross sectional EBIC while others would appear worse. However, on average, the cross sectional EBIC line scans would agree with the top-down approach. This situation is demonstrated in Fig. 2.23 where a region of CIGS is found where the current collection does not extend all the way to the back of the CIGS layer indicating worse carrier collection. However, it is inherently difficult to measure the degree of lateral non-uniformity in current collection using the cross sectional EBIC method given only a very small area of the cell can be polished and analyzed. This makes it difficult to form general conclusions about the degree of current collection non-uniformities. However, it will be shown in Sec. 3.4 that the top-down EBIC approach can be extended to quickly map the carrier collection non-uniformities over an entire sample.
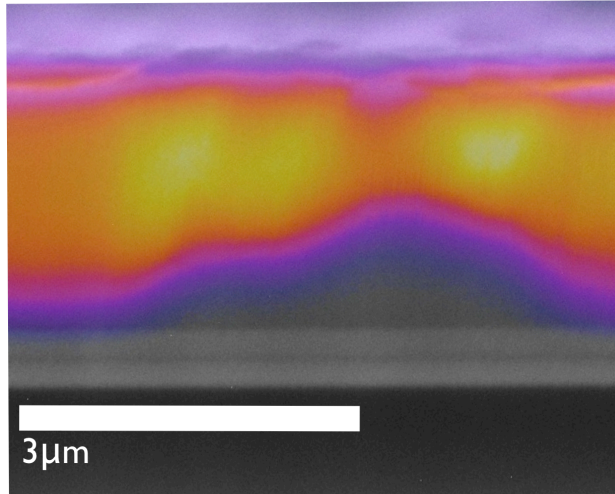
Fig. 2.23: EBIC image taken from a different location on the same sample shown in Fig. 2.20. In this area, the carrier collection probability is reduced indicating laterally non-uniform current collection properties across these CIGS films.

As seen in Fig. 2.22, the CIGS/air interface has some influence on the EBIC profile. It has previously been shown that by changing the electron beam accelerating voltage, it is possible to directly determine the surface recombination velocity at a semiconductor/air interface by fitting the line scans at each beam voltage[2.6.5]. However, this method has previously been used on CIGS solar cells with a uniform gallium profile and it has been found that in many cases, it's not possible to fit the line scans at every beam voltage[2.6.6]. The authors in Ref. 2.6.6 could not explain the lack of fit. However, they did find that the current collection probability varies significantly from grain to grain in a CIGS sample (similar to the variations observed between Fig. 2.20 and Fig. 2.23). Therefore, one likely explanation is that by varying the electron beam energy, carriers are being generated in different grains in the depth of the cross section. Without knowing the full three dimensional microstructure of the sample being studied, it is in most cases not possible to use the method described in Ref. 2.6.5 to correct for the CIGS/air surface recombination velocity.

2.7   Upper Limits on Back Surface Recombination Velocity
        One inherent complication in using a current collection method to determine the minority carrier diffusion length in a thin film sample is the influence of the back surface recombination velocity. In many cases, it is not directly possible to separate a high back surface recombination velocity from a low bulk diffusion length making it only possible to give a range of possible values. Fortunately, two high efficiency samples with the prototypical saddle shaped gallium profile were measured and found to have extremely high collection through the depth of the film making it possible to set a new upper limit on the back surface recombination velocity.
        The I-V characteristics of the two samples in question are shown in Fig. 2.24. It is important to point out the similarity between these two curves and the ones in Fig. 2.15. The short circuit currents in both cases are almost identical indicating that

any change in collection efficiency between the samples has a relatively minor effect on device performance. This can be understood by considering the very high absorption coefficient of CIGS combined with the saddle shaped gallium profile, which in practice leads to the collection of almost every photo-carrier that is generated.
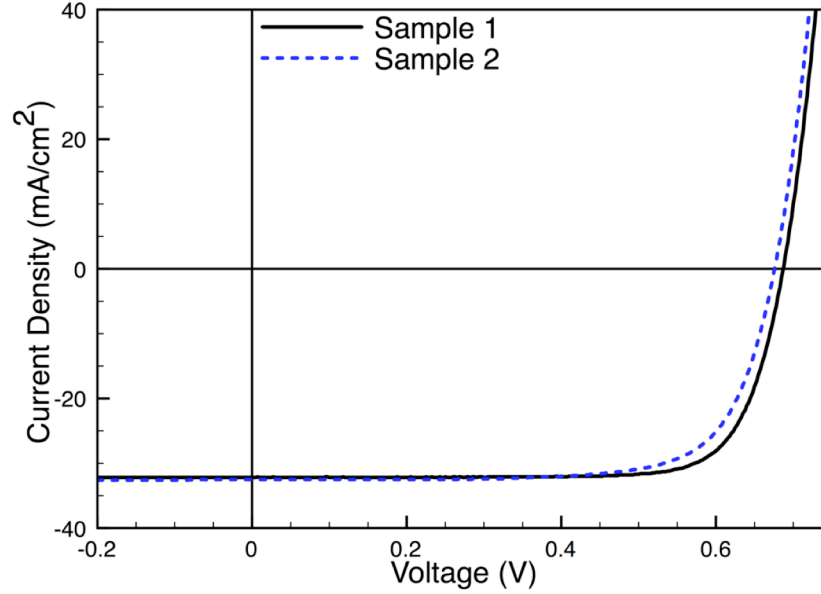

Fig. 2.24. I-V curves for two CIGS samples grown at NREL with the saddle shaped gallium profile. EBIC measurements of these samples indicate nearly perfect collection through the depth of the sample.

However, the samples do show large differences when measured using the top-down EBIC approach developed in the previous sections. The EBIC quantum efficiency data for Sample 1 is shown in Fig. 2.25. It was found that the data could only be fit assuming a diffusion length much larger than the thickness of the film and a back surface recombination velocity below $10^4 \, cm/\sec$. Based on the previous assumption of a bulk electron mobility of $100 \, cm^2/V \sec$, this leads to an upper limit $4 \times 10^3 \, cm^{-1}$ for the S_{Mo}/D_e ratio. Therefore, these results show that for some samples, the back surface has a negligible impact on device performance.
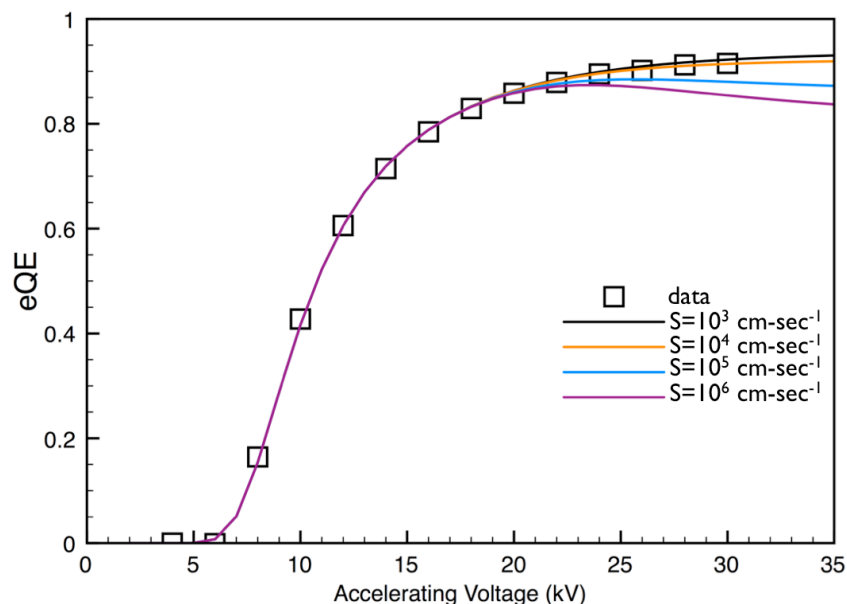
Fig. 2.25: EBIC quantum efficiency curve for Sample 1 shown in Fig. 2.24. The solid lines show fits to the data assuming different values for the back surface recombination velocity.

3 Lateral Variations in Electronic Properties

3.1 Background

Thin film photovoltaics are inherently prone to lateral non-uniformities in their electronic properties. Typical grain sizes in CIGS solar cells are on the order of microns while device areas are on the order of centimeteres. For this reason, no matter what technique is used to deposit the absorber layer, one would expect variations in the current-voltage characteristics across the cell. The physics of non-uniform electronic properties on device behavior has previously been explored by several groups[3.1.1,3.1.2]. These studies have found that lateral non-uniformities in current-voltage characteristics across the cell can significantly lower device efficiencies.

This concept can be easily explained in the case of lateral bandgap non-uniformities. In a given CIGS solar cell, there will be regions of the cell with a below average gallium concentration. Even if all the other electronic properties of the cell were identical, the regions of low gallium content would have a lower bandgap and therefore a higher short circuit and lower open circuit voltage. As all regions of the cell are connnected in parallel, the I-V curve of the entire device will be the sum of the I-V curves of each individual region. The net result on the I-V curve is shown qualitatively in Fig. 3.1 where the whole device has a slightly higher short circuit current than expected but a significantly lower open circuit voltage resulting in diminshed device performance. The same concept can be applied to other electronic non-uniformities such as lateral variations in the free hole concentration or defect concention in the absorber layer. Lateral non-uniformities are always problematic for device performance while intentional non-uniformities along the

depth of the cell (such as the bandgap gradient discussed in the last section) can in some cases be good for device performance.
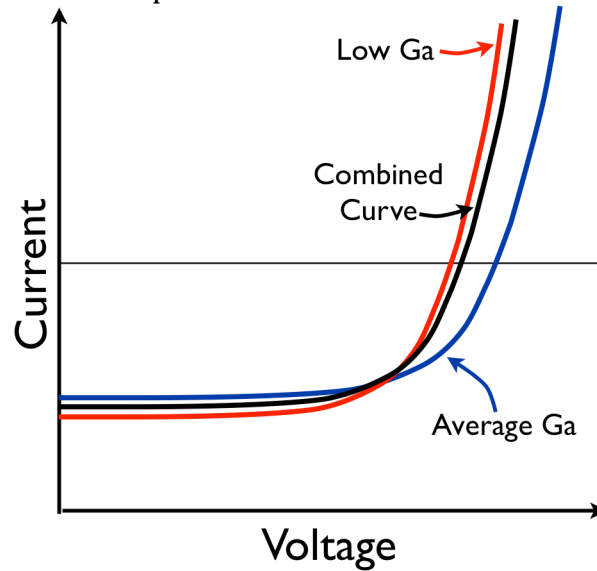

Fig. 3.1: Qualitative I-V curves showing the effect of gallium non-uniformities on device performance. Adding a low gallium cell and average gallium cell in parallel produces an I-V curve with a lower efficiency than the two curves separately.

A common way of treating electronic non-uniformities in solar cells is to subdivide the active area into nodes that are homogenous and can be described by the equivalent circuit in Fig. 3.2. In this way, each node on the cell behaves as if it has uniform electronic properties. The diode at each node is connected in series to a resistor corresponding to the stack resistance provided by the CdS/IZO layers. Each node is then connected to one another in parallel by resistors representing the finite resistance of the AZO layer. It has previously been shown that the prescence of a non-nelgible stack resistance in such a model can be beneficial for device performance by limiting the amount of current that can go through any node in the cell[3.1.3]. This model therefore explains the CdS and IZO layers as being necessary to prevent localized weak diodes from dominating the behavior of the entire cell.
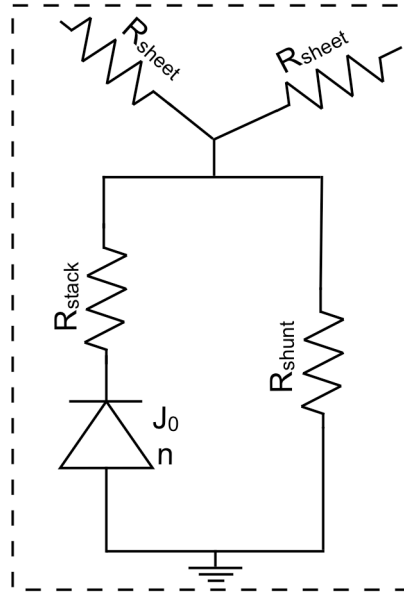
Fig. 3.2: Equivalent circuit of one node in a thin film solar cell. Each node is connected by resistors corresponding to the sheet resistance of the TCO. J_0 and n are the local diode saturation current and ideality factor. Each diode is connected in series with a resistor corresponding to the stack resistance and in parallel with a shunt.

Bandgap fluctuations have theoretically been shown to significantly reduce device efficiencies[3.1.4]. The fluctuations are expected to arise from local variations in atomic concentrations (particularily the gallium to group III ratio) or strain induced bandgap fluctions[3.1.2]. It has also been proposed that CIGS is thermodynamically driven to phase separation into In-rich and Ga-rich clusters around room temperature leading to large efficeicny losses[3.1.5].

Several different techniques have been proposed to measure the bandgap fluctuations in the absorber layer. One approach is to use the photoluminescence (PL) spectra to determine the bandgap distribution in the material[3.1.6]. Ref. 3.4.6 showed that an analytical function can be derived for the PL spectra assuming a Gaussian distribution of bandgaps with a step function absorption coefficient. This method of fitting was applied to PL spectra obtained on high efficiency CIGS samples grown at NREL. A representative spectra and fit are shown in Fig. 3.3 where it's apparent that the local standard deviation of bandgaps is on the order of 30-40meV. This result is typical for PL spectra measured in this work and other reports using this technique have found standard deviations from 15 to 65meV[3.1.6,3.1.7]. However, PL spectra are typically only obtained from a small laser spot making it difficult to make conclusions about the uniformity over the entire sample. Electroluminescence (EL) spectra measurements have been used to circumvent this problem but these measurements do not provide any spatial information about where the non-uniformities are located[3.1.7]. Furthermore, techniques which depend on fitting emission spectra can not differentiate between intentional bandgap non-uniformities along the depth of the film and unintentional lateral non-uniformities.
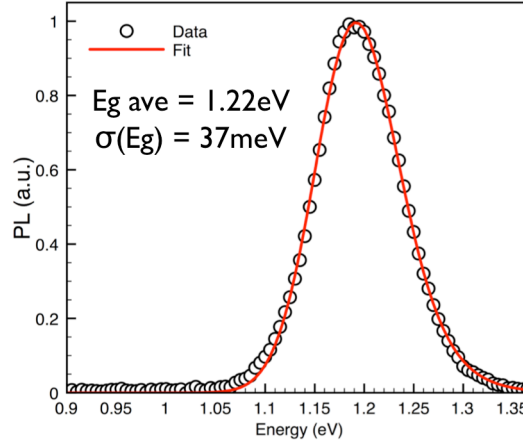
Fig. 3.3: Experimental PL spectrum from a CIGS solar cell. The PL data are fit assuming a Gaussian distribution of bandgaps with a standard deviation equal to 37meV.

Several other techniques have been shown to measure bandgap non-uniformities including photo-capacitance spectroscopy[3.1.8] and scanning tunneling microscopy[3.1.9]. Photo-capacitance spectroscopy measurements also have found exponential bandtails with a characteristic energy dependence around 20meV[3.1.8]. However, these measurements again suffer from not providing any spatial information about the bandgap non-uniformities. Scanning tunneling microscopy experiments have found much larger bandgap fluctuations on the length scale of several atomic spacings[3.1.9]. However, the interpretation of this data is complicated and it's still unclear how much the observed fluctuations affect device performance. Overall, there is a strong need to develop rapid characterizaiton techniques to look at the bandgap non-uniformities across an entire sample in order to properly ascertain whether or not these non-uniformities are strongly influencing the device physics.

Lateral variations in defect concentration across polycrystalline thin-film photovoltaics are also expected to modify device performance. The most common techniques for analyzing defect concentrations involve measuring the capacitance of a sample, which inherently gives a weighted average over the entire device and therefore provides no spatial information[3.1.10]. Similarly, external quantum efficiency measurements have previously been used to measure the bulk diffusion length in thin film solar cells, but these measurements again provide no spatial information[3.1.11].

In order to obtain spatial information about the defect density across a film, it is necessary to either scan a small probe across the sample surface to measure many individual points on the cell or rely on a luminescence based technique which can be directly imaged with a camera. Both approaches have been used to study thin film solar cells. A variety of scanning techniques have been used to measure the electronic properties of CIGS films including photo/cathodoluminescence[3.1.12,3.1.13] and surface photo-voltage[3.1.14] (or electron-beam induced voltage[3.1.15]).

Variations in the photoluminescence intensity and spectra have been observed on CIGS samples on length scales down to 200nm[3.1.16]. These lateral non-uniformities have been related to the splitting of the electron and hole quasi-Fermi

levels under illumination, which in turn are related to the device open circuit voltage[3.1.17]. The differences in quasi-Fermi level splitting across the sample can be deconvoluted between variations in the minorty carrier lifetime and bandgap[3.1.16]. The origin of these fluctuations is generally not known and does not appear correlated with the structural properties of the film[3.3116]. This technique is very useful for looking at non-uniformities, although it has three shortcomings. First, the technique is inherently slow making it difficult to probe the entire sample area. As a result, quantitative comparison between observed non-uniformities and device performance is difficult. Second, at high resolutions, the laser power approaches 10^5 suns and therefore the CIGS can be in high injection conditions where the number of excess carriers exceeds the equilibrium free carrier concentration. In this regime, other electronic properties of the sample such as the majority hole lifetime and auger recombination rates can dominate recombination leading to no correlation between the measurements and device performance[3.1.18]. Finally, PL measurements are done on cells before TCO deposition in order to prevent carrier seperation from dominating the measurements. However, the Fermi-level in the CIGS changes significantly upon TCO deposition. If the defects resposible for recombination are only active when the Fermi-level moves away from the valence band[3.1.19], PL measurements on CIGS or CIGS/CdS layers will not be representative of the defect density when the solar cell is in operation.

A closely related technique used to characterize lateral non-uniformities in CIGS electronic properties is cathodoluminescence. This technique has been used to analyze high efficiency CIGS cells over a range of temperatures and injection levels[3.1.13]. It was found that at low temperatures, quasi-donor-to-acceptor transitions dominate the luminescence. The emission spectrum was found to vary from grain to grain and attributed to defect ordering. However, there was no attempt to quantify the observed lateral fluctuations in terms of performance losses.

Surface photo-voltage and electron beam induced voltage measurements have also been used to determine the lateral non-uniformities in electronic properties across CIGS solar cells. In one case, a scanning tunneling microscope combined with a laser was used to map the distirbution in photo-voltage across a CdS/CIGS sample[3.1.14]. In another case, the lateral non-uniformities in electron beam induced voltage was measured on CdS/CIGS samples using an SEM[3.1.15]. Both approaches found large changes in photo/electron beam induced voltage across the sample which were interpreted as variations in material properties that would affect the final device performance. However, a key problem with these is obtaining high resolutions if the full p-n junction is formed after CdS deposition. The lateral resolution obtained using these techniques is governed by the sheet resistance of the n-type layer as the Mo contact on the p-type CIGS side keeps the back surface at equipotential[3.1.21]. A 100nm layer of CdS would need more than $10^{16} cm^{-3}$ free carriers to form a complete p-n junction with the CIGS layer. The resulting sheet resistsance (assuming a mobility of 10 $cm^2 V^{-1} sec^{-1}$) of the CdS would result in screening lengths above 2μm[3.1.21]. The fact that scanning tunneling microscopy measurments of the surface photovoltage after CdS shows large lateral non-uniformities on the sub-micron length scale strongly suggests the CdS has insufficient doping to form the n-type part of the junction. This point will be

addressed in more detial in Sec. 3.6 where experimental evidence will be provided that the full p-n junction is not formed after CdS deposition. Ultimately, whether the junction is fully formed is extremely important for interpreting surface photovoltage or electron beam induced voltage measurements as they will be affected by electronic properties that are not expected to have much influence on the overall device performance such as the CdS free carrier concentraiton.

Two potentially very useful techniques for understanding lateral non-uniformities in electronic properties are EBIC and electroluminescence. As discussed in the previous section, EBIC can be used to measure the collection properties of the CIGS absorber layer. The experiments previously done used a defocused electron beam to provide average depth dependent measurements. However, the electron beam can be focused to a spot size of roughly 1nm enabling lateral non-uniformities in the carrier collection probability to be measured across the sample and quantified.

Electroluminescence (EL) imaging is a powerful tool for characterizing defects such as localized shunts and top electrode sheet resistance in solar cells[3.1.22,3.1.23]. EL images have been used to characterize thin film solar cells such as Cu(In,Ga)Se$_2$ (CIGS)[3.1.22] and CdTe[3.1.24]. However, EL imaging can also provide more fundamental information about the diode behavior of a cell due to the reciprocity between EL efficiency and solar cell performance[3.1.25]. This has already been expressed in analytic equations for silicon connecting the EL intensity with diffusion length[3.1.26]. However, thin film solar cells exhibit different diode behavior due to secondary barriers and the increased contribution of the diode current from the space charge region (SCR) relative to silicon, making it imperative to develop equations connecting EL intensity to material parameters in thin film solar cells.

The purpose of the following sections is to extend the theory of electron beam induced current and electroluminescence to thin film solar cells thereby making it possible to quantitatively characterize electron non-uniformities in solar cells and their effect on device performance. These techniques will then be applied to various CIGS solar cells grown at the National Renewable Energy Laboratory to provided quantitative information about the degree of electronic non-uniformity and how important the non-uniformities are for device performance. Furthermore, based on the results obtained from electroluminescence imaging, new insights will be developed into the junction formation process in CIGS solar cells.

3.2   Theory of Electroluminescence (EL) Intensity in Thin Film Solar Cells

As previously mentioned, thin film solar cells made of CIGS and CdTe can be approximately described as a n$^+$p heterojunction[3.2.1]. Due to the large valence band discontinuity at the buffer/absorber interface, the pn product under forward bias is significantly higher in the absorber. For this reason, the EL coming from other layers of the device is negligible and can be ignored. The EL intensity as a function of applied voltage can be expressed as[3.2.2]:

$$EL(V) \propto \int_{-W}^{d-W} C(x) n(x, V - V_{BL}) p(x, V - V_{BL}) dx \qquad (3.1)$$

where $C(x)$ is the probability of an electron hole pair recombining radiatively in the film and being collected by the external detector, d is the film thickness and V_{BL} is the voltage drop across any secondary diodes[3.2.3]. The influence of the secondary diodes on EL intensity will be discussed in more detail in Sec. 3.6. For now, we will assume the probability of radiative recombination is constant throughout the film. In this case, $C(x)$ can be taken out of the integral and set equal to a constant (C_0). The EL in a uniform bandgap semiconductor can be split into contributions from the quasi-neutral bulk and the SCR:

$$EL(V) \propto C_0(p_0 \int_0^{d-W} n(x)dx + Wn_i^2)\exp(q(V - V_{BL})/kT). \tag{3.2}$$

Assuming the injected carriers do not modify the original band diagram in the quasi-neutral bulk, the depth dependent electron concentration is given by[3.2.4]:

$$n(x) = n(0)\left[\frac{\cosh[(d-W-x)/L] + (SL/D_e)\sinh[(d-W-x)/L]}{\cosh[(d-W)/L] + (SL/D_e)\sinh[(d-W)/L]}\right] \tag{3.3}$$

Inserting equation 3.3 into equation 3.2 and integrating gives[3.2.5]:

$$EL(V) \propto C_0 n_i^2 (W + L\xi)\exp(q(V - V_{BL})/kT) \tag{3.4}$$

where ξ is given by:

$$\xi = \frac{\sinh[(d-W)/L] + (SL/D)(\cosh[(d-W)/L] - 1)}{\cosh[(d-W)/L] + (SL/D)\sinh[(d-W)/L]} \tag{3.5}$$

Eq. 3.4 shows the electroluminescence intensity is strongly affected by the bandgap, collection length $(W + L\xi)$ and applied voltage. Equation 3.4 is also valid for silicon solar cells although the dependence of EL intensity on space charge width is usually ignored, as it is much smaller than the bulk diffusion length[3.2.6].

It is important to note that Eqn. 3.4 contains no terms reflecting the defect concentration in the space charge region. This was confirmed by performing finite element simulations[3.2.7] on an asymmetric n+p heterojunction. The first case considered was a semiconductor with a constant defect concentration (N_t) of 2×10^{13} cm^{-3} and symmetric electron/hole capture cross sections equal to 5×10^{-13} cm^2. The second case assumes a 250nm layer at the front of the semiconductor where N_t is increased to 6×10^{13} cm^{-3}. The product of the electron and hole concentration and the recombination rate through the device are displayed in Fig. 3.4 at 400mV forward bias. Fig. 3.4 shows the defective layer increases the total recombination yet the integrated pn product (i.e. EL intensity) only drops by 12%. The small dependence of EL intensity on N_t in the space charge region comes from the quasi-Fermi level separation no longer being constant through the space charge region as is assumed in Eqn. 3.4. The increased recombination in the defective layer lowers the device open circuit voltage by roughly 30mV. By comparison, a 30mV drop in V_{oc} for a silicon solar cell would require an 80% change in bulk diffusion length thereby resulting in an 80% variation in EL intensity (Eqn. 1.34).
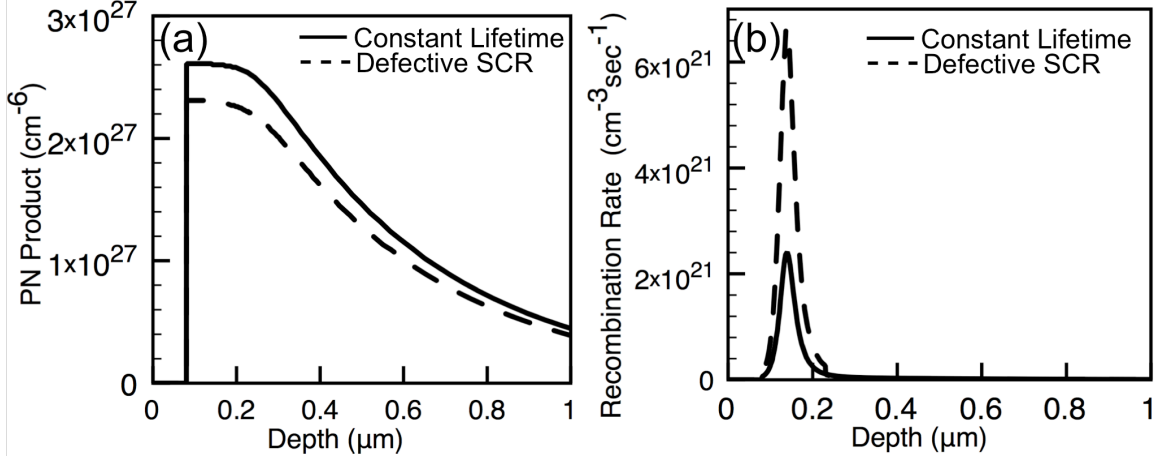
Fig. 3.4: (a) Product of the electron and hole concentration as a function of depth through the absorber. One case has a constant defect concentration and the other has a defect concentration three times higher in the space charge region. (b) Recombination rate as a function of depth for the two cases.

The dependence of the EL intensity on injection current can be expressed analytically assuming the forward current is controlled by recombination in the SCR through a midgap defect with equal capture cross sections for electrons and holes. In this case, the diode current is given by Eqn. 1.25. Inserting Eqn. 1.25 into Eqn. 3.4 gives:

$$EL(J) \propto \frac{4C\tau^2(W + L\xi)J^2}{q^2 W'^2} \tag{3.6}$$

Using Eqn. 1.25, the open circuit voltage of a device dominated by SCR recombination is roughly:

$$V_{oc} \approx \frac{kT}{q} \ln\left(\frac{4\tau^2 J_{sc}^2}{q^2 W'^2 n_i^2} \right) \tag{3.7}$$

where J_{sc} is the short circuit current of the device. It is apparent that both the V_{oc} and EL intensity at constant injection current strongly depend on the lifetime in the SCR. However, the intrinsic carrier concentration does not factor into the EL intensity at constant injection current, making it is possible to separate the effects of bandgap and recombination on forward current using EL measurements.

3.3   Extracting Shunt and Sheet Resistance from EL Images

One useful application of EL imaging comes from the voltage dependence of Eqn. 3.4 thereby making EL images sensitive to lateral variations in voltage across the TCO front contact. This can be used to measure the effect of both shunt resistance and sheet resistance on device performance. Furthermore, accurately accounting for the effects of shunt and sheet resistance is critical to avoid misinterpreting other lateral non-uniformities present in EL images.

Localized shunts can be particularly damaging to solar cell efficiencies by reducing the fill factor of a cell. Localized shunts will draw current from the cell

60

over a specified area given by the screening length of the TCO, which is typically on the order of a millimeter[3.3.1]. The high currents flowing through the shunt result in a potential gradient along the TCO. This causes a decrease in the applied voltage in the vicinity of the shunt[3.3.2]. As such, shunts appear in electroluminescence images as "dark" funnels.

An example of an electroluminescence image showing the effect of a localized shunt is given in Fig. 3.5. The image was taken with a Xenics Peltier cooled InGaAs camera. The sample was grown by vacuum co-evaporation at NREL with an un-optimized two-stage growth process where the selenium flux was intentionally kept low. Fig. 3.5 shows an EL image of the cell at 460mV forward bias (9.5mA/cm^2). EBIC imaging of the shunted area shows a feature roughly 20μm wide producing no current indicating the presence of a shunt.
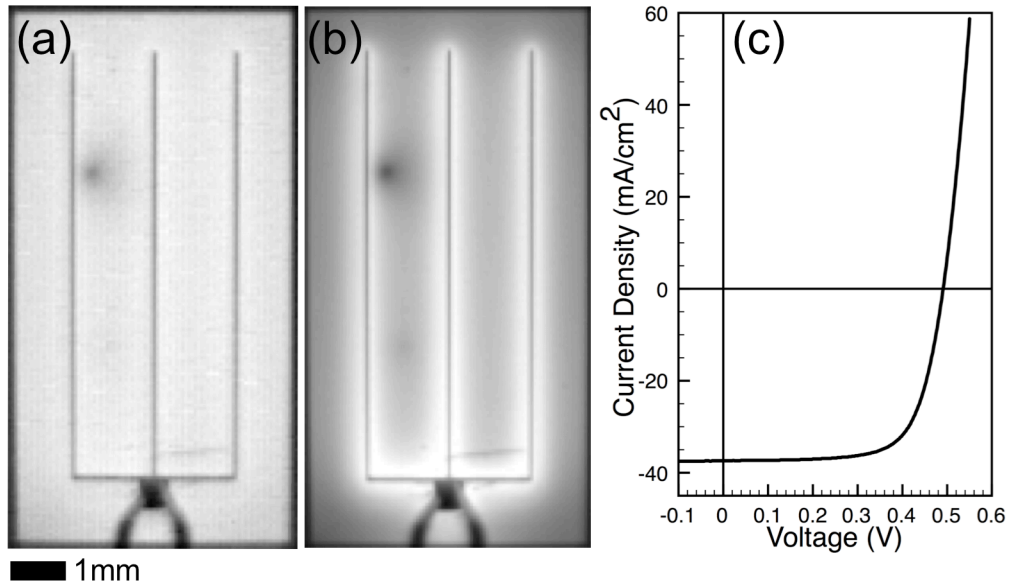

FIG. 3.5: (a) EL image at 460mV and (b) 560mV forward bias. (c) The I-V curve of the cell under 1-sun illumination.

Fig. 3.5 also shows the cell with a 560mV applied bias (64mA/cm^2). In addition to the EL contrast provided by the shunt, contrast is also observed around the cell fingers. This contrast is due to the large forward current flowing across the TCO and has been used to determine the local sheet resistance in silicon solar cells[3.3.3]. However, in the case of CIGS solar cells, the direct determination of the TCO sheet resistance is complicated by the additional stack resistance of the CdS/IZO layers which do not exist in silicon solar cells.

In order to quantitatively determine both the TCO resistance and the shunt resistance, it is necessary to use numerical simulations. NGSPICE[3.3.4] was used to model a 5mm x 1.3mm section of the cell using a grid of 100 x 26 nodes. Each node is represented by the equivalent circuit shown in Fig. 3.2. The simulation results were first compared to a line scan between two fingers away from the shunt to determine the TCO sheet resistance. The local shunt resistance was then determined by comparing the simulation results to a line scan through the shunt. The original image, simulated image and line scan comparison is shown in Fig. 3.6

along with the simulation parameters. In order to describe the large area affected by the shunt in Fig. 3.6, a shunt resistance of 500Ω had to be used. However, the slope of the I-V curve near zero bias in Fig. 3.5 suggests a linear shunt resistance of over 1500Ω. Therefore, the shunt in question may be non-linear. In this respect, EL imaging can be very helpful in determining the effect of shunts on cell performance as the image can be obtained near the maximum power point where the cell operates.
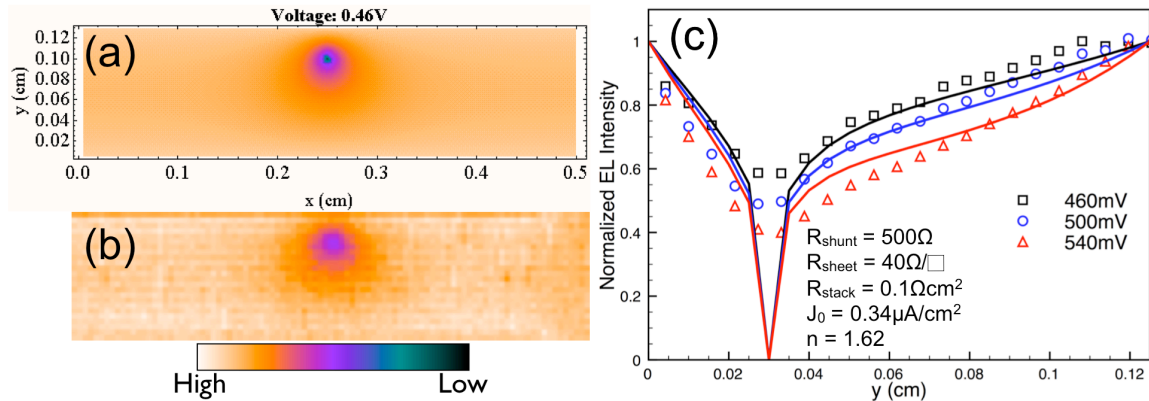

FIG. 3.6: (a) Simulated and (b) experimentally observed EL contrast around a localized shunt. (c) Experimental and simulated line scans through the localized shunt at various voltages.

3.4   Quantifying Lateral Variations in Bandgap and Collection Length

EL images will also show contrast due to variations in the diode properties across the cell. By taking images at low forward current and under UV illumination (the importance of using UV illumination will be discussed in Sec. 3.6), it is possible to minimize the voltage dependence of Eqn. 3.4 and directly view the variation in diode properties. This is shown in Fig. 3.7 on a 2µm thick $CuIn_{0.7}Ga_{0.3}Se_2$ solar cell taken at 640mV (5mA/cm²) forward bias. This sample was also grown at NREL by a two-stage vacuum co-evaporation process under high selenium flux. The image shows non-uniformities in EL intensity due to variations in either the local bandgap or collection length $(W + L\xi)$. As the EL intensity is proportional to both properties, additional techniques are needed to decouple the two effects.
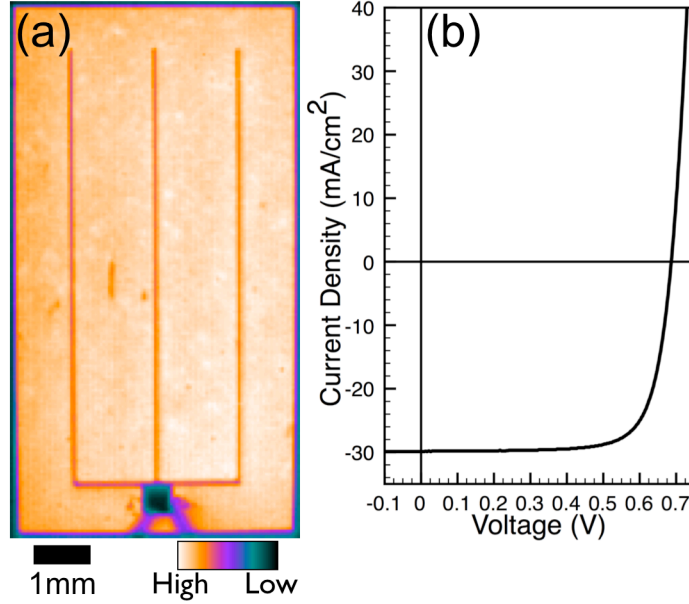
Fig. 3.7: (a) EL image at 640mV forward bias. (b) Corresponding I-V curve under 1-sun illumination.

For further analysis, a small section of the sample was imaged using infrared light beam induced current (IR-LBIC) and EBIC. The EL, IR-LBIC and EBIC images are shown together in Fig. 3.8. The IR-LBIC image was obtained by focusing an 1107-nm laser onto the sample mounted on a motorized stage. The quantum efficiency at long wavelengths is primarily affected by variations in the local absorption coefficient due to bandgap fluctuations as well as variations in the collection length. For this reason, the EL and IR-LBIC images shown in Fig. 3.8 are similar. EBIC images were obtained using ~200pA of beam current as measured using a faraday cup mounted on the sample holder. The EBIC images contain information about the collection length convoluted with the electron energy dissipation function as discussed below.

A qualitative comparison of the images in Fig. 3.8 indicates all three imaging techniques show similar features on a sub-millimeter length scale. Local bright and dark spots are observed using all three techniques suggesting a common origin. On the millimeter length scale, a gradient in intensity is observed from left to right on both the EL and IR-LBIC images but not on the EBIC image. This suggests the long range fluctuations have a different physical origin, which does not affect the electron beam induced current.
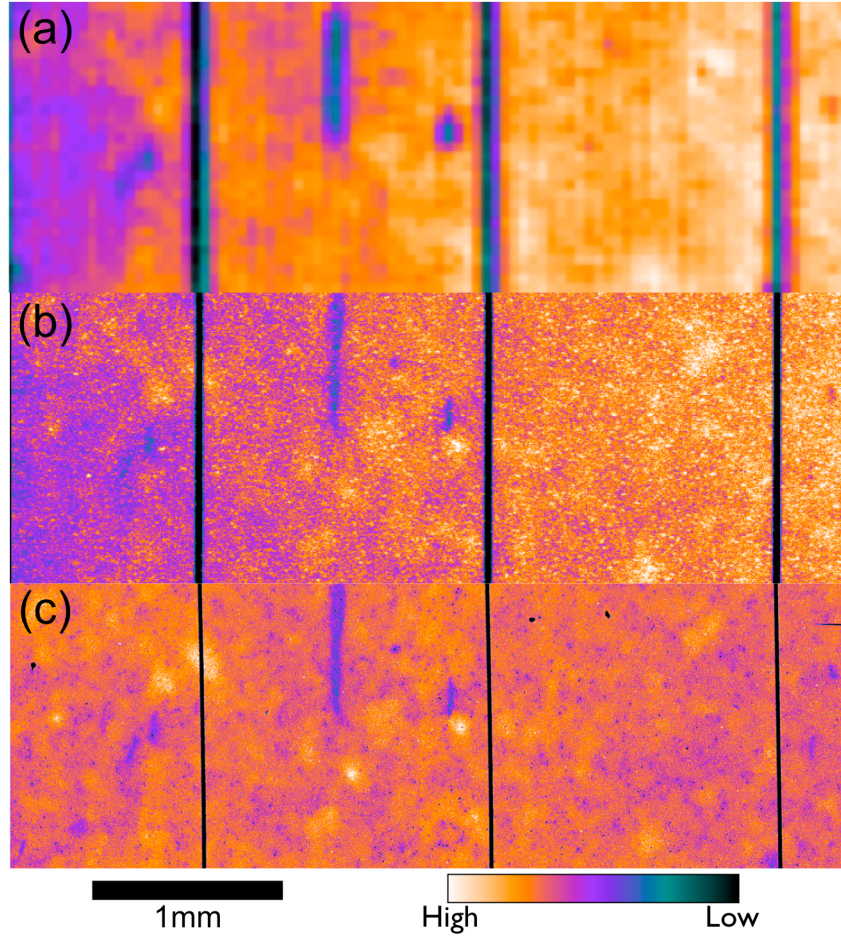
Fig. 3.8: (a) EL image taken at 640mV forward bias with enhanced contrast to highlight the non-uniformities. (b) IR-LBIC and (c) EBIC images taken in the same location.

The measured EBIC, as previously shown, can be described by Eqn. 2.1. If $g(V,z)$ were constant throughout the depth of the sample and there were no gallium gradients, the integral of Eq. 2.1 would be proportional to the collection length $(W + L\xi)$. This result is trivial given the reciprocity theorem connecting the excess minority carrier density and carrier collection[3.4.1]. However, an important distinction is the integrated excess minority carrier density depends on the local bandgap (Eq. 3.4). Therefore, if the electron-hole pair generation rate ($g(V,z)$) is approximately constant through the sample depth and only weakly dependent on the local bandgap, a direct comparison between EBIC and EL images would allow the separation of bandgap and the collection length $(W + L\xi)$ fluctuations. The strongest bandgap dependence in the function $g(V,z)$ comes from the energy required to create an electron hole pair (Eqn. 2.2). A 20meV variation in bandgap would lead to only a 1.5% change in EBIC but over a 50% change in EL intensity. Therefore, it is reasonable to assume lateral variations in bandgap do not affect the EBIC images.

As mentioned before, the electron beam induced current is proportional to the collection length of the sample if the energy dissipation function is constant through the sample. This can be approximately obtained by using high accelerating voltages, which leads to a broader, more constant generation rate. The electron-hole pair generation rate at 30kV is shown in Fig. 3.9. This figure shows that the electron-hole pair generation rate is not flat but peaks at around 0.7μm. Therefore, the electron beam induced current will also be somewhat sensitive to the shape of the collection function (Eq. 1.47) and not just the collection length $(W + L\xi)$.

To quantify this effect, the integral in Eq. 2.1 was numerically calculated for collection functions (Eq. 1.47) obtained using different values for the space charge width and bulk diffusion length. The space charge width in the CIGS absorber was varied from 0.2 to 0.7μm and the quasi-neutral bulk diffusion length from 0.25 to 2μm. Fig. 3.9 shows the calculated EBIC quantum efficiency in a 2μm thick CIGS sample at 30kV as a function of the collection length. The properties and thicknesses of the CdS and ZnO layers used in the simulation were the same as described in Sec. 2.4. Fig. 3.9 shows that the EBIC quantum efficiency is linear with respect to the collection length, even though the electron energy dissipation function is not constant through the depth of the sample. Therefore, EBIC images obtained at high accelerating voltages can be used to map non-uniformities in the collection length and compared directly to EL images.
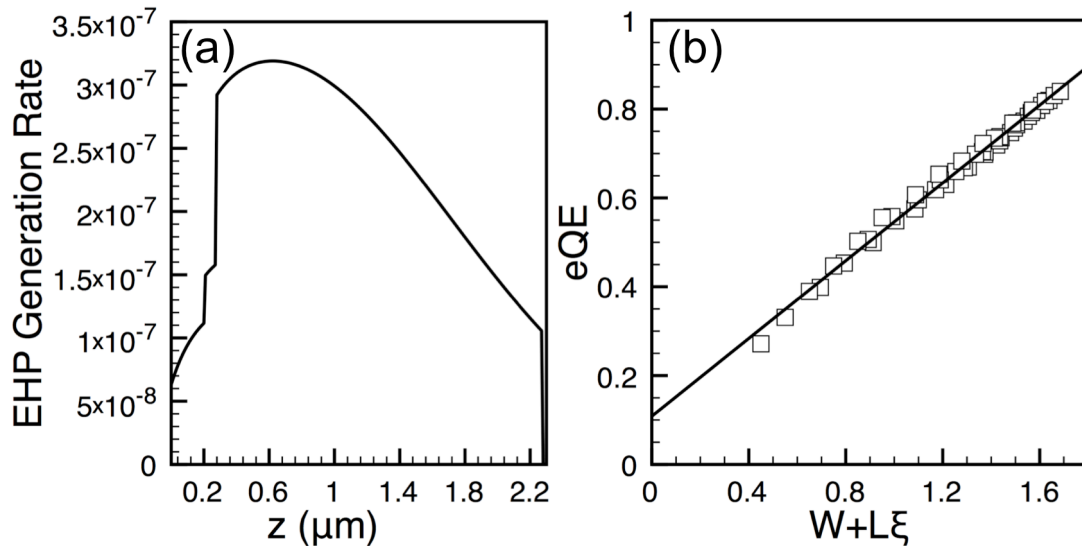

Fig. 3.9: (a) Electron-hole pair (EHP) generation rate as a function of depth through the sample at 30kV. (b) Expected EBIC quantum efficiency at 30kV versus the collection length assuming a range of possible space charge widths and bulk diffusion lengths. The straight line fit shows the EBIC quantum efficiency is linearly proportional to the collection length.

In order to obtain quantitative values of the collection length at each point on an EBIC image, it is necessary to first determine the average collection efficiency $(F(z))$ through the depth of the sample. This can be obtained using the EBIC technique described in Sec. 2. The relationship between the collection length and EBIC quantum efficiency shown in Fig. 3.9 can then be used to convert an EBIC image into a map of the collection length across the sample. The average EBIC

quantum efficiency and fit are shown in Fig. 3.10. The fit was obtained by assuming a space charge width of 500nm, neutral bulk diffusion length of 0.92μm and (S/D) ratio of 3800cm^{-1} resulting in a collection length of 1.29μm.
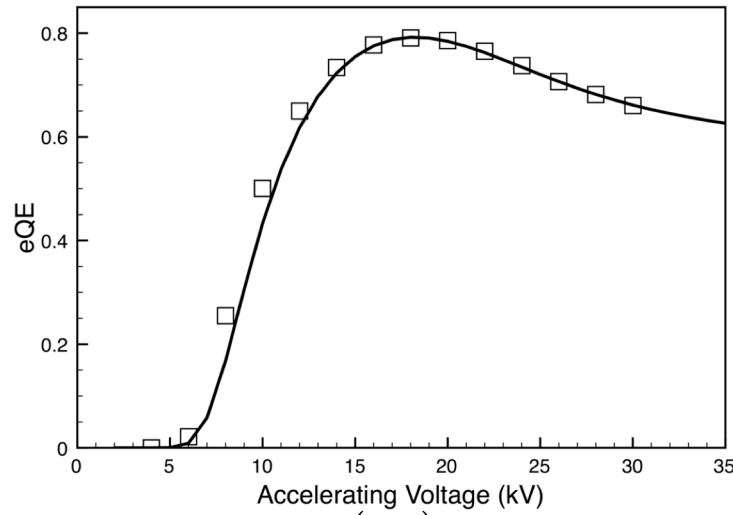

Fig. 3.10: Average EBIC quantum efficiency (eQE) versus accelerating voltage taken by defocusing the electron beam. The solid line shows the fit to the data.

A histogram of the collection length is shown in Fig. 3.11 along with the regions of the cell where the collection length varies by more than two standard deviations (0.05μm) from the average. It is apparent in Fig. 3.11 that variations in the collection length appear across the sample on a length scale above 100μm. Variations in the collection length on a smaller length scale (~1μm) are also observed in Figure 3.12. It should be noted that these images are taken at high accelerating voltage, which limits the lateral resolution to around 2μm due to the shape of the electron energy dissipation function as discussed in Sec. 2.2. Variations in the collection length on this length scale were also observed in CIGS samples in Sec. 2.6 and by other research groups using cross sectional EBIC[3.4.2].
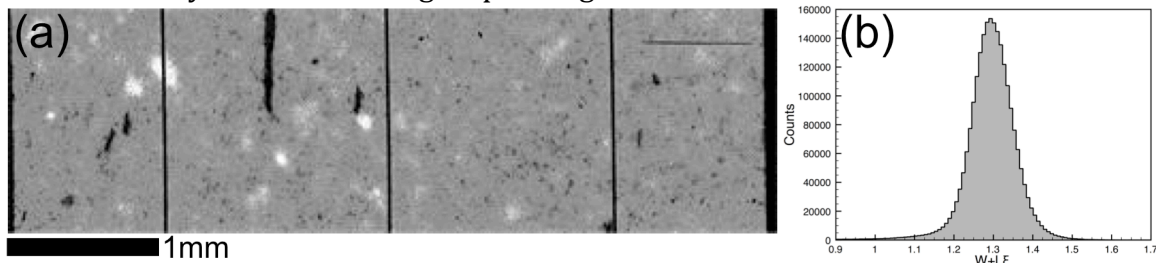

Fig. 3.11: (a) Map of the collection length across the sample as determined by EBIC. The white (black) areas correspond to areas with a collection length 0.1μm higher (lower) than the mean. (b) Histogram of the collection lengths observed on the sample.
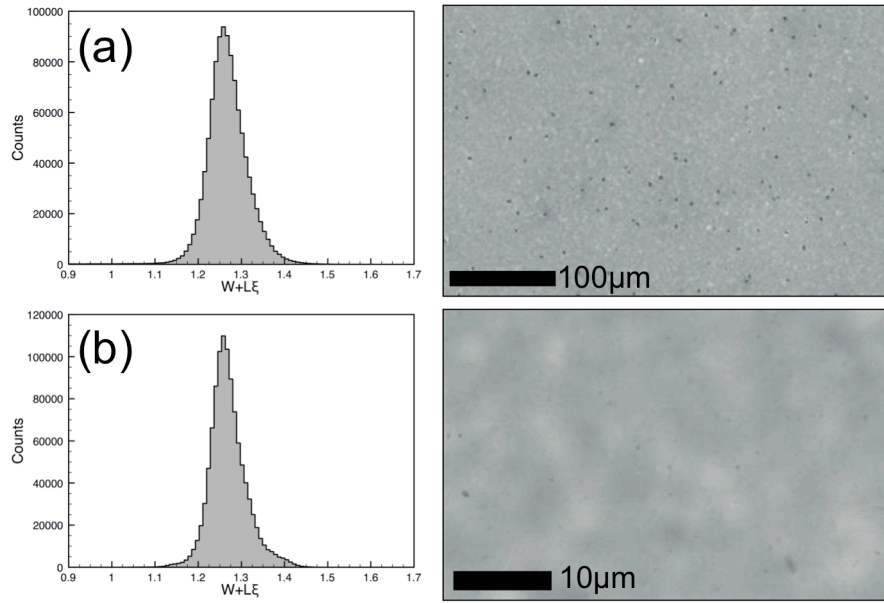
Fig. 3.12: (a) Histogram and EBIC image of the sample taken at medium and (b) high resolution.

By using a map of the collection length, it is possible to modify the EL image to display only bandgap variations by dividing the EL image by the collection length at each point. The resulting image of bandgap fluctuations is shown in Fig. 3.13. The most notable difference between the bandgap map and original EL image is the enhanced contrast on the length scale of 1mm. This is explicitly shown in Fig. 3.13 where the average bandgap is plotted laterally across the cell. From this figure, the variation in bandgap across the sample is less than ~5meV. Furthermore, it is apparent that some areas of high bandgap coincide with low collection efficiency.
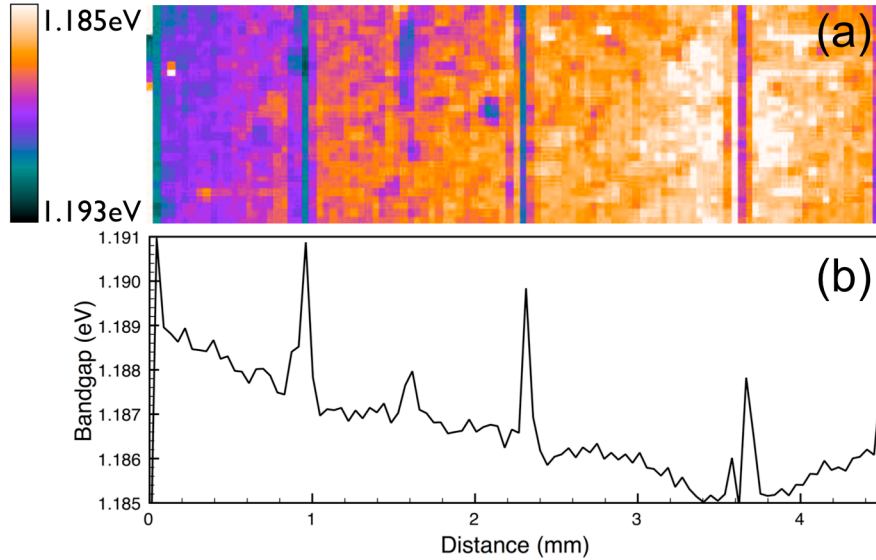

Fig. 3.13: (a) Bandgap map across the sample as determined by the EL and EBIC images. (b) Average bandgap across the width of the sample.

Additional complications may occur when comparing EL and EBIC images for samples with a non-uniform bandgap through the depth of the absorber. For example, if sample had a linearly increasing bandgap the minority electron density throughout the bulk would be [3.4.3]:

$$n(z) = n(0)\exp(-\xi z/2)\frac{\cosh[(d-W-z)/L'] + (S'L'/D_n)\sinh[(d-W-z)/L']}{\cosh[(d-W)/L'] + (S'L'/D_n)\sinh[(d-W)/L']}. \qquad (3.8)$$

For comparison, the collection efficiency throughout the cell is given by Eqn. 1.47. Comparing Eq. 3.8 and Eq. 1.47, the normalized electric field has the opposite effect on the minority carrier density compared to the collection efficiency. Therefore, the electric field will increase the collection efficiency but decrease the EL intensity. This effect will be further compounded by reabsorption of the electroluminescence emitted from the high gallium region. While it is possible to correct for this, it's necessary to accurately know the absorption coefficient through the cell thickness.

By combining EBIC and EL imaging, it is possible to obtain a map of the bandgap and collection length fluctuations across a sample. From this information, the effect of these fluctuations on cell performance can be quantified. The most important effect of bandgap fluctuations is on the saturation current density of the cell as this dictates the open circuit voltage (V_{oc}).

To calculate the effect of bandgap fluctuations on device performance and the measured EL intensity, it is necessary to assume some distribution of bandgaps. The simplest approximation is that the bandgaps follow a gaussian distribution[3.4.4,3.4.5]. Following the work in Ref 3.4.5, the V_{oc} of a device where recombination is predominantly in the SCR through a midgap defect with equal capture cross sections for electrons and holes can be expressed as:

$$V_{oc} \approx \frac{\overline{E}_g}{q} - \frac{\sigma_{Eg}^2}{4qkT} - \frac{2kT}{q}\ln\left(\frac{qW'\sqrt{N_cN_v}}{J_{sc}2\tau}\right) \qquad (3.9)$$

where $\overline{E}_g$ is the average bandgap and σ_{Eg} is the standard deviation of bandgaps,.

The same approach can be used to describe the EL intensity on a sample with bandgap fluctuations[3.4.6]:

$$EL(V) = C_0N_cN_v(W+L\xi)\exp(qV/kT)\int_{-\infty}^{\infty}\frac{1}{\sqrt{2\pi\sigma_{Eg}^2}}\exp\left(-\frac{(E-\overline{E}_g)^2}{2\sigma_{Eg}^2}\right)\exp(-E/kT)dE. \qquad (3.10)$$

Integrating Eqn. 3.10 gives:

$$EL(V) = C_0N_cN_v(W+L\xi)\exp\left(-\frac{\overline{E}_g}{kT} + \frac{\sigma_{Eg}^2}{2k^2T^2}\right)\exp(qV/kT). \qquad (3.11)$$

Eqn. 3.11 shows the overall EL intensity of a cell is increased by bandgap fluctuations. However, more information can be obtained from the distribution of EL intensities measured on a sample. Assuming the collection length does not strongly vary across the cell, the standard deviation of EL intensities is:

$$\sigma_{EL}(V) = \sqrt{\int_{-\infty}^{\infty}\left(A(V)\exp\left(\frac{-E}{kT}\right) - A(V)\exp\left(-\frac{\overline{E}_g}{kT} + \frac{\sigma_{Eg}^2}{2k^2T^2}\right)\right)^2 \frac{1}{\sqrt{2\pi\sigma_{Eg}^2}}\exp\left(-\frac{(E-\overline{E}_g)^2}{2\sigma_{Eg}^2}\right)dE} \qquad (3.12)$$

where $A(V) = C_0 N_c N_v (W + L\xi)\exp(qV/kT)$. The integral of Eqn. 3.12 is:

$$\sigma_{EL}(V) = C_0 N_c N_v (W + L\xi)\exp\left(-\frac{\overline{E}_g}{kT} + \frac{\sigma_{Eg}{}^2}{2k^2 T^2}\right)\exp(qV/kT)\sqrt{\left(\exp\left(\frac{\sigma_{Eg}{}^2}{k^2 T^2}\right) - 1\right)}. \quad (3.13)$$

Eqn. 3.11 and Eqn. 3.13 differ by a factor of $\sqrt{\left(\exp\left(\sigma_{Eg}{}^2/k^2 T^2\right) - 1\right)}$; therefore, it is possible to determine the standard deviation of bandgaps by looking at the distribution of EL intensities within an image. It is important to note that this derivation assumes the primary contrast on the cell is due to bandgap fluctuations as opposed to fluctuations in the collection length or series/shunt resistance effects. Also of note, the standard deviation of EL intensities will change depending on the resolution at which the EL image is obtained. If the bandgap fluctuations occur on a length scale lower than the resolution of the EL image, they will affect the calculated average bandgap.

One additional factor when determining the magnitude of bandgap fluctuations is the influence of stack resistance on the measured EL intensity. As previously mentioned, the stack resistance of a cell is primarily determined by the CdS/IZO layers which helps to limit the amount of current that can flow through weak diodes on a cell. Low bandgap areas on a cell function as weak diodes and therefore their impact on the device open circuit voltage is influenced by the stack resistance[3.4.5]. The stack resistance will influence the EL intensity in a similar way, as weak diodes will draw more current thereby causing a larger voltage drop across the CdS/IZO layers and increasing V_{BL} in Eq. 3.4.

Numerical simulations were used to examine the influence of stack resistance on the bandgap distribution calculated using Eq. 3.11 and Eq. 3.13. NGSPICE[3.4.7] was used to simulate the device open circuit voltage and EL intensity distribution from a Gaussian distribution of bandgaps using a network of 2000 nodes with the equivalent circuit shown in Fig. 3.2. The stack resistance was set at 0, 0.02 and 0.1Ωcm^2 while the standard deviation of bandgaps was varied from 0 to 40meV. R_{shunt} (R_{sheet}) was assumed to be infinite (zero). All diode parameters not related to the bandgap were held constant. The resulting distribution of EL intensities was calculated using Eq. 3.4 at each node. The standard deviation of bandgaps was then calculated from the distribution of EL intensities using Eq. 3.11 and Eq. 3.12 and is shown in Fig. 3.14. Fig. 3.4 shows the calculated V_{oc} versus the V_{oc} obtained in the NGSPICE simulation. The correlation between the simulated V_{oc} and the V_{oc} calculated from the EL distribution is very good even as the stack resistance changes. This analysis shows that Eq. 3.11 and Eq. 3.13 can still be used to estimate efficiency losses even in the more practical case when R_{stack} in the device is not zero. This approach is valid as the stack resistance affects the distribution of EL intensities in a similar way that it limits the V_{oc} loss from weak diodes and therefore the distribution of EL intensities will directly determine the V_{oc} loss from bandgap non-uniformities. This result also shows the advantage of using EL to determine efficiency losses from bandgap non-uniformities as it automatically takes into account the protection provided by the stack resistance.
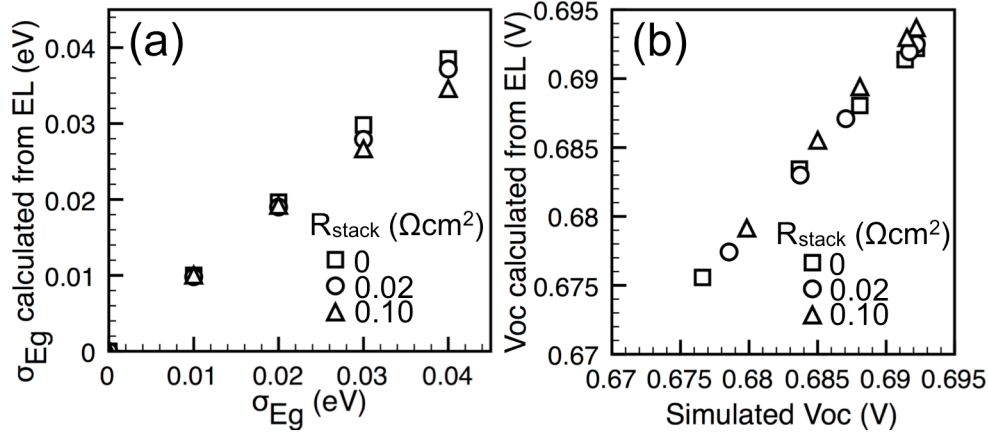
Fig. 3.14: (a) Standard deviation of bandgaps (σ_{Eg}) calculated from the simulated EL distributions versus the actual standard deviation of bandgaps used to generate the simulation data. (b) Simulated V_{oc} versus the V_{oc} calculated using Eqn. 3.9 and the data shown in (a).

While it is relatively straightforward to translate non-uniformities observed in EL intensity into their effect on device performance, the same cannot be said for variations in the collection length as determined by EBIC. The collection length is determined by the space charge width, bulk diffusion length and back surface recombination velocity. Higher space charge widths and bulk diffusion lengths both lead to an increase in carrier collection, but have opposite effects on the device open circuit voltage. As such, it's not possible to translate the variations observed in the collection length to an open circuit voltage loss. However, it is possible to translate such fluctuations into short circuit current losses. For the sample in Fig. 3.11, the expected loss in short circuit current is less than 0.5 mA as estimated from published values for the absorption coefficient[3.4.8].

3.5   Impact of Non-uniformities on Device Behavior

The role electronic non-uniformities on device behavior is still an open question for CIGS solar cells. Due to the polycrystalline nature of the CIGS absorber layer, it is highly unlikely that all the grains exhibit the same electronic properties. This is particularly important given the results shown in Sec. 2.5 where it was found that the average bulk diffusion length does not correlate with device open circuit voltage. There are several possible explanations for this result but the two most straightforward are a) the average bulk diffusion length is identical for all samples but the degree of electron non-uniformities (i.e. bandgap, bulk diffusion length, etc.) vary between the samples or b) the defect density in the space charge region is significantly different than in the quasi-neutral bulk.

The second hypothesis, that the defect density or defects controlling recombination in the space charge region is significantly different than in the quasi-neutral bulk, is inherently challenging to study due to the lack of characterization techniques which can probe this region. The most potentially appealing techniques for this study would be based on the sample capacitance (such as admittance spectroscopy or deep level transient spectroscopy). However, as discussed in Sec.

1.4, many previous studies have been done on CIGS using these techniques and there is still no consensus over which defects control recombination. On the other hand, the hypothesis that electronic non-uniformities are primarily responsible for device performance can be probed based on the EL and EBIC techniques discussed in the previous sections. These techniques are particularly advantageous for this study because they can study the entire sample area allowing a quantitative comparison between the electronic non-uniformities in each sample.

The bandgap non-uniformities on a sample could have a strong influence on device performance. These non-uniformities could happen on several length scales either due to defects during the manufacturing process or more fundamental processes such as the segregation of indium and gallium within the CIGS layer. To study this effect, the EL intensity at constant voltage was used to the bandgap non-uniformities using the same samples studied in Sec. 2.5. Eqn. 3.11 shows that at constant voltage, the EL intensity will be proportional to the bandgap distribution across the cell. It's important to note that this equation covers all possible length scales of the bandgap non-uniformities and directly measures the impact such non-uniformities would have on the device open circuit voltage (Eqn. 3.9).

The EL intensity at constant voltage is shown in Fig. 3.15 for samples with open circuit voltages varying by over 80mV. It is apparent from this figure that the samples from the two different plates have roughly constant EL intensities at constant voltage indicating a different average bandgap for the two plates. Furthermore, no relationship between EL intensity and open circuit voltage is observed between the samples. If the differences in open circuit voltage between devices were due to bandgap non-uniformities, one would expect the highest EL intensities would correlate with the lowest open circuit voltages. This would occur because areas of low bandgap on the sample appear brighter at a given voltage (Eqn. 3.4). The results in Fig. 3.15 in fact show the opposite behavior where the highest EL intensity samples also have the highest open circuit voltages strongly suggesting that bandgap non-uniformities are not responsible for variations in device performance.
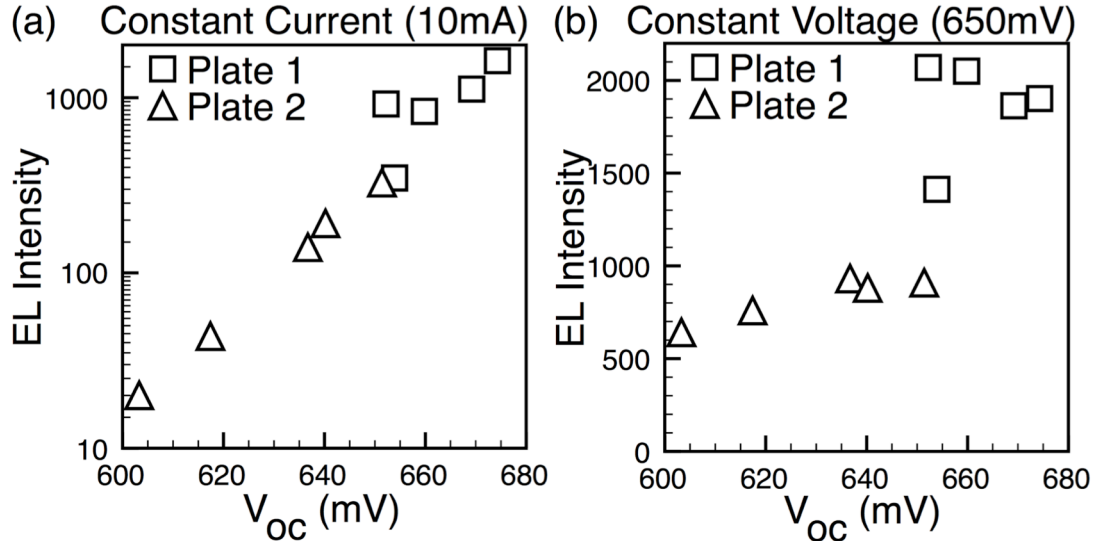
Fig. 3.15: (a) Electroluminescence intensity as a function of device open circuit voltage at constant current and (b) constant voltage for graded CIGS solar cells.

Measuring the samples at constant current also arrives at the same conclusion. Eqn. 3.6 shows that at a given current, the EL intensity is proportional to the lifetime in the absorber and has no relationship to the CIGS bandgap. The EL intensity at constant current versus device open circuit voltage is shown in Fig. 3.15 and shows a very strong relationship between the two indicating a variation in defect concentration from sample to sample is driving device performance.

Now that it is established that bandgap non-uniformities are not responsible for the variation in device performance, it is important to look at the variation in bulk diffusion length across the samples. The same technique described in Sec. 3.4 was used to map the variation in collection length across three samples with widely varying open circuit voltages. A histogram of the observed collection lengths and representative EBIC image are shown in Fig. 3.16. The EBIC image shows that lateral non-uniformities in the collection length are observed on several length scales. However, when comparing the histogram of collection lengths between samples, there is almost no difference in the degree of lateral non-uniformities. While the histogram of collection lengths is not necessarily the same as the variation in bulk diffusion length, they should be closely related and one would expect a very wide distribution of collection lengths in sample A (lowest Voc sample) if lateral non-uniformities in the bulk diffusion length were driving device performance.
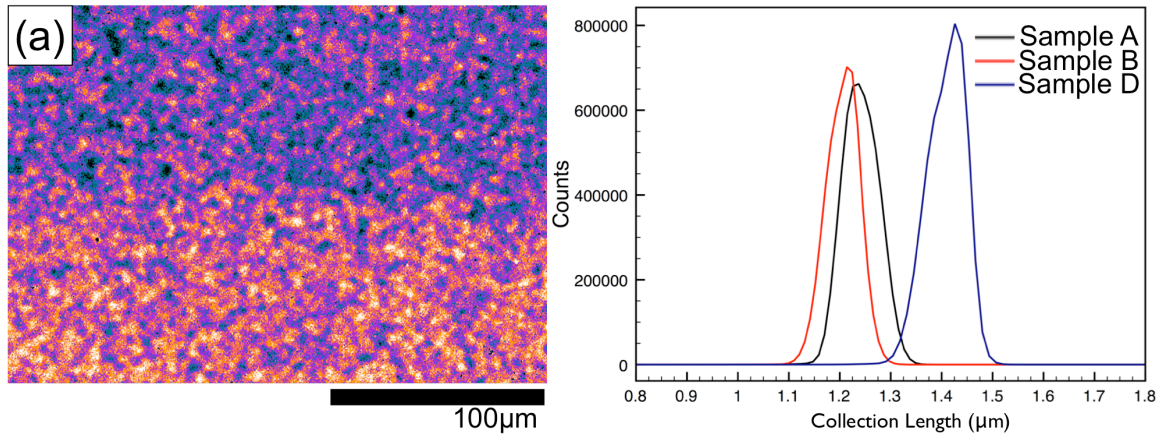
Fig. 3.16: (a) Representative EBIC image of a high efficiency CIGS solar cell. Both macro (~100μm) and micro (~5μm) non-uniformities in current collection are observed. (b) Comparison of the lateral non-uniformities in current collection for three high efficiency CIGS solar cells with large differences in open circuit voltage. The non-uniformities in current collection are quantitatively similar between all three samples suggesting lateral non-uniformities are not driving device performance.

Overall, no evidence was found using either EBIC or EL techniques that lateral non-uniformities in either the bandgap or bulk diffusion length drive the variation in device performance. Therefore, the most straightforward explanation for the variation in performance from sample to sample is a change in defect concentration in the space charge region.

In order to gain a more complete understanding of the recombination physics in CIGS solar cells, it is essentially to develop new techniques that can explore this region of the device. This may be difficult if the increased defect concentration in the space charge region is a fundamental consequence of the Fermi-level moving towards the conduction band at the front of the device. If this were true, the measured defect concentrations would be very contingent on the degree of band bending in the CIGS. As will be discussed in the next section, there is evidence that the Fermi-level is unpinned at the CdS/CIGS interface meaning that the built-in voltage after CdS deposition may be significantly less than after AZO deposition. This would mean that defect concentration measurements would need to be done on a full device or at least under conditions where the Fermi-level is brought close to the conduction band in the CIGS. However, many defect concentration measurements (such as time resolved photoluminescence) rely on measuring the properties of excess carriers generated in the CIGS layer. Moving the Fermi-level in the CIGS close to the conduction band also generates a built-in electric field that will quickly separate photo-generated carriers. This observation has already been made for time resolved photoluminescence measurements where it was found that charge separation kinetics dominate the signal if the measurement is performed on a full device[3.5.1].

3.6   Secondary Diode Effects

Despite being the highest efficiency thin film solar cell material, CIGS exhibits a wide range of unusual phenomena typically associated with highly defective materials. For instance, it has been observed that CIGS solar cells often exhibit evidence of a secondary diode in series with the primary diode, particularly at low temperatures[3.6.1]. This effect was initially prescribed to a rectifying back contact between the CIGS and Mo[3.6.1]. However, it has also been observed that the secondary diode effects are light sensitive suggesting the effect originates in the front of the device[3.6.2]. This effect is not well explained using the most basic equivalent circuit of a solar cell where the primary diode is in parallel with a current source. In this case, the difference between light and dark I-V curves is expected to be constant at all voltages as shown in Fig. 3.17.
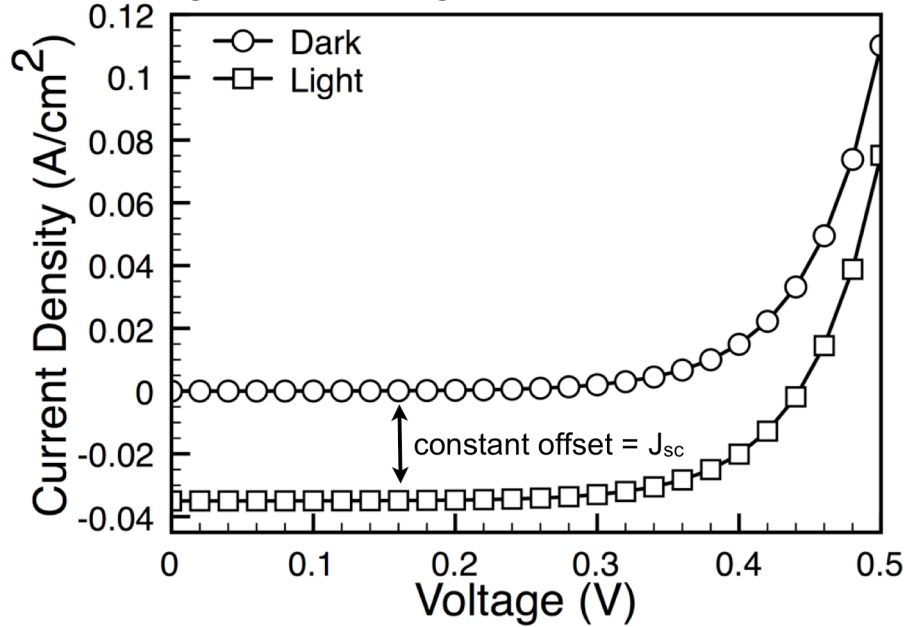

Fig. 3.17: Expected dark and light I-V curves for a solar cell based on a simple equivalent circuit where the primary diode is in parallel with a current source (J_{sc}).

This phenomenon is particularly important in the case of EL imaging where the sample is typically kept in the dark to avoid the influence of stray light on the captured image. If insufficient light reaches the solar cell during the measurement, the I-V characteristics can be drastically altered from the I-V characteristics in the sunlight. An example of this is shown in Fig. 3.18 where a $CuIn_{0.1}Ga_{0.9}Se_2$ solar cell was measured under 1-sun conditions in a solar simulator and then, several weeks later, measured in a dark box used to acquire EL images. Fig. 3.18 shows that the dark and light I-V curves do not differ by a constant value at all voltages. Furthermore, the curves cross each other at roughly 0.55V indicating the presence of a large secondary barrier in series with the primary diode. This effect is known as the failure of superposition between dark and light I-V curves.
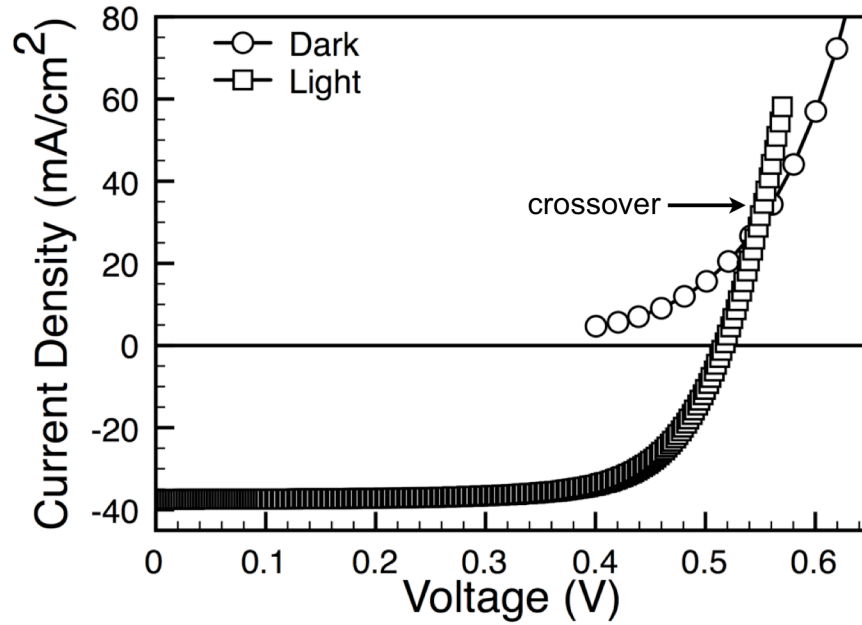
Fig. 3.18: Light I-V curve for a $CuIn_{0.1}Ga_{0.9}Se_2$ sample measured using a solar simulator and the dark I-V curve for the same sample measured in a dark box used for EL measurements. The light and dark I-V curves crossover in at roughly 0.55V.

Several theories have been put forth in literature to explain this effect. One theory attributes the effect to the conduction band offset between CIGS and CdS combined with photoconductivity in CdS. Theoretical calculations have put the conduction band offset between CdS and CIS at roughly +0.3eV indicating type-I band alignment[3.6.3]. Other experimental investigations of the barrier height between CdS and CIS have come to a similar value[3.6.4]. This offset provides a barrier to current injection equal to the difference between the Fermi-level at the CdS/CIGS interface and the bottom of the CdS conduction band. At first glance, the conduction band offset between CIS and CdS would seem to preclude the formation of high efficiency solar cells as this secondary barrier would provide a severe impediment to the collection of photogenerated electrons. However, numerical calculations have shown that barriers heights below 0.4 eV should have only a small effect on device performance[3.6.5].
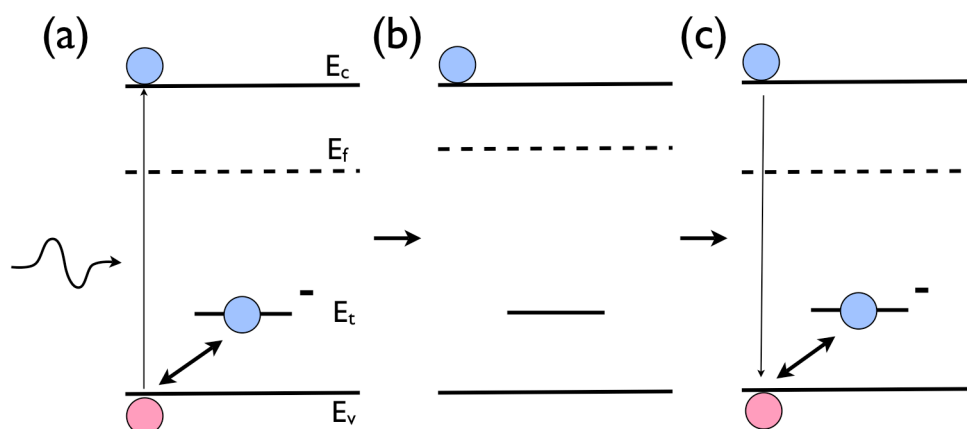
Fig. 3.19: (a) n-type CdS with a large concentration of deep acceptors (E_t). In the dark, the acceptors will be ionized and thus have a negative charge. Upon illumination, electron-hole pairs are generated. The photogenerated holes have a higher probability of being captured by the deep acceptor due to the coloumbic attraction. The steady-state condition under illumination is shown in (b) where there exists a surplus of electrons in the conduction band. When the illumination source is removed (c), the holes eventually are thermally emitted from the deep trap where they recombine with the excess carriers in the conduction band and restore the dark equilibrium condition.

Given the conduction band offset between the CdS and CIS, the variable determining whether this secondary barrier will or will not affect the device performance is the Fermi level at the CdS/CIS interface. The Fermi-level at this interface is a function of the free carrier density of the ZnO, CdS and CIS layers as well as the density of interface states between each layer[3.6.6]. Therefore, the change in carrier concentration in any of the layers would be expected to change the position of the Fermi-level at the CdS/CIS interface. It has been observed that the conductivity of CBD grown CdS films can change by orders of magnitude under illumination[3.6.7]. The photoconductivity in CdS has been explained by the presence of deep acceptors, which are ionized in the dark [3.6.8,3.6.9]. If the deep acceptors have a much larger capture cross section for holes than for electrons, they will effectively trap holes upon illumination leaving excess free electrons in the CdS conduction band. This process is shown schematically in Fig. 3.19. Some authors have attributed this effect in CdS to copper impurities[3.6.10].

Therefore, it has been proposed that the failure of superposition between dark and light I-V curves stems from the increase in carrier concentration of CdS under illumination[3.6.8,3.6.9]. This increase in carrier concentration in the CdS layer leads to additional band bending in the CIGS and pulls the bottom of the CdS conduction band closer to the Fermi level at the CIGS/CdS interface. Following the work of Ref. 3.6.8, this effect was simulated using AMPS[3.6.11]. The layer properties used in the simulation are based on those presented in Ref. 3.6.8 and Ref. 3.6.11. There is a large degree of uncertainty in each parameter and therefore they should only be considered as one possible way of obtaining this effect. To highlight the effect of photoconductivity on blocking behavior, Fig. 3.20 shows the band diagram of a ZnO/CdS/CIGS device under a 0.4V forward bias both in the dark and with a

380nm (UV) light source. Fig. 3.20 shows that in the dark, a significant fraction of the applied voltage (V_{BL}) drops at the CdS/CIGS interface due to the large energy difference between the electron quasi-Fermi level and the bottom of the CdS conduction band. Based on Eqn. 3.4 this would lead to a significant reduction in the EL intensity at a given bias. Under UV illumination, almost all of the applied voltage drops across CIGS layer thereby eliminating the effect of V_{bl} in Eqn. 3.4.
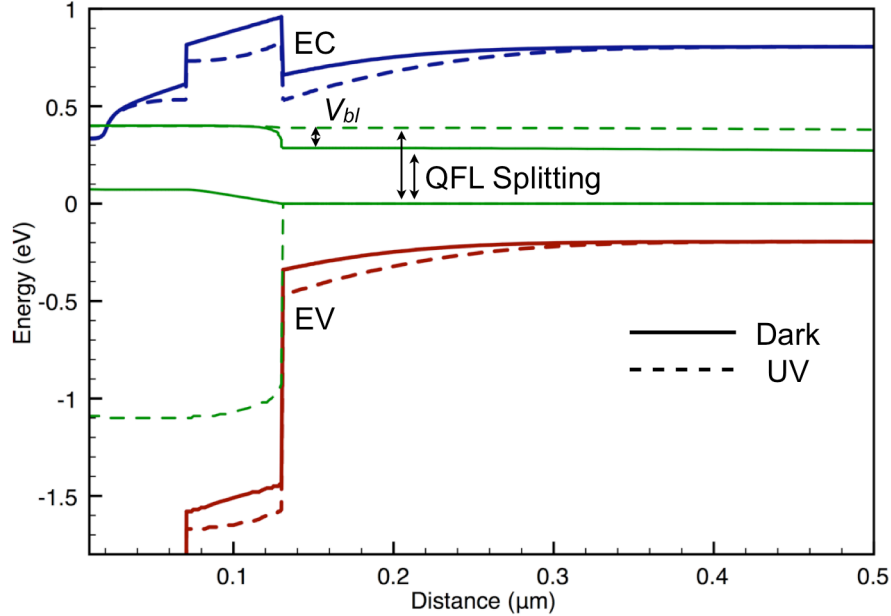

Fig. 3.20: Simulated band diagram of an AZO/IZO/CdS/CIGS structure under 0.4V forward bias in the dark and with UV illumination. The conduction band (EC), valence band (EV) and quasi-Fermi level (QFL) splitting are displayed. The barrier at the CdS/CIGS interface causes a reduction of the QFL splitting by V_{BL} in the dark.

An alternative theory has been proposed to explain the failure of superposition between dark and light I-V curves. This theory was developed in part to explain another interesting feature often observed on CIGS solar cells. Photo-emission experiments in CIS thin film samples have shown evidence for a thin Cu-poor compound on the surface of CIGS that appears to be n-type[3.6.12]. The Cu-poor compound has been described as the ordered defect compound (ODC) $CuIn_3Se_5$[3.6.13] which has a bandgap of roughly 1.6eV[3.6.14]. Hall effect measurements on thin films of $CuIn_3Se_5$ have also found the material to be weakly n-type[3.6.15]. This experimental evidence has led some groups to the conclusion that the Fermi-level is pinned at the CdS-CIGS interface[3.6.16]. As such, it is argued that the p-n junction is actually a "buried" junction in that it exists entirely within the CIGS layer.

The CdS/CIGS interface photoconductivity theory inherently requires that the Fermi-level not be pinned at this interface. Therefore, an alternative explanation has been presented explaining the failure of superposition between dark and light I-V curves, relying instead on a barrier due to deep acceptors between the ODC and bulk CIGS layer[3.6.17]. The exact details of this theory are beyond the scope of this section but an important distinction between this theory and the previous one is that photogenerated holes in the ODC should reduce the blocking barrier[3.6.17].

A simple example of the influence of photo-conductive blocking barriers on EL imaging is shown in Fig. 3.21. Here, two images are taken on a $CuIn_{0.9}Ga_{0.1}Se_2$ solar cell at 0.48V forward bias. One image was taken while the sample was in the dark while the other image was taken with additional UV illumination. A close examination of the two images shows the additional UV illumination results in the EL image being brighter due to a reduction of V_{BL} (Eqn. 3.4). The effect can be seen even more clearly in Fig. 3.22 where the injection current and average EL intensity are plotted versus the applied voltage. In this case, both the EL intensity and current versus voltage are affected in a similar way by the blocking barrier. This is also seen in Fig. 3.22 where the injection current is plotted versus EL intensity. Here it is apparent that the addition of the UV light is only modifying the term V_{BL} in Eqn. 3.4, which does not appear in the equation for EL intensity as a function of current injection (Eqn. 3.6).
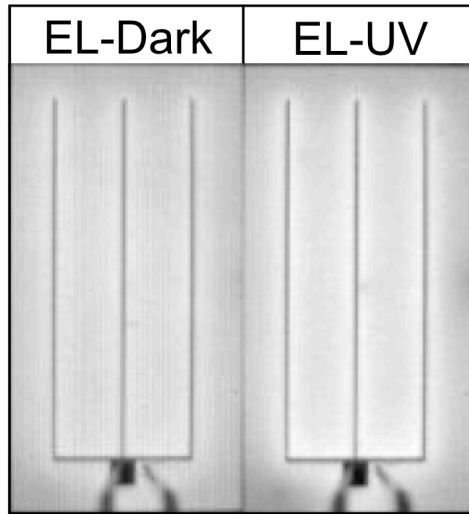

Fig. 3.21: EL images of a $CuIn_{0.1}Ga_{0.9}Se_2$ solar cell at 0.48V forward bias in the dark and under UV illumination. The EL image under UV illumination is slightly brighter than in the dark.
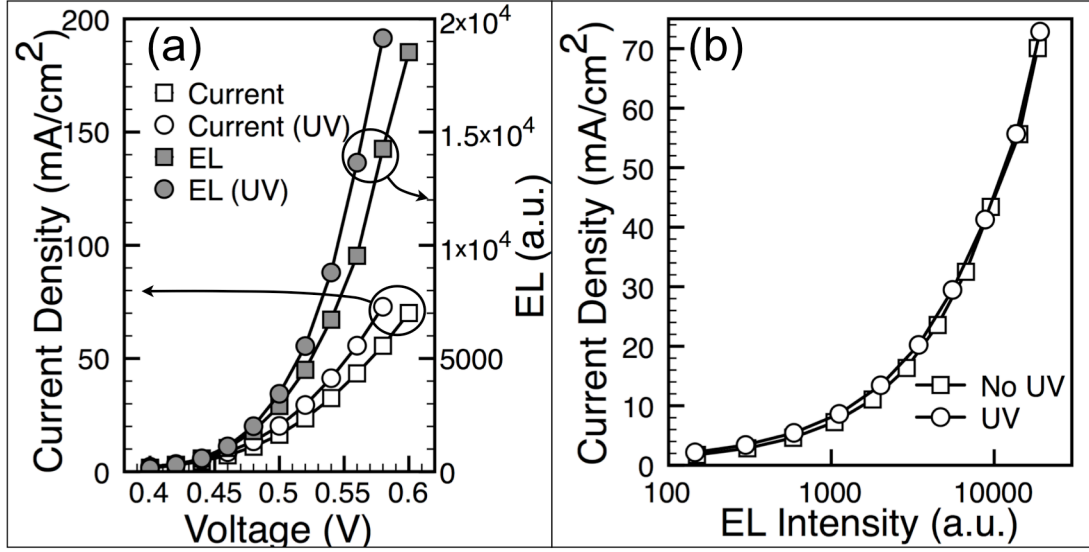
Fig. 3.22: (a) Current density and EL intensity versus applied voltage in the dark and under UV illumination for the sample shown in Fig. 3.21. (b) The current density versus EL intensity for the same sample showing no difference in the dark versus under UV illumination.

Another more dramatic demonstration of photo-conductive blocking barriers on EL imaging is shown in Fig. 3.23. The growth parameters for this sample are similar to those for the sample shown in Fig. 3.21. It is apparent from looking at Fig. 3.23 that a large contrast in EL intensity is observed across the sample in the dark, which is effectively removed under both blue and UV light, although not under red light. These non-uniformities are not a result of lateral variations in the primary diode properties across the sample but are instead a result of laterally non-uniform blocking barriers on the sample. It is important to note that these blocking barriers will also disappear when the sample is measured under a solar simulator and therefore have very little impact on the overall device efficiency. As such, when using EL imaging to analyze the impact of non-uniformities on device performance, it is important to use a UV offset to eliminate the effect of secondary barriers.
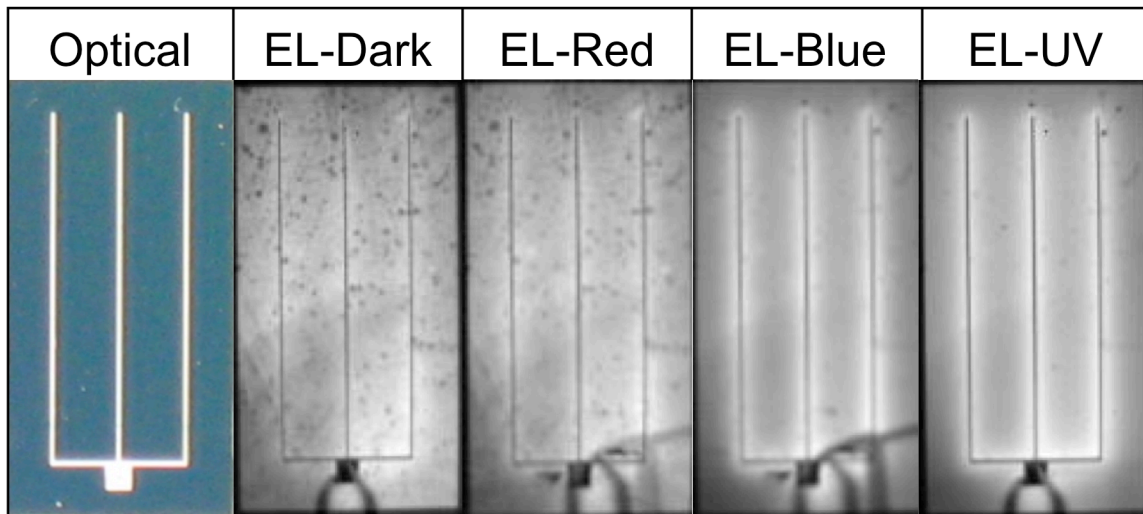
Optical	EL-Dark	EL-Red	EL-Blue	EL-UV

Fig. 3.23: Optical image of a $CuIn_{0.1}Ga_{0.9}Se_2$ solar cell along with EL images taken in the dark and under red, blue and UV illumination.

Fig. 3.23 shows another interesting effect when comparing the blue and red images. The blue image was measured prior to the red image using a blue LED positioned off to the side of the sample. Due to the directional illumination, the contact probes appear to cast a shadow on the sample surface. However, this shadow is not a result of reflection but comes from blocking barriers on the sample that have not received a sufficient photon flux to be removed. The red image was measured immediately after this blue image was taken, and it is apparent that the shadow from the contact probe remains on the surface. As such, this image directly shows the photoconductive secondary barrier has a slow decay time and the secondary barrier does not immediately return after the illumination is removed. A study of the time dependence of the EL intensity decay after UV illumination is shown in Fig. 3.24. This figure shows that photoconductivity of CdS persists for hours after just two minutes of illumination.
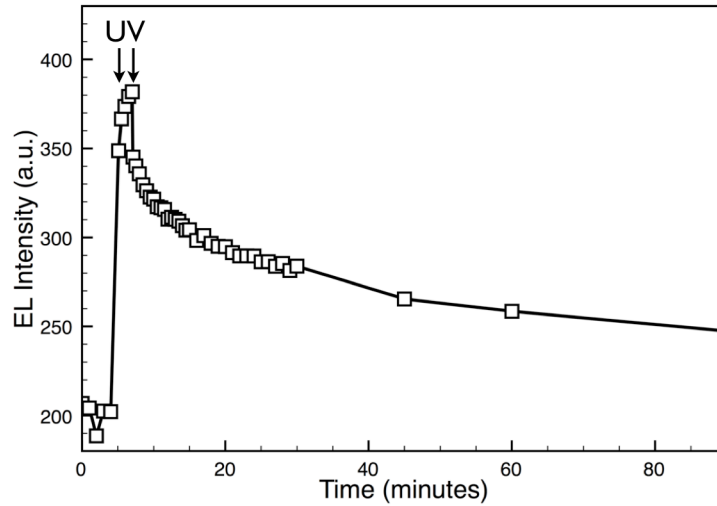
Fig. 3.24. EL intensity of a $CuIn_{0.1}Ga_{0.9}Se_2$ solar cell as a function of time. The cell was kept in the dark for the first 5 minutes and then exposed to UV light for 2 minutes. The increased EL intensity persisted for several hours before decaying to its equilibrium value.

An important conclusion regarding the origin of the secondary barrier effect can be drawn from Fig. 3.23. The red illumination clearly shows a strong lateral variation in the blocking behavior of the cell, similar to that observed in the dark image. If the secondary barrier was a result of deep acceptors in the ODC, one would expect the secondary barriers would be removed under red illumination as the ODC bandgap is ~ 1.6eV[3.6.14]. However, this is not observed suggesting the origin of the photoconductive secondary barrier lies in the CdS layer. Furthermore, this also indicates that the Fermi-level at the CdS/CIGS interface is not pinned. It is interesting to note that the efficiency of the cell shown in Fig. 3.23 is 13.6% (J_{sc} = 37.5mA/cm^2, V_{oc} = 516mV and FF=0.7), which is fairly efficient for a CIGS solar cell given the sub-optimal Ga/(In+Ga) ratio. This indicates that it is possible to achieve high efficiency CIGS solar cells without a pinned CdS/CIGS interface.

Blocking barriers often have additional impacts on device characterization beyond adding additional contrast to EL images. For instance, it has been observed that secondary diodes in series with a primary diode can lead to an inflated diode ideality factor[3.6.18]. In several cases, this makes it difficult to use the diode ideality factor as a tool to characterize which part of the device is responsible for recombination[3.6.19]. In this case, it is helpful to note that the EL ideality factor should in theory be equal to 1 (Eqn. 3.4). Therefore, a deviation in the EL ideality factor from 1 can be attributed to the effect of secondary blocking barriers. This is shown in Fig. 3.25 in the voltage dependence of both the injection current and EL intensity for the same sample as imaged in Fig. 3.23. In the dark, the EL ideality factor is 2 but drops to 1.2 when the cell is under UV illumination. Likewise, the current ideality factor is inflated to 3 in the dark but drops to 1.7 under UV illumination. As such, it's possible to ascribe the high ideality factor of the sample in the dark to the influence of the photoconductive secondary barrier.
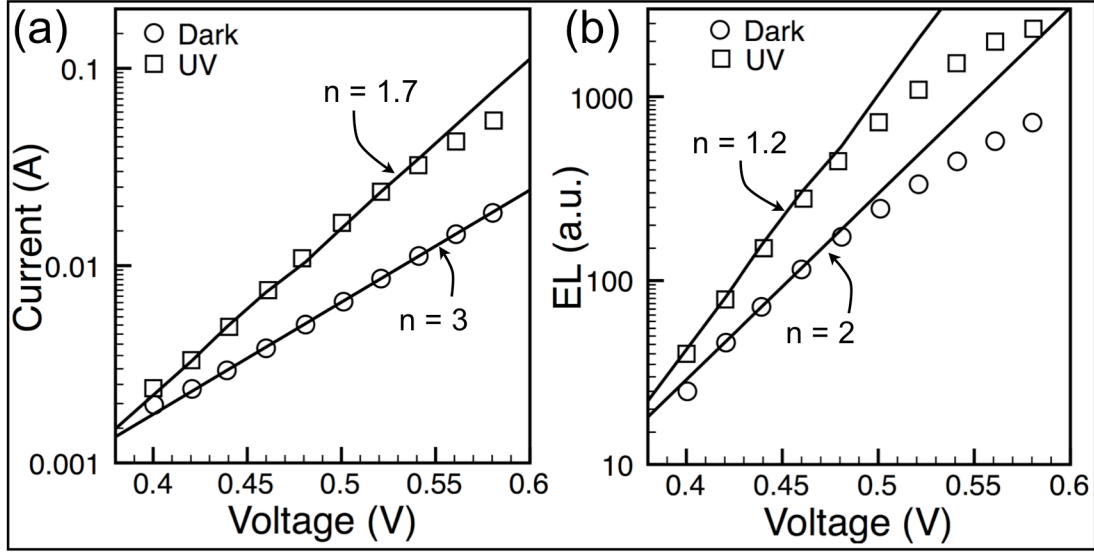
81

Fig. 3.25. (a) Current and (b) EL intensity versus voltage with and without a UV offset. The ideality factor (n) and corresponding fit are shown in each image.

Secondary barriers will also affect measurements of the TCO sheet resistance from the EL intensity distribution away from the aluminum fingers. Previous publications have shown the lateral gradient in EL intensity can be used to determine the TCO sheet resistance[3.6.20, 3.6.21]. This approach assumes that there are no secondary barriers in series with the primary CIGS diode. However, secondary barriers can effectively limit the amount of current that can go through any one portion of the cell and as such, will affect the lateral gradient in EL intensity across the sample. An example of this is shown in Fig. 3.26 where the average EL intensity is plotted across a sample at 20mA of forward current. Following the approach of Ref. 3.6.20 and Ref. 3.6.21, one would come to the conclusion that the TCO sheet resistance changed dramatically under UV illumination. However, this is not the case as the different line profiles are simply a result of the large secondary barriers in the dark.
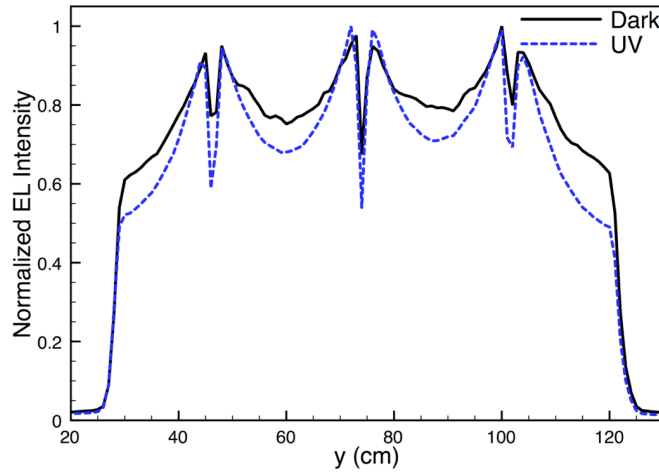

Fig. 3.26: Normalized EL intensity lines scans across the sample with and without a UV offset. The images were taken at 20mA forward current.

Conclusions

Thin film photovoltaics are a very promising source of renewable energy. However, a fundamental understanding of the physical and electronic parameters governing device performance is lacking. One of the main complications when dealing with thin film photovoltaics is the inherent electronic non-uniformities present in the cells. The purpose of this work was to develop new characterization techniques and modeling approaches to quantify the effects of these non-uniformities using CIGS as a model materials system. Therefore, while all of the experimental results in this work come from CIGS samples, the advances in characterization techniques and modeling are applicable to any thin film material system.

The technique of electron beam induced current was extended in this work to characterize the depth dependent electronic properties in compositionally graded thin film absorbers. This technique was specifically applied to the CIGS material system where it was experimentally shown that gallium gradients present in high efficiency CIGS solar cells improve the carrier collection efficiency by introducing quasi-electric fields into the absorber. However, the bulk diffusion length in these films was found to have no correlation with the device open circuit voltage suggesting the dominant recombination pathway in these cells occurs through a separate set of defects in the space charge region. This result provides a theoretical justification for the gallium depth profile experimentally observed in the highest efficiency CIGS samples. The advances in electron beam induced current are generally applicable to any material system involving compositionally graded absorbers, including new solar cell materials such as InGaN. With this technique, it is possible to quantitatively determine the influence of compositional grading on carrier collection efficiency.

To understand the influence of lateral electron non-uniformities on device behavior, a theory of electroluminescence intensity was developed for thin film photovoltaics. It was found that electroluminescence intensity, when combined with electron beam induced current images, can be used to quantitatively image both the bandgap and collection probability across a cell. Finally, the electroluminescence intensity was found to be very sensitive to secondary blocking barriers allowing these barriers to be directly imaged.

Together, the advances in characterization techniques and modeling approaches described in this work are critical components in determining the effects of non-uniform electronic properties in thin film photovoltaics. These modeling efforts are important not only for future efficiency improvements but also for research efforts focused on understanding how the physical properties of these materials affect the observed electronic properties. Ultimately, these efforts will lead to a greater understanding of which materials properties are critical in designing solar cells and in turn help design the next generation of cheaper, more efficient photovoltaics.

References

1.1   Thin Film Photovoltaics Overview

[1.1.1] U.S. Energy Information Administration Forecasts,
http://www.eia.doe.gov/oiaf/forecasting.html

[1.1.2] AM 1.5 Solar Spectrum, http://rredc.nrel.gov/solar/spectra/am1.5/

[1.1.3] G. Brown and J. Wu, Laser and Photonics Reviews 3, 394-405 (2009).

[1.1.4] M. Green, Third Generation Photovoltaics: Advanced Solar Energy Conversion (Springer, New York, 2003).

[1.1.5] W. Shockley and H. Queisser, J. Appl. Phys. 32, 510-519 (1961).

[1.1.6] W. Shockley and W. Read, Phys. Rev. 87, 835-842 (1952).

[1.1.7] M. Green, K. Emery, Y. Hishikawa and W. Warta, Prog. Photovolt 17, 85-94 (2009).

[1.1.8] X. Wu, J. Keane, R. Dhere, C. DeHart, A. Duda, T. Gessert, S. Asher, D. Levi and P. Sheldon, Proceedings of the 17th European Photovoltaic Solar Energy Conference, Munich, 22-26, 995-1000 (2001).

[1.1.9] I. Repins, M. A. Contreras, B. Egaas, C. DeHart, J. Scharft, C. Perkins, B. To and R. Noufi, Prog. Photovoltaics 16, 235-239 (2008).

[1.1.10] M. Green, Prog. Photovoltaics 17, 183-189 (2009).

1.2   Cu(In,Ga)Se$_2$ (CIGS) Device Structure

[1.2.1] J. Shay, S. Wagner and H. Kasper, Appl. Phys. Lett. 27, 89-90 (1975).

[1.2.2] L. Kazmerski, F. Whie and G. Morgan, Appl. Phys. Lett. 29, 268-270 (1976).

[1.2.3] R. Mickelsen, W. Chen, Y. Hsiao and V. Lowe, IEEE Trans. Electron Devices 31, 542-546 (1984).

[1.2.4] R. Potter, Solar Cells 16, 521-527 (1986).

[1.2.5] I. Repins, M. Contreras, B. Egaas, C. DeHart, J. Scharft, C. Perkins, B. To and R. Noufi, Prog. Photovolt. 16, 235-239 (2008).

[1.2.6] J. Hedstrom, H. Ohlsen, M. Bodegard, A. Kylner, L. Stolt, D. Hariskos, M. Ruckh and H. Schock, IEEE Photovoltaic Specialist Conf. 364-371 (1993).

[1.2.7] U. Rau and H. Schock, Appl. Phys. A 69, 131-147 (1999).

[1.2.8] W. Shafarman, J. Phillips, IEEE Photovoltaic Specialist Conf. 841, 917-919 (1996).

[1.2.9] T. Wada, N. Kohara, T. Negami and M. Nishitani, Jpn. J. Appl. Phys. 35, 1253-1256 (1996).

[1.2.10] T. Friedlmeier, D. Braunger, D. Hariskos, M. Kaiser, H. Wanka and H. Schock, IEEE Photovoltaic Specialist Conf. 841, 847-848 (1996).

[1.2.11] A. Pudov, PhD thesis, Colorado State University (2005).

[1.2.12] U. Rau, P. Grabitz and J. Werner, Appl. Phys. Lett. 85, 6010-6012 (2004).

[1.2.13] A. Gabor, J. Tuttle, D. Albin, M. Contreras, R. Noufi and A. Hermann, Appl. Phys. Lett. 65, 198-200 (1994).

[1.2.14] P. Jackson, R. Wurz, U. Rau, J. Mattheis, M. Kurth, T. Schlotzer, G. Bilger and J. Werner, Prog. Photovolt. 15, 507-519 (2007).

[1.2.15] I. Repins, B. Stanbery, D. Young, S. Li, W. Metzger, C. Perkins, W. Shafarman, M. Beck, L. Chen, V. Kapur, D. Tarrant, M. Gonzalez, D. Jensen, T. Anderson, X. Wang, L.

Kerr, B. Keyes, S. Asher, A. Delahoy and B. Von Roedern, Prog. Photovolt. 14, 25-43 (2006).

1.2.16 S. Wei, A. Zunger, Appl. Phys. Lett. 63, 2549-2551 (1993).

1.2.17 D. Schmid, M. Ruckh, H. Schock, Sol. Energy Mater. Sol. Cells 41, 281-294 (1996).

1.2.18 A. Niemegeers, M. Burgelman and A. De Vos, Appl. Phys. Lett. 67, 843-645 (1995).

1.2.19 M. Ruckh, D. Schmid and H. Schock, J. Appl. Phys. 76, 5945-5948 (1994).

1.2.20 Q. Nguyen, K. Orgassa, I. Koetschau, U. Rau and H. Schock, Thin Solid Films, 431, 330-334 (2003).

1.3   Physics of Photovoltaics

1.3.1 S. Sze and K. Ng, *Physics of Semiconductor Devices* (Wiley, New York 2007) pg. 17-21, 62-63, 91.

1.3.2 NGSPICE, http://ngspice.sourceforge.net/

1.3.3 J. Pankove, *Optical Processes in Semiconductors* (Dover, New York, 1971), 110-111.

1.3.4 W. Shockley and W. Read, Phys. Rev. 87, 835-842 (1952).

1.3.5 A. Milnes, *Deep Impurities in Semiconductors* (Wiley, New York 1973), pg. 180-182.

1.3.6 M. A. Green, Prog. Photovoltaics 17, 57-66 (2009).

1.3.7 U. Rau and H. Schock,, Appl. Phys. A 69, 313-147 (1999).

1.3.8 R. Scheer, J. Appl. Phys 105, 104505 (2009).

1.3.9 J. Sites and P. Mauk, Solar Cells 27, 411-417 (1989).

1.3.10 U. Rau, Appl. Phys. Lett. 74, 111-113 (1999).

1.3.11 C. Donolato, Appl. Phys. Lett. 46, 270-272 (1985).

1.4   Electronic properties of CIGS

1.4.1 A. Luque and S. Hegedus, *Handbook of Photovoltaic Science and Engineering* (Wiley, New York 2003) pg. 567-616.

1.4.2 S. Wei and A. Zunger, J. Appl. Phys. 78, 3846-3856 (1995).

1.4.3 S. Wasim, C. Rincon, G. Marin, P. Bocaranda E. Hernandez, I. Bonalde and E. Medina, Phys. Rev. B 64, 195101 (2001).

1.4.4 J. Cohen, J. Heath and W. Shafarman, *Wide-gap Chalcopyrites* (Springer, New York, 2006), pg. 69-90.

1.4.5 R. Noufi, R. Axton, C. Herrington and S. Deb Appl. Phys. Lett. 45, 668-670 (1984).

1.4.6 S. Zhang, S. Wei, A. Zunger and H. Katayama-Yoshida Phys. Rev. B 57, 9642-9656 (1998).

1.4.7 S. Lany and A. Zunger Phys. Rev. B 72, 035215 (2005).

1.4.8 S. Lany and A. Zunger J. Appl. Phys. 100, 113725 (2006).

1.4.9 P. Jackson, R. Wurz, U. Rau, J. Mattheis, M. Kurth, T. Schlotzer, G. Bilger and J. Werner, Prog. Photovolt. 15, 507-519 (2007).

1.4.10 A. Li and I. Shih, J. Electron. Materials 22, 195-199 (1993).

1.4.11 T. Walter, R. Herberholz, C. Muller and H. Schock, J. Appl. Phys. 80, 4411-4420 (1996).

1.4.12 M. Igalson and H. Schock, J. Appl. Phys. 80, 5765-5769 (1996).

1.4.13 M. Burgelman, F. Engelhardt, J. Guillemoles, R. Herberholz, M. Igalson, R. Klenk, M. lampert, T. Meyer, V. Nadenau, A. Niemegeers, J. Parisi, U. Rau, H. Schock, M. Schmitt, O. Seifert, T. Walter and S. Zott, Prog. Photovolt. 5, 121-130 (1997).

[1.4.14] M. Turcu and U. Rau, Thin Solid Films 431, 158-162 (2003).

[1.4.15] G. Hanna, A. Jasenek, U. Rau and H. Schock, Phys. Stat. Sol. (a) 179, R7-R8 (2000).

[1.4.16] A. Jasenek, U. Rau, T. Hahn, G. Hanna, M. Schmidt, M. Hartmann, H. Schock, J. Werner, S. Kraft, K. Schmid and W. Bolse, Appl. Phys. A 70, 677-680 (2000).

[1.4.17] U. Rau, K. Weinert, Q. Nguyen, M. Mamor, G. Hnna, A. Jasenek and H. Schock, MRS 668, H9.1 (2001).

[1.4.18] M. Igalson and H. Schock, J. Appl. Phys. 80, 5765-5769 (1996).

[1.4.19] M. Ruberto and A. Rothwart, J. Appl. Phys. 61, 4662-4669 (1987).

[1.4.20] F. Engelhardt, M. Schmidt, T. Meyer, O. Seifert, J. Parisi and U. Rau, Phys. Lett. A 245, 489-493 (1998).

[1.4.21] S. Lany and A. Zunger, J. Appl. Phys. 100, 113725 (2006).

[1.4.22] M. Eron and A. Rothwarft, J. Appl. Phys. 57, 2275-2279 (1985).

[1.4.23] U. Rau and H. Schock, Appl. Phys. A 69, 131-147 (1999).

[1.4.24] M. Bar, I. Repins, M. Contreras, L. Weinhardt, R. Noufi and C. Heske, Appl. Phys. Lett. 95, 052106 (2009).

[1.4.25] T. Walter, R. Menner, Ch. Koble and H. Schock, Proceddings of the 12th European Photovoltaic Solar Energy Conference. Pg. 1755 – 1758 (1994).

[1.4.26] U. Rau, Appl. Phys. Lett. 74, 111-113 (1999).

[1.4.27] W. Metzger, I. Repins and M. Contreras, Appl. Phys. Lett. 93, 022110 (2008).

[1.4.28] L. Gutay and G. Baur, Thin Solid Films 515, 6212-6216 (2007).

[1.4.29] M. Romero, K. Ramanathan, M. Contreras, M. Al-Jassim, R. Noufi and P. Sheldon, Appl. Phys. Lett. 83, 4770-4772 (2003).

[1.4.30] M. Mayer, L. Ruppalt, D. Hebert, J. Lyding and A. Rockett, J. Appl. Phys. 107, 034906 (2010).

[1.4.31] J. Werner, J. Mattheis and U. Rau, Thin Solid Films 480-481, 399-409 (2005).

[1.4.32] U. Rau and J. Werner, Appl. Phys. Lett. 84, 3735-3737 (2004).

[1.4.33] U. Rau, P. Grabitz and J. Werner, Appl. Phys. Lett. 85, 6010-6012 (2004).

[1.4.34] C. Ludwig, T. Gruhn, C. Felser, T. Schilling, J. Windeln and P. Kratzer, Phys. Rev. Lett. 105, 025702 (2010).

[1.4.35] T. Dullweber, G. Hanna, W. Shams-Kolahi, A. Schwartzlander, M. Contreras, R. Noufi and H. Schock, Thin Solid Films 361-362, 478-481 (2000).

[1.4.36] T. Dullweber, O. Lundberg, J. Malmstrom, M. Bodegard, L. Stolt, U. Rau, H. Schock and J. Werner, Thin Solid Films 387, 11-13 (2007).

[1.4.37] J. Song, S. Li, C. Huang, O. Crisalle and T. Anderson, Solid-State Electron. 48, 73-79 (2004).

2.1 Background

[2.1.1] J. Hutchby and R. Fudurich, J. Appl. Phys. 47, 3140-3151 (1976).

[2.1.2] G. Virshup, C. Ford and J. Werthen, Appl. Phys. Lett. 47, 1319-1321 (1985).

[2.1.3] C. Donolato, Appl. Phys. Lett. 46, 270-272 (1985).

[2.1.4] N. Arora, S. Chamberlain and D. Roulston, Appl. Phys. Lett. 37, 325-327 (1980).

[2.1.5] C. Wu and D. Wittry, J. Appl. Phys. 49, 2827-2836 (1978).

[2.1.6] J. Parisi, D. Hilburger, M. Schmitt and U. Rau, Sol. Energy Mater. Sol. Cells 50, 79-85 (1998).

[2.1.7] J. Mattheis, P. Rostan, U. Rau and J. Werner, Sol. Energy Mater. Sol. Cells 91, 689-695 (2007).

2.1.8 R. Scheer, C. Knieper and L. Stolt, Appl. Phys. Lett. 67, 3007-3009 (1995).

2.1.9 R. Scheer, M. Wilhelm, H. Lewerenz, H. Schock and L. Stolt, Sol. Energy Mater. Sol Cells 49, 299-309 (1997).

2.1.10 B. Sieber, C. Ruiz and V. Bermudez, Superlattices Microstruct. 45, 161-167 (2009).

2.2   Electron Beam Carrier Generation Function

2.2.1 D. Drouin, A. Couture, D. Joly, X. Tastet, V. Aimez and R. Gauvin, Scanning 29, 92-101 (2007).

2.2.2 P. Hovington, D. Doruin and R. Gauvin, Scanning 19, 1-14 (1997).

2.2.3 P. Hovington, D. Doruin, R. Gauvin, D. Joy and N. Evans, Scanning 19, 29-35 (1997).

2.2.4 C. Wu and D. Wittry, J. Appl. Phys. 49, 2827-2836 (1978).

2.2.5 W. Drummond and J. Moll, J. Appl. Phys. 42, 5556-5562 (1971).

2.2.6 H. Leamy, J. Appl. Phys. 53, R51-R80 (1982).

2.2.7 R. Scheer, Philos. Mag. B 72, 75-80 (1995).

2.3   Carrier Collection Function

2.3.1 S. Sze and K. Ng, *Physics of Semiconductor Devices* (Wiley, New York 2007) pg. 85.

2.3.2 M. Gloeckler, A. Fahrenbruch and J. Sites, Proceedings of the 3rd World Conference on Photovoltaic Energy Conversion, May 11-18, 2003 Osaka, Japan. 491-494.

2.3.3 J. Heath, J. Cohen and W. Shafarman, J. Appl. Phys. 95, 1000-1010 (2004).

2.4   Influence of Gallium Gradients on Collection

2.4.1 G. Brown, V. Faifer, A. Pudov, S. Anikeev, E. Bykov, M. Contreras and J. Wu, Appl. Phys. Lett. 96, 022104 (2010).

2.4.2 M. A. Green, Prog. Photovoltaics 17, 57-66 (2009).

2.4.3 J. Mattheis, P. Rostan, U. Rau and J. Werner, Sol. Energy Mater. Sol. Cells 91, 689-695 (2007).

2.5   Influence of Gallium Gradients on Forward Current

2.5.1 R. Scheer, J. Appl. Phys 105, 104505 (2009).

2.5.2 G. Brown, V. Faifer, B. Cardozo, E. Bykov and M. Contreras, Appl. Phys. Lett. 96, 222102 (2010).

2.5.3 T. Dullweber, O. Lundberg, J. Malmstrom, M. Bodegard, L. Stolt, U. Rau, H. Schock and J. Werner, Thin Solid Films 387, 11-13 (2001).

2.5.4 K. Ramanathan, M. Contreras, C. Perkins, S. Asher, F. Hasoon, J. Keane, D. Young, M. Romero, W. Metzger, R. Noufi, J. Ward and A. Duda, Prog. Photovoltaics 11, 225-230 (2003).

2.5.5 M. Mayer, L. Ruppalt, D. Hebert, J. Lyding and A. Rockett, J. Appl. Phys. 107, 034906 (2010).

2.5.6 J. Werner, J. Mattheis and U. Rau, Thin Solid Films 480-481, 399-409 (2005).

2.5.7 A. Rockett, Thin Solid Films 361-362, 330-337 (2000).

2.5.8 A. Milnes, *Deep Impurities in Semiconductors* (Wiley, New York, 1973), pp. 180-182.

2.5.9 S. Lany and A. Zunger, J. Appl. Phys. 100, 113725 (2006).

2.5.10 F. Engelhardt, M. Schmidt, Th. Meyer, O. Seifert, J. Parisi and U. Rau, Phys. Lett. A 245, 489-493 (1998).

2.6   Cross Sectional EBIC

[2.6.1] M. Contreras, H. Wiesner, D. Niles, K. Ramanathan, R. Matson, J. Tuttle, J. Keane and R. Noufi, Proceedings of the 25th Photovoltaics Specialist Conference, Washington, DC. May 13-17 1996. 809-812.

[2.6.2] J. Rechid, A. Kampmann and R. Reineke-Koch, Thin Solid Films 361-362, 198-202 (2000).

[2.6.3] R. Kniese, M. Powalla and U. Rau, Thin Solid Films 515, 6163-6167 (2007).

[2.6.4] R. Kniese, M. Powalla and U. Rau, Thin Solid Films 517, 2357-2359 (2009).

[2.6.5] L. Jastrzebski, J. Lagowski and H. Gatos, Appl. Phys. Lett. 27, 537-539 (1975).

[2.6.6] M. Nichterwitz, D. Abou-Ras, K. Sakurai, J. Bundesmann, T. Unold, R. Scheer and H. Schock, Thin Solid Films 517, 2554-2557 (2009).

3.1   Background

[3.1.1] V. Karpov, A. Compaan and D. Shvydka, Appl, Phys. Lett. 80, 4256-4258.

[3.1.2] J. Werner, J. Mattheis and U. Rau Thin Solid Films 480-481, 399-409 (2005).

[3.1.3] U. Rau, P. Grabitz and J. Werner, Appl. Phys. Lett. 85, 6010-6012 (2004).

[3.1.4] U. Rau and J. Werner, Appl. Phys. Lett. 84, 3735-3737 (2004).

[3.1.5] C. Ludwig, T. Gruhn, C. Felser, T. Schilling, J. Windeln and P. Kratzer, Phys. Rev. Lett. 105, 025702 (2010).

[3.1.6] J. Mattheis, U. Rau and J. Werner, J. Appl. Phys. 101, 113519 (2007)

[3.1.7] T. Kirchartz and U. Rau, J. Appl. Phys. 102, 104510 (2007).

[3.1.8] J. Cohen, J. Heath and W. Shafarman, *Wide-Gap Chalcopyrites* (Springer, New York, 2006), 69-90.

[3.1.9] M. A. Mayer, L. B. Ruppalt, D. Hebert, J. Lyding and A. A. Rockett, J. Appl. Phys. 107, 034906 (2010).

[3.1.10] G. Hanna, A. Jasenek, U. Rau and H. Schock, Phys. Stat. Sol. (a) 179, R7 (2000).

[3.1.11] J. Parisi, D. Hilburger, M. Schmitt and U. Rau, Sol. Energy Mater. Sol. Cells 50, 79-85 (1998).

[3.1.12] K. Bothe, G. Bauer and T. Unold, Thin Solid Films 304, 453-456 (2002).

[3.1.13] M. Romero, K. Ramanathan, M. Contreras, M. Al-Jassim, R. Noufi and P. Sheldon, Appl. Phys. Lett. 83, 4770-4772 (2003).

[3.1.14] D. Eich, U. Herber, U. Groh, U. Stahl, C. Heske, M. Marsi, M. Kiskinova, W. Riedl, R. Fink and E. Umbach, Thin Solid Films 361, 258-262 (2000).

[3.1.15] P. Grabitz, U. Rau, B. Wille, G. Bilger and J. Werner, J. Appl. Phys. 100, 124501 (2006).

[3.1.16] L. Gutay, C. Lienau and G. Bauer, Appl. Phys. Lett. 97, 052110 (2010).

[3.1.17] G. Bauer, R. Bruggemann, S. Tardon, S. Vignoli and R. Kniese, Thin Solid Films 480, 410-414 (2005).

[3.1.18] J. Pankove, *Optical Processes in Semiconductors* (Dover, New York, 1971), 110-111.

[3.1.19] S. Lany and A. Zunger, J. Appl. Phys. 100, 113725 (2006).

[3.1.20] V. G. Karpov, G. Rich, A. V. Subashiev and G. Dorer, J. Appl. Phys. 89, 4975-4985 (2001).

[3.1.21] U. Rau, T. Kirchartz, A. Helbig and B. Pieters, Mat. Res. Soc. Symp. Proc. 1165, M3.4 (2009).

[3.1.22] D. Hinken, K. Ramspeck, K. Bothe, B. Fischer and R. Brendel, Appl. Phys. Lett. 91, 182104 (2007).

[3.1.23] S. Feldman, F. Seymour, T. Ohno, V. Kaydanov and R. Collins, Mat. Res. Soc. Symp. Proc. 763, B5.10 (2003).

[3.1.24] U. Rau, Phys. Rev. B 76, 085303 (2007).

[3.1.25] T. Fuyuki, H. Kondo, Y. Kaji, A. Ogane and Y. Takahashi J. Appl. Phys. 101, 023711 (2007).

3.2   Theory of Electroluminescence (EL) Intensity in Thin Film Solar Cells

[3.2.1] U. Rau, H. W. Schock, Appl. Phys. A 69, 131-147 (1999).

[3.2.2] J. Pankove, *Optical Processes in Semiconductors* (Dover, New York, 1971), 110-111.

[3.2.3] M. Gloeckler, C. Jenkins, J. Sites, Mat. Res. Soc. Symp. Proc. 763, B5.20 (2003).

[3.2.4] M. A. Green, Prog. Photovoltaics 17, 57-66 (2009).

[3.2.5] G. Brown, V. Faifer, B. Cardozo, E. Bykov and M. Contreras, Appl. Phys. Lett. 96, 222102 (2010).

[3.2.6] T. Fuyuki, H. Kondo, Y. Kaji, A. Ogane and Y. Takahashi J. Appl. Phys. 101, 023711 (2007).

[3.2.7] "AMPS-1D" software was developed at Pennsylvania State University by S. Fonash, J. Arch, J. Hou, W. Howland, P. McElheny, A. Moquin, M. Rogosky, F. Rubinelli, T. Tran and H. Zhu with support from the Electric Power Research Institute.

3.3   Extracting Shunt and Sheet Resistance from EL Images

[3.3.1] V. G. Karpov, G. Rich, A. V. Subashiev and G. Dorer, J. Appl. Phys. 89, 4975-4985 (2001).

[3.3.2] A. Helbig, T. Kirchartz, R. Schaeffler, J. Werner and U. Rau, Sol. Energy Mater. Sol. Cells 94, 979-984 (2010).

[3.3.3] D. Hinken, K. Ramspeck, K. Bothe, B. Fischer and R. Brendel, Appl. Phys. Lett. 91, 182104 (2007).

[3.3.4] NGSPICE, http://ngspice.sourceforge.net/

3.4   Quantifying Lateral Variations in Bandgap and Collection Length

[3.4.1] C. Donolato. Appl. Phys, Lett. 46, 270-271 (1985).

[3.4.2] M. Nichterwitz, D. Abou-Ras, K. Sakurai, J. Bundesmann, T. Unold, R. Scheer and H. W. Schock, Thin Solid Films 517, 2554-2557 (2009).

[3.4.3] M. A. Green, Prog. Photovoltaics 17, 57-66 (2009).

[3.4.4] U. Rau and J. H. Werner, Appl. Phys. Lett. 84, 3735-3737 (2004).

[3.4.5] U. Rau, P. O. Grabitz and J. H. Werner, Appl. Phys. Lett. 85, 6010-6012 (2004).

[3.4.6] G. Brown, A. Pudov, B. Cardozo, V. Faifer, E. Bykov and M. Contreras, J. Appl. Phys. 108, 074516 (2010).

[3.4.7] NGSPICE, http://ngspice.sourceforge.net/

[3.4.8] P. D. Paulson, R. W. Birkmire and W. N. Shafarman, J. Appl. Phys. 94, 879-888 (2003).

3.5   Impact of Non-uniformities on Device Behavior

[3.5.1] W. Metzger, I. Repins and M. Contreras, Appl. Phys. Lett. 93, 022110 (2008).

3.6   Secondary Diode Effects

[3.6.1] M. Roy, S. Damaskinos and J. Phillips, Proceedings 20th IEEE hotovoltaic Specialists Conference, Las Vegas, NV, IEEE, New York, 1988, 1618-1623.

[3.6.2] J. Tuttle, J. Sites, A. Delahoy, W. Shafarman, B. Basol, S. Fonash, J. Gray, R. Menner, J. Phillips, A. Rockett, J. Scofield, F. Shapiro, P. Singh, V. Suntharalingam, D. Tarrant, T. Walter, S. Wiedeman and T. Peterson, Prog. Photovolt. 3, 89-104 (1995).

[3.6.3] S. Wei, A. Zunger, Appl. Phys. Lett. 63, 2549-2551 (1993).

[3.6.4] D. Schmid, M. Ruckh, H. Schock, Sol. Energy Mater. Sol. Cells 41, 281-294 (1996).

[3.6.5] A. Niemegeers, M. Burgelman and A. De Vos, Appl. Phys. Lett. 67, 843-845 (1995).

[3.6.6] U. Rau, D. Braunger, R. Herberholz, H. Schock, J. Guillemoles, L. Kronik and D. Cahen, J. Appl. Phys. 86, 497-505 (1999).

[3.6.7] C. Guillen, M. Martinez and J. Herrero, Thin Solid Films 335, 37-42 (1998).

[3.6.8] M. Gloeckler, C. Jenkins, J. Sites, Mat. Res. Soc. Symp. Proc. 743, B5.20 (2003).

[3.6.9] I. Eisgruber, J. Granata, J. Sites, J. Hou and J. Kessler, Sol. Energy Mater. Sol. Cells 53, 367-377 (1998).

[3.6.10] K. Boer, J. Appl. Phys. 107, 023701 (2010).

[3.6.11] M. Gloeckler, A. Fahrenbruch and J. Sites, in Proc. 3rd World Conf. Photovoltaic Energy Conversion (2003), 491-494.

[3.6.12] D. Schmid, M. Ruckh, F. Grunwald and H. Schock, J. Appl. Phys. 73, 2902-2909 (1993).

[3.6.13] T. Schulmeyer, R. Hunger, A. Klein, W. Jaegerman and S. Niki, Appl. Phys. Lett. 84, 3067-3069 (2004).

[3.6.14] M. Bar, I. Repins, M. Contreras, L. Weinhardt, R. Noufi and C. Heske, Appl. Phys. Lett. 95, 052106 (2009).

[3.6.15] M. Contreras, H. Wiesner, D. Niles, K. Ramanathan, R. Matson, J. Tuttle, J. Keane and R. Noufi, Proceedings of the 25th Photovoltiac Specialist Conference (1996), 809-812.

[3.6.16] T. Eisenbarth, T. Unold, R. Caballero, C. Kaufmann and H. Schock, J. Appl. Phys. 107, 034509 (2010).

[3.6.17] A. Niemegeers, M. Burgelman, R. Herberholz, U. Rau, D. Hariskos and H. Schock, Prog. Photovolt. 6, 407-421 (1998).

[3.6.18] D. Zhu, J. Xu, A. Noemaun, J. Kim, E. Schubert, M. Crawford and D. Koleske, Appl. Phys. Lett. 94, 081113 (2009).

[3.6.19] J. Sites and R. Mauk, Sol. Cells 27, 411-417 (1989).

[3.6.20] U. Rau, T. Kirchartz, A. Helbig and B. Pieters, Mat. Res. Soc. Symp. Proc. 1165, M3.4 (2009).

[3.6.21] A. Helbig, T. Kirchartz, R. Schaeffler, J. Werner and U. Rau, Sol. Energy Mater. Sol. Cells 94, 979-984 (2010).

Appendices

1. Mathematica Program for Fitting Electron Beam Induced Current Data

```
sample := "C2228-13 3";
profile := "Linear";
Option := True; (* True if the SCR is > the first composition data point.  False if SCR is <
first composition point *)
Schottky := False;
q := 1.60217646*10^-19;
kb := 1.3806503*10^-23;
T := 300;
data = ReadList["H:\documents\EBIC\Data\\" <> sample <> ".txt", {Real, Real,
Real,Real, Real}];
For[k = 1, k <= Length[data], k++,
data[[k, 2]] = data[[k, 2]]*data[[k, 3]]*10^-9;
data[[k, 4]] = data[[k, 4]]*data[[k, 5]]*10^-12;]
EBICSignal = Drop[data, None, {3, 5}];
CorrectionFactor[V_] := 0.76; (* Account for backscattered electrons *)
wZnO = 200*10^-3; (* ZnO thickness in υm *)
wCdS = 80*10^-3;(* CdS thickness in υm *)
wCIGS := 2000*10^-3; (* CIGS thickness in υm *)
wSCR := 558*10^-3; (* Space charge width in υm *)
scaling := 0.94; (* Scaling factor for simulated QE curve *)
FZnO := 0; (* Carrier collection probability in ZnO *)
FCdS := 0.2; (* Carrier collection probability in CdS *)
FSCR := 1;(* Carrier collection probability in SCR *)
L := 0.30; (* Diffusion Length in μm *)
м := 100;(* mobility in cm^2/Vsec *)
S := 1*10^5; (* Surface recombination velocity cm*s^-1)
SL[x_, P1_, P2_] := (P2[[2]] - P1[[2]])/(P2[[1]] - P1[[1]])*(x - P1[[1]]) + P1[[2]];
Comps = ReadList["H:\documents\Composition Profile\\" <> profile <> ".txt", {Real,
Real}];
EgZnO := 3.3; (* Bandgap of ZnO in eV *)
EgCdS := 2.42; (* Bandgap of CdS in eV *)
EgMo := 10^5; (* Bandgap of Mo in eV, just a really high number to avoid EHPs *)
EgCIGS[x_] := 1.04` (1 - x) + 1.68` x - 0.2` x (1 - x); (* Bandgap of CIGS as function of
Gallium content *)
рZnO := If[Schottky, 2.70, 5.606];
рCdS := 4.82;
рMo := 10.28;
рCIGS := 5.57 ; (* Density of CIGS, just uses CGS values *)
wZnO = wZnO*рZnO/рCIGS;
wCdS = wCdS*рCdS/рCIGS;
Comp[z_] :=
 Which[z <= Comps[[2, 1]], SL[z, Comps[[1]], Comps[[2]]],
```

```
  Comps[[2, 1]] < z <= Comps[[3, 1]], SL[z, Comps[[2]], Comps[[3]]],
  Comps[[3, 1]] < z, SL[z, Comps[[3]], Comps[[4]]]];
jb := 10/10^12; (* Beam current in A *)
Eg[z_] :=
 Which[z <= wZnO, EgZnO, wZnO <= z <= (wCdS + wZnO),
  EgCdS, (wCdS + wZnO) <= z <= (wCdS + wZnO + wCIGS),
  EgCIGS[Comp[z - (wCdS + wZnO)]], (wCdS + wZnO + wCIGS) <= z, EgMo];
R[z_] := RCIGS;
z[z_] := 2.596 Eg[z] + 0.714; (* Empirical relationship for average energy to make one
EHP *)
G0[V_] := 6.25*10^21* V * CorrectionFactor[V]; (* Carrier generation rate cm^-
2sec^-1 *)
BARatio := 0.4; (* Next 4 terms are constants describing shape of the generation \
volume *)
u0 := 0.125;
du := 0.35;
b := 4;
A[V_] := n /.Solve[n*0.5*P^0.5*du*(1 + Erf[u0/du]) - BARatio*n*u0/b == G0[V], n]
R[V_] := (2.56` (V/30)^1.7`)/10^3; (* Maximum energy range of electrons *)
F[z_, V_] :=
 A[V][[1]]* Exp[-(((R[z]*z*10^-4)/R[V] - u0)/du)^2] - BARatio* A[V][[1]] * Exp[-((b
*R[z]*z*10^-4)/(R[V]*u0))]; (* Final expression of the Energy Dissipation Function *)
Correction[V_] := (1/G0[V] NIntegrate[F[z, V], {z, 0, 20}, PrecisionGoal -> 10])^-1;
F2b[z_, V_, jb_] := Correction[V]*(A[V][[1]]* Exp[-(((R[z]*z*10^-4)/R[V] -u0)/du)^2]
- BARatio* A[V][[1]] *Exp[-((b *R[z]*z*10^-4)/(R[V]*u0))])*q*jb;
F2[z_, V_, jb_] := 1/z[z] Correction[V]*(A[V][[1]]* Exp[-(((R[z]*z*10^-4)/R[V] -
u0)/du)^2] - BARatio* A[V][[1]] *Exp[-((b *R[z]*z*10^-4)/(R[V]*u0))])*q*jb;
QEEBICSignal = {};
For[k = 1, k <= Length[data], k++,
AppendTo[QEEBICSignal, {data[[k, 1]], data[[k, 2]]/NIntegrate[F2[z, data[[k, 1]],
data[[k, 4]]], {z, 0, wZnO + wCdS + wCIGS}]}]; ];
De := (kb*T*M*10^8)/q;
Nc := 6.7*10^17;
Nv := 1.5*10^19;
x[Startx_, Endx_, W_] := q/(kb*T)*(EgCIGS[Endx] - EgCIGS[Startx])/W;
Lmod[L_, Startx_, Endx_, W_] := L/(1 + ((x[Startx, Endx, W]*L)/2)^2)^0.5;
Smod[S_, Startx_, Endx_, W_] := S*10^4 + (x[Startx, Endx, W]*De)/2;
Jo[P1_, P2_, L_, S_, W_] := 10^-4*(De/Lmod[L, P1[[2]], P2[[2]], P2[[1]] -
P1[[1]]]*(Sinh[(W)/Lmod[L, P1[[2]], P2[[2]], P2[[1]] - P1[[1]]]] + (Smod[S, P1[[2]],
P2[[2]], P2[[1]] - P1[[1]]]*Lmod[L, P1[[2]], P2[[2]], P2[[1]] -
P1[[1]]]/De)*Cosh[(W)/Lmod[L, P1[[2]], P2[[2]], P2[[1]] -
P1[[1]]]])/(Cosh[(W)/Lmod[L, P1[[2]], P2[[2]], P2[[1]] - P1[[1]]]] + (Smod[S,
P1[[2]], P2[[2]], P2[[1]] - P1[[1]]]*Lmod[L, P1[[2]], P2[[2]], P2[[1]] -
P1[[1]]]/De)*Sinh[(W)/Lmod[L, P1[[2]], P2[[2]], P2[[1]] - P1[[1]]]]) -
De/2*x[P1[[2]], P2[[2]], P2[[1]] - P1[[1]]]);
```

Modified[x_, P1_, P2_, L_, S_, W_] := Exp[(x[P1[[2]], P2[[2]], P2[[1]] -
P1[[1]]]*x)/2]*(Cosh[(W - x)/Lmod[L, P1[[2]], P2[[2]], P2[[1]] - P1[[1]]]] +
(Smod[S, P1[[2]], P2[[2]], P2[[1]] - P1[[1]]]*Lmod[L, P1[[2]], P2[[2]], P2[[1]] -
P1[[1]]]/De)*Sinh[(W - x)/Lmod[L, P1[[2]], P2[[2]], P2[[1]] -
P1[[1]]]])/(Cosh[(W)/Lmod[L, P1[[2]], P2[[2]], P2[[1]] - P1[[1]]]] + (Smod[S,
P1[[2]], P2[[2]], P2[[1]] - P1[[1]]]*Lmod[L, P1[[2]], P2[[2]], P2[[1]] -
P1[[1]]]/De)*Sinh[(W)/Lmod[L, P1[[2]], P2[[2]], P2[[1]] - P1[[1]]]]]);
NeutralRegion[x_, L_, S_] := If[Option,
  Which[x <= wSCR, FSCR, wSCR < x <= Comps[[3, 1]],
   Modified[x - wSCR, Comps[[2]], Comps[[3]], L,
    Jo[Comps[[3]], Comps[[4]], L, S, wCIGS - Comps[[3, 1]]],
    Comps[[3, 1]] - wSCR], Comps[[3, 1]] < x,
   Modified[Comps[[3, 1]] - wSCR, Comps[[2]], Comps[[3]], L,
    Jo[Comps[[3]], Comps[[4]], L, S, wCIGS - Comps[[3, 1]]],
    Comps[[3, 1]] - wSCR]*
   Modified[x - Comps[[3, 1]], Comps[[3]], Comps[[4]], L, S,
    wCIGS - Comps[[3, 1]]]],
  Which[x <= wSCR, FSCR, wSCR < x <= Comps[[2, 1]],
   Modified[x - wSCR, Comps[[1]], Comps[[2]], L,
    Jo[Comps[[2]], Comps[[3]], L,
    Jo[Comps[[3]], Comps[[4]], L, S, wCIGS - Comps[[3, 1]]],
    Comps[[3, 1]] - Comps[[2, 1]]], Comps[[2, 1]] - wSCR],
   Comps[[2, 1]] < x <= Comps[[3, 1]],
   Modified[Comps[[2, 1]] - wSCR, Comps[[1]], Comps[[2]], L,
    Jo[Comps[[2]], Comps[[3]], L,
     Jo[Comps[[3]], Comps[[4]], L, S, wCIGS - Comps[[3, 1]]],
     Comps[[3, 1]] - Comps[[2, 1]]], Comps[[2, 1]] - wSCR]*
    Modified[x - Comps[[2, 1]], Comps[[2]], Comps[[3]], L,
    Jo[Comps[[3]], Comps[[4]], L, S, wCIGS - Comps[[3, 1]]],
    Comps[[3, 1]] - Comps[[2, 1]]], Comps[[3, 1]] < x,
   Modified[Comps[[2, 1]] - wSCR, Comps[[1]], Comps[[2]], L,
    Jo[Comps[[2]], Comps[[3]], L,
     Jo[Comps[[3]], Comps[[4]], L, S, wCIGS - Comps[[3, 1]]],
     Comps[[3, 1]] - Comps[[2, 1]]], Comps[[2, 1]] - wSCR]*
    Modified[Comps[[3, 1]] - Comps[[2, 1]], Comps[[2]], Comps[[3]], L,
    Jo[Comps[[3]], Comps[[4]], L, S, wCIGS - Comps[[3, 1]]],
    Comps[[3, 1]] - Comps[[2, 1]]]*
   Modified[x - Comps[[3, 1]], Comps[[3]], Comps[[4]], L, S,
    wCIGS - Comps[[3, 1]]]]]
  ];
F[z_, L_, S_] :=
  Which[z <= wZnO, FZnO, wZnO <= z <= (wCdS + wZnO),
   FCdS, (wCdS + wZnO) <= z <= (wCdS + wZnO + wSCR),
   FSCR, (wCdS + wZnO + wSCR) <= z <= (wCdS + wZnO + wCIGS),
   NeutralRegion[z - (wZnO + wCdS), L, S], (wCdS + wZnO + wCIGS) <= z, 0];

s[V_, L_, S_] := scaling*NIntegrate[F[z, L, S]*F2[z, V, 10^-10], {z, 0, wZnO + wCdS +
wCIGS}]/NIntegrate[F2[z, V, 10^-10], {z, 0, wZnO + wCdS + wCIGS}];
SimulatedQE = Table[{V, s[V, L, S]}, {V, 2, 40, 1}];